Universitat
de les Illes Balears

DOCTORAL THESIS 2019

TEMPORAL EVOLUTION OF MHD WAVES IN SOLAR CORONAL ARCADES

Samuel Rial Lesaga

Universitat de les Illes Balears

DOCTORAL THESIS 2019

Doctoral Programe of Physics

TEMPORAL EVOLUTION OF MHD WAVES IN SOLAR CORONAL ARCADES.

Samuel Rial Lesaga

Thesis supervisor: Iñigo Arregui Uribe-Echevarria
Thesis supervisor: Ramón Oliver Herrero
Thesis Tutor: Alicia Sintes Olives

Doctor by the university of the Balearic islands

Universitat de les Illes Balears

Dr. Ramón Oliver Herrero of the University of the Balearic Islands

DECLARE:

That the thesis entitled “Temporal evolution of magnetohydrodynamic waves in solar coronal arcades”, presented by Samuel Rial Lesaga to obtain the PhD degree, has been completed under my supervision.

For all intents and purposes, I hereby sign this document.

Signature

Dr. Ramón Oliver Herrero

Palma de Mallorca, 17 May 2019

Firmado electrónicamente por OLIVER HERRERO RAMON - 43031748J el día 09/09/2019 con un certificado emitido por AC FNMT Usuarios

Dr. Iñigo Arregui Uribe-Echebarria of the Instituto de Astrofísica de Canarias.

DECLARE:

That the thesis entitled "Temporal evolution of magnetohydrodynamic waves in solar coronal arcades", presented by Samuel Rial Lesaga to obtain the PhD degree, has been completed under my supervision.

For all intents and purposes, I hereby sign this document.

Signature

Firmado por ARREGUI URIBE-ECHEVARRIA IÑIGO - 15392542E el día 20/05/2019 con un certificado emitido por AC FNMT Usuarios

Dr. Iñigo Arregui Uribe-Echebarria

La Laguna, 17 May 2019

Firmado por ARREGUI URIBE-ECHEVARRIA IÑIGO - 15392542E el día 09/09/2019 con un certificado emitido por AC FNMT Usuarios

Acknowledgments

En primer lugar me gustaría agradecer al Dr. Ramon Oliver la amistad, la confianza y el apoyo incondicional que me siempre me ha ofrecido. El siempre ha sabido animarme y motivarme en los múltiples momentos difíciles que ha tenido esta tesis y estoy plenamente convencido de que si no hubiera sido por él esta tesis no existiría.
Gracias

Al Dr. Iñigo Arregui por su paciencia y su confianza en mi trabajo y en mi. Gracias motivarme cuando no lo estaba y por hacerme ver que este esfuerzo merece la pena.

Al Dr. José Luis Ballester y a todo el grupo de personas que forman o han formado parte el grupo de física solar de la Universitat de les Illes Balears y con los que he compartido algún congreso, desayuno o cena. Un buen ambiente de trabajo siempre es una gran ayuda a la hora de realizar cualquier trabajo y en este caso ha sido genial.

A mis padres, Rubén y Clarisa, porque siempre me han apoyado durante este proceso que parecía no tener fin, por la formación y valores que me han dado y por muchas otras cosas que es imposible enumerar aquí.

A mi pareja Diana por apoyarme y estar siempre a mi lado sin importarle el camino que elija por muy extraño que este sea.

Finalmente agradezco al Ministerio de Educación y Ciencia la concesión de la beca asociada al proyecto BES-2007-16670 gracias a la cual este trabajo ha sido posible.

List of publications

The format of this thesis is compendium of articles. In the following list appear the published articles from which the present thesis is made.

- Rial, S., Arregui, I., Oliver, R. and Terradas, J.: 2019, Determining normal mode features from numerical simulations using CEOF analysis: I. Test case using transverse oscillations of a magnetic slab, ApJ 876(1), 86, doi: 10.3847/1538-4357/ab1417

- Rial, S., Arregui, I., Terradas, J., Oliver, R. and Ballester, J. L.: 2010, Three-dimensional Propagation of Magnetohydrodynamic Waves in Solar Coronal Arcades, ApJ 713, 651661, doi:10.1088/0004-637X/713/1/651.

- Rial, S., Arregui, I., Terradas, J., Oliver, R. and Ballester, J. L.: 2013, Wave Leakage and Resonant Absorption in a Loop Embedded in a Coronal Arcade, ApJ 763, 16, doi:10.1088/0004-637X/763/1/16.

Aim of the thesis

The aim of this thesis is to go a step further in the theoretical modeling of coronal loops. Following that direction, our main goal is to be able to theoretically reproduce part of the observed complexity that these structures display when a sudden release of energy occurs in the solar corona. Since not too much time ago, the theoretical models of these features have been rather simple. In order to have simple solutions, these models use big approximations, such as, straight instead of curved structures, one-dimensional/two-dimensional structures, etc.

In order to go beyond that simple models, our aim is to increase the complexity of the theoretical models by adding what we think can be some key ingredients just like the curvature or three-dimensionality. In this work we will adopt the approach of increase the complexity of the model step by step to create a solid base of knowledge that helps us understand the underlying physics. Therefore we will begin with a well known two-dimensional problem and then we will allow perturbations propagate in the third direction as a first step towards three-dimensionality. These are known as 2.5 dimensional models. Afterwards, we will add more ingredients such as a sharp model of coronal loop, different density profiles, curvature, etc.

The study of coronal loop oscillations can be done from several points of view but in this thesis we will focus in two of them. The first one is to solve the time-dependent MHD equations by means of a temporal code. In the first two papers Rial et al. (2010) and Rial et al. (2013) we use this approach.

The second approach consists in solve the normal modes of the system. The standard method to do so can be in general a difficult task because an specially designed numerical code is needed. For that reason another goal of this thesis is to develop a technique that allow us to find an alternative way to find the normal modes of any system. In Rial et al. (2019) we explain how this technique works as well as its advantages and disadvantages. .

Abstract of the thesis

0.1 Abstract

In this thesis we will study vertical oscillations in a potential arcade under the approximation of a zero-β plasma, when different density profiles are considered.
On one hand we will focus on the time-dependent problem to analyze the other side of the magnetohydrodynamic oscillations coin which traditionally is given by the normal mode analysis. We are going to study the propagation, energy transformation and damping of the impulsively generated waves as well as its relevant spatial and temporal scales in order to complete the picture. In order to study the wave damping, we examine two physical mechanisms that may be involved in the fast attenuation of the observed vertical coronal loop oscillations, namely wave leakage through wave tunneling and resonant absorption. In this wok whenever is possible, the time-dependent results are going to be compared with known normal mode properties to gain knowledge of how both sides are related as well as to test them.
On the other hand, we also will investigate the use of a new technique of obtaining the system normal modes when the standard normal mode analysis is difficult to be carried out. We will apply it to a straight coronal loop model and we will obtain them with the desired degree of accuracy thanks to several criteria based on the convergence of the method.

0.2 Resumen

En esta tesis estudiaremos las oscilaciones verticales de una arcada potencial en la aproximación $\beta \sim 0$ de un plasma, cuando diferentes perfiles de densidad son considerados.
Por un lado nos vamos a centrar en la evolución temporal de este problema para así analizar la otra cara de la moneda de las oscilaciones magnetohidrodinámicas, la cual tradicionalmente se ha estudiado mediante el análisis de modos normales. Vamos a estudiar la propagación, la conversión energética y la atenuación de ondas generadas mediante un impulso inicial, así como las escalas espaciales y temporales generadas, para de esta manera obtener una imagen lo más completa posible. Para el estudio de la atenuación, vamos a examinar dos mecanismos físicos que podrían estar involucrados en la rápida atenuación de la oscilaciones verticales observadas en bucles coronales, que son la emisión de energía mediante "wave tunneling" y absorción resonante. En este trabajo, siempre que sea posible, se van a comparar los resultados de las simulaciones temporales con las propiedades conocidas que han de poseer los modos normales. Esto nos va a servir como un método de comprobación de nuestros resultados además de ayudarnos a entender como ambas visiones están relacionadas entre si.

Por otro lado lado vamos a investigar el uso de una nueva técnica para obtener los modos normales de un sistema cuando el método estándard es difícil de llevar a cabo. Este método lo vamos aplicar a un modelo de bucle coronal recto y vamos a obtener los modos normales del sistema con el grado de precisión que deseemos mediante el uso de un criterio de convergencia.

0.3 Resum

En aquesta tesi estudiarem les oscil·lacions verticals d'una arcada potencial en l'aproximació $\beta \sim 0$ d'un plasma quan diferents perfils de densitat són considerats. Per un costat ens centrarem en l'evolució temporal d'aquest problema per tal d'analitzar l'altra cara de la moneda de les oscil·lacions magnetohidrodinàmiques, la qual tradicionalment s'ha estudiat mitjançant l'anàlisi de modes normals. Estudiarem la propagació, la conversió energètica i l'atenuació de les ones generades mitjançant un pols inicial, així com les escales espacials i temporals generades, per tal de ser capaços d'obtenir una imatge el més completa possible. Per a l'estudi de l'atenuació, examinarem dos mecanismes físics que podrien estar involucrats en la ràpida atenuació de les oscil·lacions verticals observades en els bucles coronals, que són l'emissió d'energia mitjançant "Wave tunneling" i l'absorció ressonant. En aquest treball, sempre que sigui possible, compararem els resultats de les nostres simulacions temporals amb les propietats conegudes que han de tenir els modes normals. Això ens servirà com a mètode de comprovació dels nostres resultats així com per entendre com les dues visions estan relacionades entre si.
Per altre costat investigarem l'ús d'una nova tècnica per obtenir els modes normals d'un sistema quan el mètode estàndard és difícil de dur a terme. Aquest mètode l'aplicarem a un model de bucle coronal recte i obtindrem els modes normals del sistema amb el grau de precisió que desitgem mitjançant un criteri de convergència.

Contents

Chapter 1

Introduction and basic magnetohydrodynamics

1.1 Brief introduction to the solar corona

The upper layer of the solar atmosphere is the solar corona, which extends from the top of the transition region to the Earth and beyond, with a density that decreases rather rapidly with height above the solar surface. The solar corona is an extremely hot, tenuous part of the solar atmosphere appearing in white light as streamers, plumes and other structures extending out from the chromosphere when observing the Sun during an eclipse or with a coronagraph. The basic plasma structures of the solar corona related with this work are the so-called coronal loops, conduits filled with heated plasma, shaped by the geometry of the coronal magnetic field, see Figure 1.1. The magnetic field of these structures is anchored in the relatively dense and highly conductive photospheric plasma and, hence, the photospheric footpoints are forced to follow the convective motions of the photospheric plasma. Isolated loops do not often occur and they are usually seen in active regions in coronal arcades, made of many regularly arranged loops forming a tunnel-like structure, see Figure 1.2. These coronal arcades are thought to be formed by stretching and reconnection of the magnetic field after the occurrence of a flare and may last in a stable way from days to weeks. A large variety of similar structures, with various heights, widths and lengths, can be seen in many Yohkoh pictures, see Watari et al. (1996) and Weiss et al. (1996). For a more extensive description of different structures and of the solar corona in general, see Golub (1997) and, more recently, Aschwanden et al. (2001) and Aschwanden (2005).

1.2 Coronal loops oscillations

The solar corona contains an impressively large ensemble of plasma structures that are capable of sustaining various types of waves and harmonic oscillations. Early observations of coronal oscillations were restricted to time series analysis with no spatial information. Oscillations were inferred from the temporal behavior of the intensity, width and Doppler velocity of spectral coronal lines. The situation has recently changed due to the spatial, temporal, and spectral resolution of imaging and spectroscopic instruments in current ground- and space-based observatories (SST, DST, SoHO, TRACE CoMP, Hinode, STEREO, SDO, HI-C, IRIS) have enabled us to directly image and measure motions associated to wave dynamics

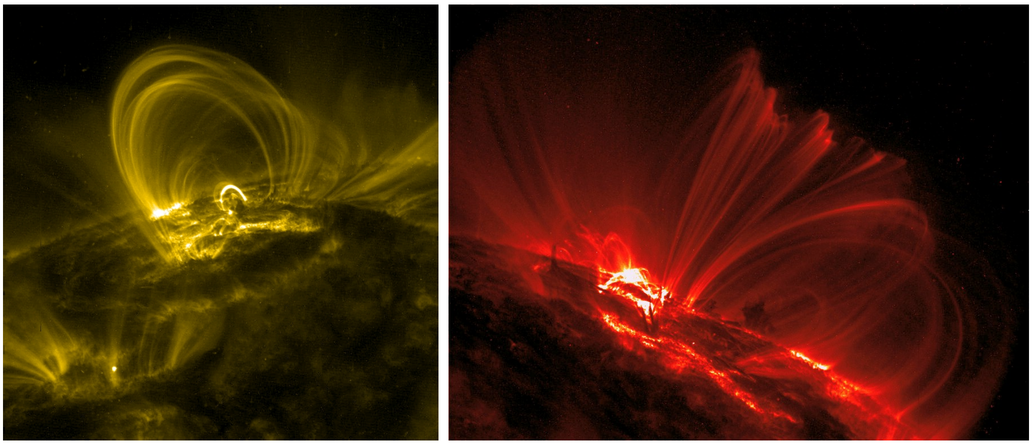

Figure 1.1: Coronal loop pictures taken with TRACE in 171 Å.

with increasing precision. Due to the improved temperature discrimination, high spatial resolution, image contrast and time cadence of these instruments, observations of the solar corona have demonstrated that the existence of oscillations in solar coronal structures are now beyond question. Also thanks to these capabilities, oscillating loops have been identified and localized in the corona and transition region. Moreover, some of their properties have also been inferred from these observations and among them a remarkable point is that these oscillations are damped in both space and time.

1.2.1 Observational evidence

As nowadays a large amount oscillations, propagating and standing waves have been reported, here we only mention some of the observed highlights to exemplify the rich variety of these phenomena and to illustrate their position in the discovery timeline.

One of the first observations of oscillations were reported by Nightingale et al. (1999) using TRACE. They saw EUV brightenings in an active region of coronal loops and interpreted them as compressional waves. Afterwards thanks to SoHO/EIT, Berghmans and Clette (1999) found propagating disturbances in coronal loops that were later interpreted as slow magnetoacustic waves by Nakariakov et al. (2000). De Moortel et al. (2000) reported on the detection of outward propagating oscillations in the footpoints of large diffuse coronal loop structures close to active regions. They suggested that these oscillations are slow magnetoacustic waves propagating along the loop. Since then, a great amount of observations were interpreted as slow modes, (see Ofman and Wang, 2002; Wang et al., 2003a,b; Terradas et al., 2004; Wang et al., 2009). For an overview of the observed longitudinal oscillations and a discussion of the observed parameters see De Moortel et al. (2002b), De Moortel et al. (2002c). Wang (2011) conducts a review of standing slow modes observed in hot coronal loops (see review by de Moortel (2009), and references within). Understanding how the waves are generated and behave as a function of the line formation temperature and the magnetic field structure is essential Mariska and Muglach (2010). They describe long period oscillations around 10 minutes observed within active regions using Hinode. As a remark, it is important to bear in mind that observations always should be complemented with theoretical or numerical modeling to complete the picture.

Among all the possible kinds of oscillations the solar coronal structures can hold, the ones related with the present study are the transverse oscillations of coronal loops which were first discovered in EUV wavelengths (171 Å) with TRACE in 1998. This phenomenon was firstly reported by Aschwanden et al. (1999); Nakariakov et al. (1999) and Aschwanden et al. (2002), namely as flare-excited transversal oscillations. Since then, a large number observations of this phenomena have been observed by Verwichte et al. (2004); Wang and Solanki (2004); Verwichte et al. (2009, 2010); Mrozek (2011); Aschwanden and Schrijver (2011); White and Verwichte (2012); Wang et al. (2012); Nisticò et al. (2013); Verwichte et al. (2013); Hindman and Jain (2014) and Anfinogentov et al. (2015). Recently, Zimovets and Nakariakov (2015) performed a large-scale investigation using SDO/AIA to better understand the excitation mechanisms for kink oscillations. Pascoe et al. (2016) examined the damping profile of a coronal loop oscillation to extract information about the the loop structure. Goddard and Nakariakov (2016) also analyzed a big number of event and estimated the physical parameters of a large number individual kink oscillations of coronal loops. See Aschwanden (2009) and De Moortel et al. (2016) for an overview and analysis of transversal, flare-excited, coronal loop oscillations and their parameters.

More general reviews of observations of various periodic and quasi-periodic oscillations in the solar atmosphere can be found in Aschwanden (1987), Tsubaki (1988) and more recently in Aschwanden et al. (1999), Roberts (2000), Aschwanden (2003) and Nakariakov and Verwichte (2005).

1.2.2 Theoretical models

Even though the detection of such perturbations is quite recent because it was necessary to wait for the high-resolution EUV imaging capabilities that can only be obtained from space, the theory of coronal magnetohydrodynamic (MHD) oscillations and waves was developed more than three decades ago and was ready for applications. The following list is not trying to be exhaustive, we only present some of the highlights of the theoretical development of coronal oscillation models related with the work being presented in this thesis.

The theoretical study of the normal modes of oscillation of coronal flux tubes were firstly done using straight magnetic cylinders by Wentzel (1979), Spruit (1981), Edwin and Roberts (1983) and Roberts et al. (1984). When flare-excited transverse oscillations were reported, they were identified by (Nakariakov and Ofman, 2001; Goossens et al., 2002; Ruderman and Roberts, 2002) as oscillations of the fast kink normal mode when a straight cylindrical tube is considered. Many other authors Poedts et al. (1985); Goossens et al. (1985); Poedts and Goossens (1988) studied the spectrum of ideal magnetohydrodynamics (MHD) of curved coronal magnetic configurations. Oliver et al. (1993, 1996) and Terradas et al. (1999) obtained the eigenmodes in potential and non-potential arcades. As a step towards more realistic structures Arregui et al. (2004a,b) considered sheared magnetic arcades configurations in the approximation of the zero-β plasma. The study of normal modes in curved configurations with coronal loops represented by density enhancements have been analyzed by (e.g., Smith et al., 1997; Van Doorsselaere et al., 2004; Terradas et al., 2006b; Verwichte et al., 2006a,b,c; Díaz et al., 2006; Van Doorsselaere et al., 2009). Coronal loops with twist magnetic field have also been modeled by several authors, see Terradas and Goossens (2012)and Ruderman

(2015). Also some authors considered more complex configurations and analyzed the collective kinklike normal modes of a system of several cylindrical loops using the T-matrix theory Luna et al. (2009).

Although it is widely accepted that the theoretical study of normal modes supplies the basis to understand the dynamics of a system, to complete the whole picture and have an accurate description, the time-dependent problem also needs to be solved. Čadež and Ballester (1995a,b) investigate analytically the temporal evolution of fast waves in a potential coronal arcade when constant Alfvén speed is considered. Using the same structure Oliver et al. (1998) inquire the properties of fast waves that are impulsively generated. Terradas et al. (2008b) considered a potential arcade embedded in a low β environment to study the properties of linear waves. Del Zanna et al. (2005) analyzed the consequences of including a transition region between the photosphere and the corona on the properties of Alfvén waves when an arcade configuration is considered. Howson et al. (2017) computed the temporal evolution of a three-dimensional magnetic flux tube to quantify the effects of twisted magnetic files on the development of the magnetic Kevin-Hemholtz instability. Antolin et al. (2017) conducted three-dimensional simulations and forward modeling of standing transverse MHD waves in coronal loops. Pagano et al. (2018); Pagano and De Moortel (2019) also ran three-dimensional MHD simulations of magnetized cylinder and a driver in the footpoint is set to trigger kink modes. Brady and Arber (2005); Murawski et al. (2005); Brady et al. (2006); Selwa et al. (2006, 2007) analyzed the consequences of the loop structure on the characteristics of fast and slow waves in curved configurations, see Terradas (2009) for a review.

Another phenomenon that is worthy to point out is the reported damping of coronal loops oscillations, see Nakariakov et al. (1999) and Aschwanden et al. (2002). Some authors believe that the wave damping can be the underlying reason of the coronal heating (see Arregui (2015); Terradas and Arregui (2018) for a wave heating review). Several mechanisms of wave damping have been proposed such as phase mixing, resonant absorption, wave leakage, gravitational stratification, magnetic field divergence, see, e.g. Aschwanden et al. (2003); Safari et al. (2007) and Ebrahimi and Karami (2016). In general, phase mixing Heyvaerts and Priest (1983) and more recently Soler and Terradas (2015); Pagano et al. (2018); Pagano and De Moortel (2019), resonant absorption (Hollweg and Yang, 1988; Goossens, 1991; Ruderman and Roberts, 2002; Goossens et al., 2002; Van Doorsselaere et al., 2004; Antolin et al., 2015, and references therein) and wave leakage by tunneling (Brady and Arber, 2005; Brady et al., 2006; Díaz et al., 2006; Verwichte et al., 2006a,b,c) are shown to be the most studied physical mechanisms for damping of the standing transverse oscillations of coronal loops. Although these are believed to be the main mechanisms behind the coronal heating, the Kevin-Hemholtz instability is also though to have major implications for wave heating the solar atmosphere due to the creation of small length scales and the generation of a turbulent regime, see Magyar and Van Doorsselaere (2016b,a); Howson et al. (2017).

The damping by resonant absorption has been studied mainly in single magnetic slabs (Terradas et al., 2005; Arregui et al., 2007b) and single magnetic cylinders (Ruderman and Roberts, 2002; Terradas et al., 2006a), for example. Also more complex equilibrium models have been considered (Van Doorsselaere et al., 2004; Terradas et al., 2006b, 2008a). More recent studies on resonant absorption are done by Magyar and Van Doorsselaere (2016b); Howson et al. (2017)For a good review on the resonant absorption mechanism see also Goossens et al. (2011). Concerning the wave tunneling mechanism, a model of a semi-circular slab was considered by Brady and Arber (2005). They excite transverse motions with a driver located at one footpoint and the results show that there are no longer confined modes, only modes that leak energy to the external medium by means of tunneling. Later, Brady et al. (2006) studied a straight cylinder model with a variable tunneling region to compare the results with the ones obtained by Brady and Arber (2005). Verwichte et al. (2006a) also analyzed a semi-circular slab with a piece-wise density whose shape can be modified by varying a parameter. Their results show that only when the Alfvén speed vary linearly with the distance to the loop center, the system can support purely trapped modes. Verwichte et al. (2006b) go beyond the study done by Verwichte et al. (2006a) and considered models where non-trapped modes can exist. They found that the resulting oscillation modes are damped by lateral leakage. In this paper the authors cataloged the modes that leak energy into leaky and tunneling. The model considered by these authors is analogous to the model used in Chapter 3 when perpendicular propagation is not considered.

1.2.3 Coronal seismology

The study of global internal solar oscillations created the discipline of helioseismology whose aim is to obtain a detailed knowledge of the physics and also of the internal physical conditions thanks to the observation and the theoretical modeling of the Sun oscillations as a whole. Following that idea Uchida (1970); Tandberg-Hanssen (1995) and Roberts et al. (1984) proposed that just like in helioseismology, coronal seismology can be used to determine physical properties of the solar atmosphere which are difficult to be measured or estimated directly. This theoretical study of the oscillatory properties of magnetic coronal structures provides us with formulae that can be used to compare our predictions with observations and help us to establish a feed-back which allows to reach a better agreement between theory and observations as well as to extract some parameters of the coronal plasma that cannot be easily measured by other means.

The first attempt to apply this method used transverse magneto-acoustic kink oscillations and was done by Aschwanden et al. (1999). In this work it was demonstrated that the fast kink mode provides the best agreement with the observed period. Nakariakov et al. (1999) used this method for the estimation of the coronal dissipative coefficients. Nakariakov and Ofman (2001) have shown the importance of the determination of coronal properties from observations, by estimating the Alfvén speed and magnetic field strength in coronal loops. Later Wang et al. (2007) also determine the coronal magnetic field. De Moortel et al. (2002a) have shown that it is possible to determine the period, damping coefficient and decay exponent of loop oscillations by means of the wavelet analysis of the time series of those oscillations. By using data analysis techniques Terradas et al. (2004) quantified the properties of the oscillatory motions of coronal loops by means of two-dimensional maps of the distribution of amplitudes inside the loop structures. Some other recent applications of coronal seismology have allowed the estimation and/or restriction of Alfvén speed in coronal loops (Zaqarashvili, 2003; Arregui et al., 2007a; Goossens et al., 2008), the transverse density structuring (Verwichte et al., 2006d) or the coronal density scale height (Andries et al., 2005). All these works are based on the detection of MHD waves in coronal structures and the application of theoretical models to extract information on the physical parameters of interest.

The initial research in the field of coronal seismology concentrates on measurements of oscillation periods, spatial displacements, damping times and temperature and density diagnostics of individual oscillating structures. For the proper development of coronal seismology, accurate theoretical models, good quality observations and effective inversion techniques are needed. Following that direction, one field that lately has addressed a lot of attention is the forward modeling, which consists in recreating observational data from the numerical models results, see Goossens et al. (2014); Antolin et al. (2014, 2015, 2017); Van Doorsselaere et al. (2018); Guo et al. (2019).

The current applications of seismological techniques have allowed us to estimate several unknown physical parameters in coronal structures. Some parameters of coronal loops that has been observed or obtained by means of the coronal seismology which are relevant for the purposes of this work are next presented. First the static magnetic structure of a coronal loop has a lateral extend whose order is around hundreds Mm and a radius over the half-width which range between $a/L = 0.02 - 0.06$. An estimation of the lower limit of the loop densities is in the range $\rho_i = 0.13 - 1.7 \times 10^9 \text{cm}^{-3}$ whereas the ratio between the external and the internal densities is assumed to be $\rho_i/\rho_e = 3 - 4$. As for the magnetic field inside the loop, $\mathbf{B}$, a value which range between $5 - 20$G is commonly accepted. Regarding the oscillatory parameters, the amplitude values stay between $100 - 8800$km whereas the period values are of the order of a few min. Finally, the damping time over the period is an important parameter for the present work and its value is between $\tau_D/P = 2 - 4$, see Aschwanden et al. (2002); Goddard and Nakariakov (2016) and De Moortel et al. (2016) for more details about all these parameters.

1.2.4 Thesis contribution to coronal loop oscillations

In this thesis we explore two theoretical ways to analyze coronal loops oscillations, i.e. solve the time-dependent problem and the normal mode problem. By doing so, our aim is to better understand how both views are related. We will increase the complexity of our model step by step in order to build a solid physical knowledge of these oscillations and we will always compare with previous known results.

In Chapter 2, which is based in (Rial et al., 2010), we follow the time-dependent approach. We have considered the propagation properties of linear fast and Alfvén waves in solar coronal arcades in the zero-β approximation without considering a density enhancement, i.e. a coronal loop. As long as the solution of this kind of problem in realistic three-dimensional configurations is not easy to handle, we have considered a simplified problem in which the magnetic equilibrium is two-dimensional, but we allow for waves to propagate with a three-dimensional character. This can be considered as a first steep towards a full three-dimensional model.

Two kinds of numerical experiments are carried out. On one hand, we consider the resonant wave energy exchange between a fast normal mode and local Alfvén waves. The results from the temporal evolution of a fast normal mode-like disturbance are analyzed in order to show how and where resonant absorption, due to three-dimensional propagation of perturbations in a non-uniform medium, takes place. It is interesting to bear in mind previous results obtained from the normal modes of coupled fast and Alfvén waves in a sheared potential arcade by Arregui et al. (2004a) because they can guide us to understand the temporal evolution of the system and the energy exchange between resonantly coupled modes. On the other hand a more complex situation is considered by analyzing the time evolution of a localized impulsive excitation which tries to mimic a nearby coronal disturbance. It is important to note that this situation is more similar to what it is possible to observe in the solar corona.

Chapter 3 is based in Rial et al. (2013). In this chapter we consider the temporal evolution of impulsively generated perturbations in a potential arcade when a new ingredient is added, i.e. a density enhancement as a model of a coronal loop. As a first approach we model the coronal loop as sharp density profile, which is unbounded in the ignorable direction of the magnetic structure. The linearized time-dependent magnetohydrodynamic equations have been numerically solved in field-aligned coordinates, which are considered the best coordinates to solve a curved problem.

The eigenmodes of curved configurations with coronal loops represented by density enhancements have been analyzed by several authors (e.g., Smith et al., 1997; Van Doorsselaere et al., 2004; Terradas et al., 2006b; Verwichte et al., 2006a,b,c; Díaz et al., 2006; Van Doorsselaere et al., 2009). In all these cases the propagation have been constrained to the plane defined by the magnetic equilibrium. The inclusion of three-dimensional propagation in straight loop models have been discussed by Arregui et al. (2007b) and several important consequences emerged, such as more spatial confinement of the modes which affect to the damping rates as well as to the frequencies of oscillation of the loops. As a result, it looks obvious that to improve our coronal loop models it is important to include the three dimensionality such as have been done by Terradas et al. (2006b). Following that direction, to make reliable temporal simulations of three-dimensional oscillations when a sudden release of energy is produced, such as happens in the solar corona, we introduce three-dimensional propagation of waves to explore if this addition allow the existence of trapped modes.

In Chapter 4, Rial et al. (2019), we investigate the application of a new technique to obtain the normal modes of a complex system. We already know that to obtain the normal modes can give us very important information about the dynamics of the system but it is also known that when we increase the complexity of the model, to obtain the normal modes by means of the standard analysis can be very difficult. For that reason we explore another way to obtain them by the application of an analysis technique called complex empirical orthogonal function, CEOF, to our time dependent solutions. This technique is an extension of the well-known principal component analysis, to which the Hilbert transform has been added. Terradas et al. (2004) have proved the utility of this tool to diagnostic information for coronal seismology when the time series comes from the observations of intensity variations. In our case we have also time series but they are the output of our temporal code. Several test are carried out to prove if this technique can provide us useful information in our case. In order to do that in this chapter we consider a straight equilibrium field model whose normal modes have been obtained theoretically by Arregui et al. (2007b). Then, the CEOF analysis is applied to the straight equilibrium temporal results and we compare the obtained CEOF modes with the theoretical ones.

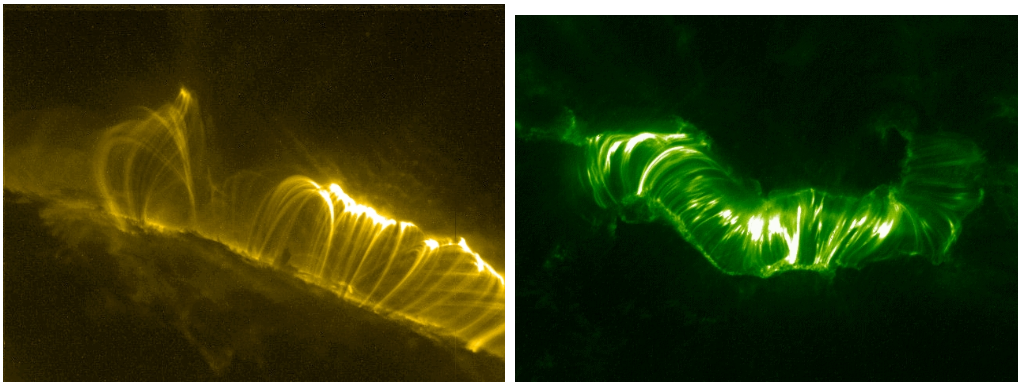

Figure 1.2: TRACE EUV images of coronal arcades, created by arranged loops forming a tunnel-like structure. Typical sizes of magnetic arcades are $100,000$ km wide and $200,000$ km long.

1.3 The equations of magnetohydrodynamics

Magnetohydrodynamics (MHD) is more a physical model than a fundamental theory, although it can be derived from kinetic theory by defining appropriate statistical (averaged) quantities, see Goedbloed and Poedts (2004). Following that direction, the plasma can be described in terms of macroscopic parameters, such as density, pressure, temperature and flow velocity. The MHD theory is accurate as long as the time scales of interest are longer than particle collision times, and the relevant length scales are longer than the particle mean free paths. In this work we consider the single fluid approach of MHD, which describes an idealized plasma treated as a continuous medium. We assume that the electromagnetic variations are non-relativistic together with a very high electric conductivity (quasi-neutrality). We also look upon the Ohm's Law as the constitutive relation between $\mathbf{E}$ and the electric density current $\mathbf{j}$ and we neglect the diffusive term in the induction equation. Although it seems we are restricting ourselves so much, it is important to say that all these requirements are well fulfilled by the dynamic phenomena of the solar corona that we are interested in. Having all that in mind, the ideal set of MHD equations are

Equation of mass continuity
$$\frac{D\rho}{Dt} + \rho\nabla\cdot\mathbf{v} = 0, \tag{1.1}$$

Equation of motion
$$\rho\frac{D\mathbf{v}}{Dt} = -\nabla p + \frac{1}{\mu_0}(\nabla\times\mathbf{B})\times\mathbf{B} + \rho\mathbf{g}, \tag{1.2}$$

Equation of energy
$$\frac{Dp}{Dt} + \gamma p\nabla\cdot\mathbf{v} = 0, \tag{1.3}$$

Induction equation
$$\frac{\partial\mathbf{B}}{\partial t} = \nabla\times(\mathbf{v}\times\mathbf{B}), \tag{1.4}$$

Solenoidal condition
$$\nabla\cdot\mathbf{B} = 0, \tag{1.5}$$

where

$$\frac{D}{Dt} = \frac{\partial}{\partial t} + \mathbf{v} \cdot \nabla, \tag{1.6}$$

is the material derivative.

These equations constitute a set of partial differential equations where $\rho(\mathbf{r}, t)$, $p(\mathbf{r}, t)$ are the density and the pressure, $\mathbf{g}$ is the gravity and $\mathbf{v}(\mathbf{r}, t)$ and $\mathbf{B}(\mathbf{r}, t)$ are the velocity and the magnetic fields. In addition μ_0 and γ are the magnetic permeability and the ratio of specific heats, respectively.

The mass continuity equation describes the evolution of the mass density, $\rho(\mathbf{r}, t)$, under the influence of a velocity field, $\mathbf{v}(\mathbf{r}, t)$. The evolution of the velocity in turn is determined by the forces on the right-hand side of the equation of motion, which are the gas pressure gradient, the Lorentz force exerted by the magnetic field and gravity. The third of these equations is the energy equation for adiabatic perturbations. Finally, we close this set of equations with the induction equation and the solenoidal condition. Strictly speaking, the solenoidal condition is nothing more than an initial condition. By taking the divergence of the induction equation one can demonstrate that $\nabla \cdot \mathbf{B}(\mathbf{r}, t)$ will be zero at any time provided that $\nabla \cdot \mathbf{B}(\mathbf{r}, t = 0) = 0$.

1.4 Magnetohydrostatic equilibria

Many solar structures of interest such as coronal loops, coronal arcades or solar prominences are observed to essentially remain in an static state for long periods of time, from days to weeks, so they can be modeled by static solutions to the MHD equations. In such equilibrium state ($\partial/\partial t = 0$, $\mathbf{v} = \mathbf{0}$), Equation (1.2) for the momentum balance becomes

$$\mathbf{0} = -\nabla p + \frac{1}{\mu_0}(\nabla \times \mathbf{B}) \times \mathbf{B} + \rho \mathbf{g}. \tag{1.7}$$

General solutions to this equation can only be obtained under particular circumstances and in order to simplify it, it is important to find out the relative importance between the terms involved. Hence, at this point it is interesting to remember that the magnetic force can be split into two parts using an elementary vector identity and can be expressed as

$$\frac{1}{\mu_0}(\nabla \times \mathbf{B}) \times \mathbf{B} = -\nabla(\frac{\mathbf{B} \cdot \mathbf{B}}{2\mu_0}) + \frac{(\mathbf{B} \cdot \nabla)\mathbf{B}}{\mu_0}, \tag{1.8}$$

where the first term represents the magnetic pressure whereas the second term represents the magnetic tension. Then we compare the gas and the magnetic pressure, which leads to the definition of the plasma-β parameter as

$$\beta = \frac{\textit{gas pressure}}{\textit{magnetic pressure}} = \frac{p}{B^2/2\mu_0} = \frac{2\mu_0 p}{B^2}. \tag{1.9}$$

A value of $\beta \gg 1$ indicates that the gas pressure dominates over the magnetic pressure (although the magnetic field is still advected by the flow) and, conversely, a value of $\beta \ll 1$ implies that the magnetic pressure dominates the plasma. In order to give a value to this parameter we use the perfect gas law for a fully ionized hydrogen plasma which states

$$p = \frac{\rho R T}{\widetilde{\mu}}, \tag{1.10}$$

with R the gas constant, T the temperature and $\widetilde{\mu}$ the mean atomic weight. The tilde placed on $\widetilde{\mu}$ is to distinguish it from the magnetic permeability, μ_0. Following Priest (1984), for realistic coronal values, $n = 5 \times 10^{-14}$ m^{-3} (particle density), $T = 2 \times 10^6$ K (temperature) and $B = 10$ G (magnetic field strength), we find

$$\beta_{corona} = 3.5 \times 10^{-21} n T B^{-2} = 3.5 \times 10^{-3} \ll 1. \tag{1.11}$$

Next we compare the magnitude of the gravity and the magnetic force terms in Equation (1.7),

$$\frac{\mid \rho \mathbf{g} \mid}{1/\mu_0 \mid (\nabla \times \mathbf{B}) \times \mathbf{B} \mid} \simeq \frac{\rho g}{B^2/L\mu_0} = \frac{p\widetilde{\mu} g/RT}{B^2/L\mu_0} = \frac{\widetilde{\mu} g L p \mu_0}{RTB^2} = \frac{\widetilde{\mu} g L \beta}{RT}. \tag{1.12}$$

Therefore, when $\beta \simeq 0$, the gravity force can also be neglected and the magnetic field dominates. In these conditions, as gravity and plasma pressure terms are negligible compared to the magnetic force, the magneto-static Equation (1.7) can be split into two equilibrium equations, one for the pressure gradient and gravity and another for the magnetic force. We next focus our attention on the static solutions obtained by the last one, which becomes

$$\frac{1}{\mu_0} (\nabla \times \mathbf{B}) \times \mathbf{B} = \mathbf{0}. \tag{1.13}$$

As we are interested in theoretically modeling vertical oscillations of coronal loops we are going to use two of the simplest solutions of Equation (1.13) namely the straight field and the potential arcade solution adding y-invariance along them. These solutions have been used to model the equilibrium fields of the coronal structures whose oscillations we are concerned about. To obtain them we assume that the current density is identically zero, so that Equation (1.13) becomes

$$\nabla \times \mathbf{B} = \mathbf{0}. \tag{1.14}$$

It is well known that when a vector field satisfies the later equation we call it a potential vector field. So that our two-dimensional equilibrium magnetic field is potential and as a consequence it is susceptible to be expressed in terms of a vector potential, commonly called flux function, $\mathbf{A} = A(x, z)\hat{e}_y$. Therefore the Cartesian components of this field can be expressed as

$$\mathbf{B} = \nabla A(x, z) \times \hat{e}_y = \left(-\frac{\partial A(x, z)}{\partial z}, 0, \frac{\partial A(x, z)}{\partial x} \right). \tag{1.15}$$

By replacing it in Equation (1.14), we obtain the Laplace's equation for the flux function,

$$\nabla^2 A(x, z) = 0. \tag{1.16}$$

Once the flux function is defined, three directions of interest can be defined. The unit vectors in the normal, perpendicular and parallel directions, which are related to the polarization of each wave type, are given by

$$\hat{e}_n = \frac{\nabla A}{\mid \nabla A \mid}, \qquad \hat{e}_\perp = \hat{e}_y, \qquad \hat{e}_\parallel = \frac{\mathbf{B}}{\mid \mathbf{B} \mid}. \tag{1.17}$$

1.4.1 Straight slab configuration

Equation (1.14) has a trivial solution which is the straight and uniform field, for example $\mathbf{B} = (0, 0, B)$, and can be expressed in terms of the flux function as

$$A(x, z) = Bx + A_0, \tag{1.18}$$

with A_0 the value of A at $z = 0$. Equation (1.18) indicates that magnetic surfaces (i.e. the surfaces of constant flux function) are planes of constant z. Regarding to the directions of interest, in this configuration using the Equation (1.17) the unit vectors are

$$\hat{e}_n = \hat{e}_x, \qquad \hat{e}_\perp = \hat{e}_y, \qquad \hat{e}_\parallel = \hat{e}_z. \tag{1.19}$$

1.4.2 Potential arcade configuration

In order to find out our second solution of interest, we solve Equation (1.16) through separation of variables, under the conditions that the solution does not diverge at infinity and that the resulting vertical component of the magnetic field vanishes at $x = 0$ (i.e. a symmetry condition). Then, the full solution for $A(x, z)$ is obtained by summing over all possible solutions

$$A(x, z) = \sum_k A_k \cos{(kx)} e^{-kz}, \tag{1.20}$$

with $k = n\pi/2L$. If we assume that only one Fourier component is taken, the one with $k_B = \pi/2L$, then the flux function is simply

$$A(x, z) = \frac{B_0}{k_B} \cos{(k_B x)} e^{-k_B z} = B_0 \Lambda_B \cos\left(\frac{x}{\Lambda_B}\right) e^{-\frac{z}{\Lambda_B}}, \tag{1.21}$$

where B_0 is the magnetic field strength at $x = 0$, $z = 0$ and $\Lambda_B = k_B^{-1} = 2L/\pi$ is the magnetic scale height. This quantity is related to the half-width of the structure, L. From Equation (1.15) the magnetic field components in the xz-plane are

$$B_x(x, z) = B_0 \cos\left(\frac{x}{\Lambda_B}\right) e^{-\frac{z}{\Lambda_B}}, \quad B_z(x, z) = -B_0 \sin\left(\frac{x}{\Lambda_B}\right) e^{-\frac{z}{\Lambda_B}}. \tag{1.22}$$

Finally it is worth to define the directions of interest in the potential arcade configuration using Equation (1.17) which are

$$\hat{e}_n = \frac{(B_z \hat{e}_x - B_x \hat{e}_z)}{\mid \mathbf{B} \mid}, \qquad \hat{e}_\perp = \hat{e}_y, \qquad \hat{e}_\parallel = \frac{(B_x \hat{e}_x + B_z \hat{e}_z)}{\mid \mathbf{B} \mid}. \tag{1.23}$$

The unitary normal and parallel orthogonal vectors together with the magnetic field lines of the potential arcade in the xz-plane, are shown in Figure 1.3.

1.4.2.1 Equilibrium density profile

Another key ingredient of the equilibrium is the static density profile. In this thesis two different density profiles are used when the potential arcade configuration is considered. Each of these density profiles allow us to model two different scenarios. One of them does not take into account the existence of a loop embedded in the arcade, while in the other, the coronal loop is modeled by means of an enhancement in the density.

Without density enhancement

The first density profile considered can be obtained by combining the equation of the hydrostatic equilibrium together with the equation of the perfect gas which leads to

$$\rho(z) = \rho_0 e^{\frac{-z}{\Lambda}}, \tag{1.24}$$

where ρ_0 is the density at $z = 0$ and Λ is the density scale height. This allows us to define a dimensionless parameter, δ, defined as the ratio of the magnetic scale height to the density scale height,

$$\delta = \frac{\Lambda_B}{\Lambda}. \tag{1.25}$$

This parameter is of relevance when considering the so-called Alfvén speed, v_A, which is defined as follows,

$$v_A^2(z) = \frac{\mid \mathbf{B} \mid^2}{\mu_0 \rho} = v_{A0}^2 e^{\frac{-(2-\delta)z}{\Lambda_B}}, \tag{1.26}$$

where $\mid \mathbf{B} \mid = (B_x^2 + B_z^2)^{1/2}$ and $v_{A0}^2 = B_0^2/\mu_0\rho_0$. Here it is important to note several details. Firstly, the Alfvén speed determines the propagation speed of magnetic waves and in this configuration only depends on z. Secondly, it is possible to select different coronal models by means of varying this parameter and there are several values of it that worth to be mentioned. On the one hand, when $\delta = 0$ we choose a coronal model of constant density, on the other hand if we fix $\delta = 2$ we choose a corona with constant Alfvén speed. Values of δ within the range $0 < \delta < 2$ model a corona with an exponentially decreasing density and Alfvén profiles, whereas values of $\delta > 2$ model a solar corona with decreasing density and increasing Alfvén speed profiles.

With density enhancement

The other density profile introduce a new ingredient which in our case is a loop with uniform density, ρ_0, embedded in a environment whose density, ρ_e, is also uniform and lower than that of the loop by a factor 10, i.e. $\rho_e = \rho_0/10$.

The combination of the this equilibrium magnetic field with this non smooth density profile leads to the following piece-wise Alfvén speed distribution

$$v_A(z) = \begin{cases} v_{A0} \exp\left(-\frac{z}{\Lambda_B}\right), & \text{inside the loop,} \\ v_{Ae} \exp\left(-\frac{z}{\Lambda_B}\right), & \text{otherwise,} \end{cases} \tag{1.27}$$

where $v_{A0} = B_0/\sqrt{\rho_0\mu_0}$ and $v_{Ae} = B_0/\sqrt{\rho_e\mu_0}$ are the Alfvén speed inside and outside the loop at the base of the corona ($z = 0$). This formula gives v_A at any point in the xz-plane. The vertical density and Alfvén speed profile at the arcade center is shown in Figure 1.4. Notice that the Alfvén speed varies both along and across magnetic field lines in our curved configuration.

1.5 Linear MHD waves

Waves are always present on the Sun because it is such a dynamic body, containing features that are continually in motion over a wide range of temporal and spatial

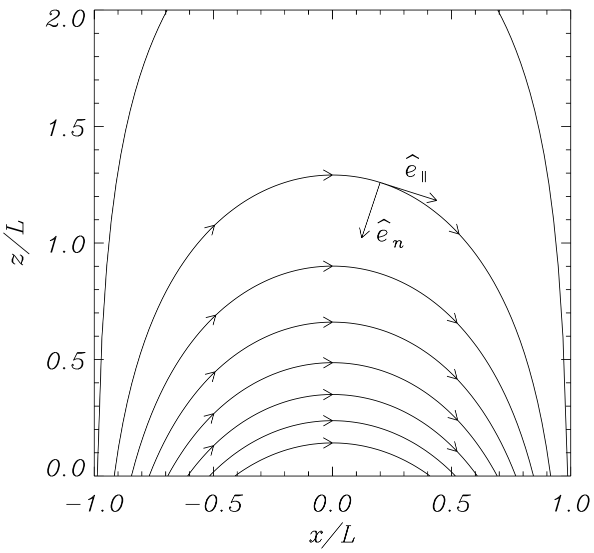

Figure 1.3: Sketch of the magnetostatic configuration of a potential coronal arcade, where the solid curves represent magnetic field lines, that are given by $A(x, z) =$ constant. These curves in the xz-plane become arcade surfaces in three dimensions. In this model z measures the vertical distance from the base of the corona (placed at $z = 0$) and L is the arcade half-width. The two orthogonal unit vectors defining the normal and the parallel directions, $\hat{e}_n$ and $\hat{e}_{\parallel}$, are also shown at a particular point.

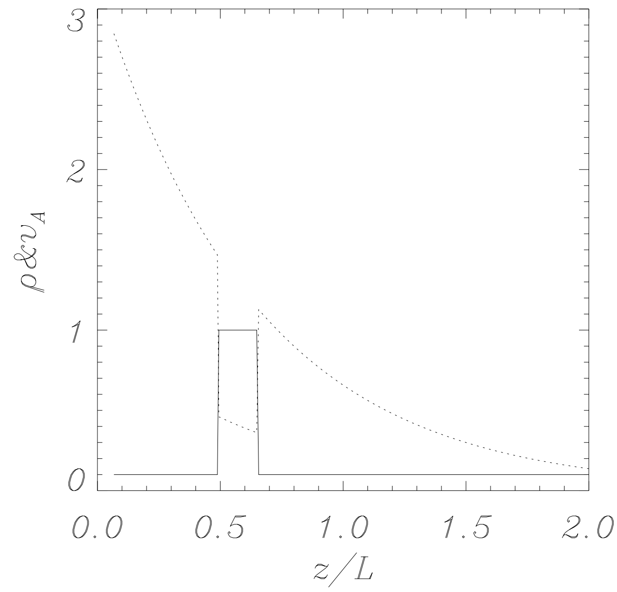

Figure 1.4: Vertical variation along the z-axis of the density (solid line) and Alfvén speed (dotted line) when a density enhancement that model a coronal loop coronal is located at a certain height, $z/L = 052$, from the base of the corona.

scales. In a plasma such as the solar atmosphere, there are typically four modes of wave motion, driven by different restoring forces. The magnetic tension and Coriolis forces can drive so-called Alfvén waves and inertial waves, respectively. The magnetic pressure, the plasma pressure and gravity can act separately and generate compressional Alfvén waves, sound waves and (internal) gravity waves, respectively; but, when acting together, these three forces produce only two magnetoacoustic gravity modes. In the absence of gravity, the two modes are referred as magnetoacoustic waves, and when the magnetic field vanishes they are called acoustic gravity waves. The aim of this section is to describe the properties of two of these modes, the Alfvén mode and the compressional Alfvén mode, also known as fast mode. These two wave modes are the relevant ones in our work.

Throughout this work we will restrict ourselves to solutions of the wave equations in the plasma $\beta = 0$ approximation. Keeping these approximations in mind, the basic equations for our discussion of waves are Equations (1.1)–(1.5) that now simplify to

$$\frac{D\rho}{Dt} + \rho\nabla\cdot\mathbf{v} = 0, \tag{1.28}$$

$$\rho\frac{D\mathbf{v}}{Dt} = \frac{1}{\mu_0}(\nabla\times\mathbf{B})\times\mathbf{B}, \tag{1.29}$$

$$\frac{\partial\mathbf{B}}{\partial t} = \nabla\times(\mathbf{v}\times\mathbf{B}), \tag{1.30}$$

$$\nabla\cdot\mathbf{B} = 0. \tag{1.31}$$

The usual procedure for the study of small amplitude oscillations is to decompose our variables in two parts. One of them is the equilibrium quantity and the other represents a small perturbation of that equilibrium, in such a way that

$$\rho_{pert} = \rho + \rho_1, \qquad \mathbf{v}_{pert} = \mathbf{v}_1, \qquad \mathbf{B}_{pert} = \mathbf{B} + \mathbf{B}_1, \tag{1.32}$$

with ρ and $\mathbf{B}$ the equilibrium density and magnetic field, and $\mathbf{v_1}$, ρ_1 and $\mathbf{B}_1$ the velocity, density and magnetic field perturbations. Note that we have assumed $\mathbf{v} = 0$, i.e. there are no flows in our equilibrium, such as corresponds to a static equilibrium.

By inserting expressions (1.32) into Equations (1.28)–(1.31), neglecting squares and products of the small perturbations and assuming a potential equilibrium magnetic field, we obtain the linear MHD wave equations in the zero-β approximation, that read

$$\frac{\partial\rho_1}{\partial t} = -\rho\nabla\cdot\mathbf{v}_1 - \mathbf{v}_1\cdot\nabla\rho, \tag{1.33}$$

$$\rho\frac{\partial\mathbf{v}_1}{\partial t} = \frac{1}{\mu_0}(\nabla\times\mathbf{B}_1)\times\mathbf{B}, \tag{1.34}$$

$$\frac{\partial\mathbf{B}_1}{\partial t} = \nabla\times(\mathbf{v}_1\times\mathbf{B}), \tag{1.35}$$

$$\nabla\cdot\mathbf{B}_1 = 0. \tag{1.36}$$

1.6 Examples of MHD waves

The theoretical study of small-amplitude oscillations and waves can be done with different techniques. The first approach is to make a normal mode analysis of the linearized MHD equations presented in the previous section which allows to obtain the spatial distribution of the eigenmodes structure together with the dispersion relation $\omega(\mathbf{k})$. An alternative approach, which is the one mainly used in this work, is to obtain the time-dependent solution of the MHD equations.

In order to review how these approaches work, several examples based on Edwin and Roberts (1982), Terradas et al. (2005), and Arregui et al. (2007b) when linear waves are superimposed on a straight field and on Oliver et al. (1993), Oliver et al. (1998), and Terradas et al. (2008b) when they are superimposed on a potential arcade field, are presented. The presentation of these works helps to contextualize as well as to give a starting point to the present thesis.

1.6.1 MHD normal modes and waves in a straight field

We first present some of the results obtained by Edwin and Roberts (1982), Terradas et al. (2005), and Arregui et al. (2007b) who modeled a solar coronal loop by means of a two-dimensional, line-tied, over-dense slab in Cartesian geometry. Their equilibrium magnetic field is straight and pointing in the z-direction, $\mathbf{B} = |\mathbf{B}|\hat{e}_z$. The coronal slab is then modeled using a varying equilibrium density profile in the x-direction, by means of a density enhancement of half-width a centered about $x = 0$. The density inside the slab, ρ_i, is constant and is connected to the constant coronal environment, ρ_e, through a sharp transition. Next two different scenarios are presented, first a purely two-dimensional problem and later a model which include three-dimensional propagation of perturbations.

In order to study the small-amplitude oscillations of the previous equilibrium, we mainly follow Arregui et al. (2007b) who obtain a set of differential equations which can be straight forward derived from our Equations (1.34) and (1.35) when the magnetic diffusivity is not neglected. They included the dissipative terms in the MHD equations because they are needed to numerically compute the resonantly-damped eigenmodes but as these terms have no physical meaning we prefer to do not write them in the following. The obtained set of equations consist in two for the perturbed velocity components (v_{1x} and v_{1y}) and three for the perturbed magnetic field components (B_{1x}, B_{1y}, and B_{1z})

$$\frac{\partial v_{1x}}{\partial t} = \frac{|\mathbf{B}|}{\mu_0 \rho}\left(\frac{\partial B_{1x}}{\partial z} - \frac{\partial B_{1z}}{\partial x}\right), \tag{1.37}$$

$$\frac{\partial v_{1y}}{\partial t} = \frac{|\mathbf{B}|}{\mu_0 \rho}\left(\frac{\partial B_{1y}}{\partial z} - \frac{\partial B_{1z}}{\partial y}\right), \tag{1.38}$$

$$\frac{\partial B_{1x}}{\partial t} = |\mathbf{B}|\frac{\partial v_{1x}}{\partial z}, \tag{1.39}$$

$$\frac{\partial B_{1y}}{\partial t} = |\mathbf{B}|\frac{\partial v_{1y}}{\partial z}, \tag{1.40}$$

$$\frac{\partial B_{1z}}{\partial t} = -|\mathbf{B}|\left(\frac{\partial v_{1x}}{\partial x} + \frac{\partial v_{1y}}{\partial y}\right). \tag{1.41}$$

Following their theoretical procedure, when the equilibrium configuration only depends on the x-coordinate, a spatial dependence of the form $\exp -i(k_y y + k_z z)$ is assumed for all perturbed quantities, with k_z and k_y being the parallel and perpendicular wavenumbers. The photospheric line-tying effect is included by imposing the velocity components vanish at $z = \pm L$ and then selecting the appropriate parallel wavenumber which is related to the lateral extend of the magnetic arcade, $2L$. The inclusion of the perpendicular wavenumber, k_y, is a feature that worth to be mentioned because although the problem is two dimensional, the previous equations include the spatial derivative with respect the y-direction to later include the perpendicular propagation of perturbations in the model.

Under these assumptions they calculated the normal modes of oscillation of this equilibrium configuration considering a temporal dependence of the form $\exp(i\omega t)$ for all perturbed quantities and allowing the frequency to be a complex number of the form $\omega = \omega_R + i\omega_I$. The resulting equations found by these authors form an eigenvalue problem which states

$$i\omega v_{1x} = \frac{|\mathbf{B}|}{\mu_0 \rho}\left(-ik_z B_{1x} - \frac{\partial B_{1z}}{\partial x}\right), \tag{1.42}$$

$$i\omega v_{1y} = \frac{|\mathbf{B}|}{\mu_0 \rho}\left(-ik_z B_{1y} + ik_y B_{1z}\right), \tag{1.43}$$

$$i\omega B_{1x} = -i|\mathbf{B}|k_z v_{1x}, \tag{1.44}$$

$$i\omega B_{1y} = -i|\mathbf{B}|k_z v_{1y}, \tag{1.45}$$

$$i\omega B_{1z} = -|\mathbf{B}|\left(\frac{\partial v_{1x}}{\partial x} - ik_y v_{1y}\right), \tag{1.46}$$

and can be combined to give a system of two ordinary differential equations for the normal and the perpendicular component of the perturbed velocity which becomes

$$\left[(k_z^2 - \partial_x^2) - \omega^2 \rho\right] v_{1x} = -k_y \frac{\partial v_{1y}}{\partial x}, \tag{1.47}$$

$$\left[(k_z^2 + k_y^2) - \omega^2 \rho\right] v_{1y} = -k_y \frac{\partial v_{1x}}{\partial x}. \tag{1.48}$$

1.6.1.1 Edwin and Roberts (1982) model

Normal mode analysis

In this section we follow the procedure described by Edwin and Roberts (1982). Therefore, if we set to zero the perpendicular wavenumber, $k_y = 0$, our Equations (1.47) and (1.48) are decoupled and they lead to the equations obtained by Edwin and Roberts (1982). We focus our attention on solutions of Equation (1.47), which are the ones associated to the fast wave. They can readily be obtained, for ρ and v_A constant, by following the usual procedure of matching different solutions in the internal and external regions and demanding the evanescence of perturbations far away from the slab. They can be classified, according to the parity of their eigenfunctions about $x = 0$, as fast kink and sausage modes. The corresponding dispersion relations are

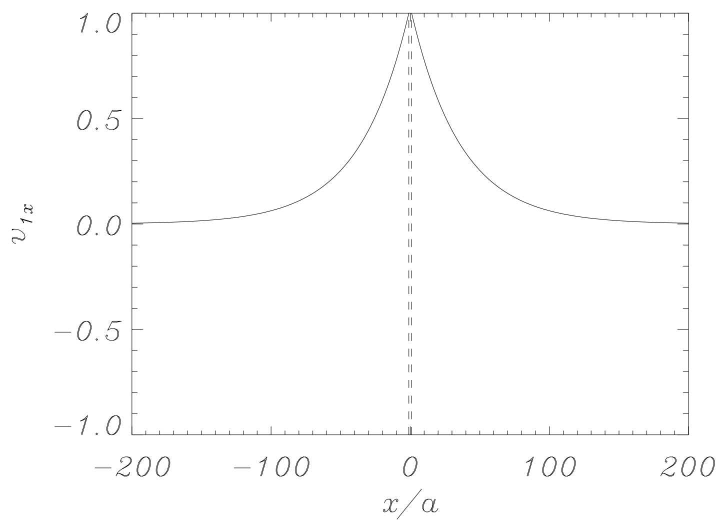

Figure 1.5: Cut at $z = 0$ of the real part of the normal velocity component, v_{1x}, for the fundamental kink mode for an equilibrium configuration with $k_z a = \pi/50$ and $\rho_i/\rho_e = 10$. Two vertical dashed lines represent where the slab is located.

$$\tanh \kappa_i a = -\frac{\kappa_e}{\kappa_i}, \tag{1.49}$$

for the kink modes (v_{1x} even about $x = 0$) and

$$\coth \kappa_i a = -\frac{\kappa_e}{\kappa_i}, \tag{1.50}$$

for the sausage modes (v_{1x} odd about $x = 0$), where

$$\kappa_e^2 = \left(k_z^2 - \frac{\omega^2}{v_{Ae}^2}\right) \quad \text{and} \quad \kappa_i^2 = \left(k_z^2 - \frac{\omega^2}{v_{Ai}^2}\right). \tag{1.51}$$

Here $v_{Ai,e} = |\mathbf{B}|\sqrt{1/\mu\rho_{i,e}}$ are the internal and external Alfvén speeds which are determined by the internal, ρ_i, and external, ρ_e, densities. We have considered the following values of density contrast, $\rho_i/\rho_e = 10$, parallel wavenumber, $k_z a = \pi/50$ and ratio of length to width of $L/2a = 25$. For our purposes is enough to show the solution obtained for the fundamental kink mode. Figure (1.5) shows the spatial distribution of a cut along the $z = 0$ axis of the perturbed normal velocity when the fundamental kink eigenmode is considered. This mode has a frequency of oscillation of $\omega a/v_{Ai} = 0.1779$.

Time-dependent analysis

From a theoretical point of view, it is interesting to study how an initial perturbation excites the different normal modes of the system. This has been accomplished by obtaining solutions of the previous model when the initial value problem of Equations (1.37)–(1.41) is solved by means of a temporal code. Terradas et al. (2005) have solved them by taking the spatial derivative with respect the y-direction, ∂_y, equal zero.

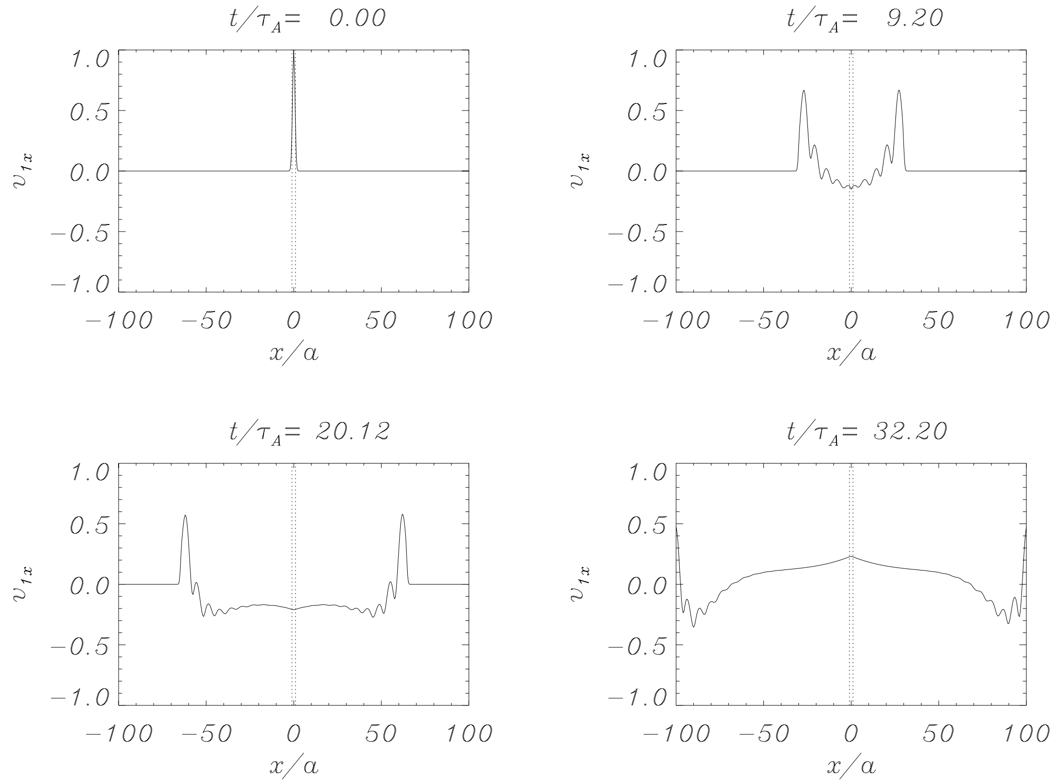

Figure 1.6: Several snapshots of the temporal evolution of a cut at $z = 0$ of the velocity component v_{1x} when a density contrast $\rho_i/\rho_e = 10$ and a perpendicular wavenumber $k_y a = 0$ are considered. In each frame the time (in units of the Alfvén transit time $\tau_A = a/v_{Ai}$) is shown on top. The system is disturbed with the initial perturbation presented in Equation (1.52) with $x_0 = 0$ and $b = 2a$. In all figures, two vertical dotted lines represent where the slab is located. See Movie 1 available in the DVD.

To mainly excite the fundamental kink mode presented in the previous section, they performed numerical simulations with an initial disturbance with its symmetry, although it is likely that such initial disturbance will excite more than one mode. The mathematical form of the initial perturbation is

$$v_{1x}(x, z) = v_{x0} \cos(k_z z) \exp - \left[\frac{(x - x_0)}{b} \right]^2, \tag{1.52}$$

where v_{x0} is the amplitude of the perturbation and k_z is the parallel wavenumber. They selected its value in order to have one maximum along the field lines. Across the field lines they chose a Gaussian profile, where x_0 is the position of the Gaussian centre and b its width at half-height. As for the boundary conditions they use line-tying at $z_{max}/a = 25$ and $z_{min}/a = -25$ and flow-through at $x_{max}/a = 200$ and $x_{min}/a = -200$.

The results of the simulation at early times are shown in Figure 1.6, where the spatial distribution of a cut along $z = 0$ of the normal velocity component is plotted at different times. The initial perturbation produces traveling disturbances to the left and right of its initial location and these disturbances exhibit some dispersion as they propagate. These traveling disturbances show that part of the initial energy

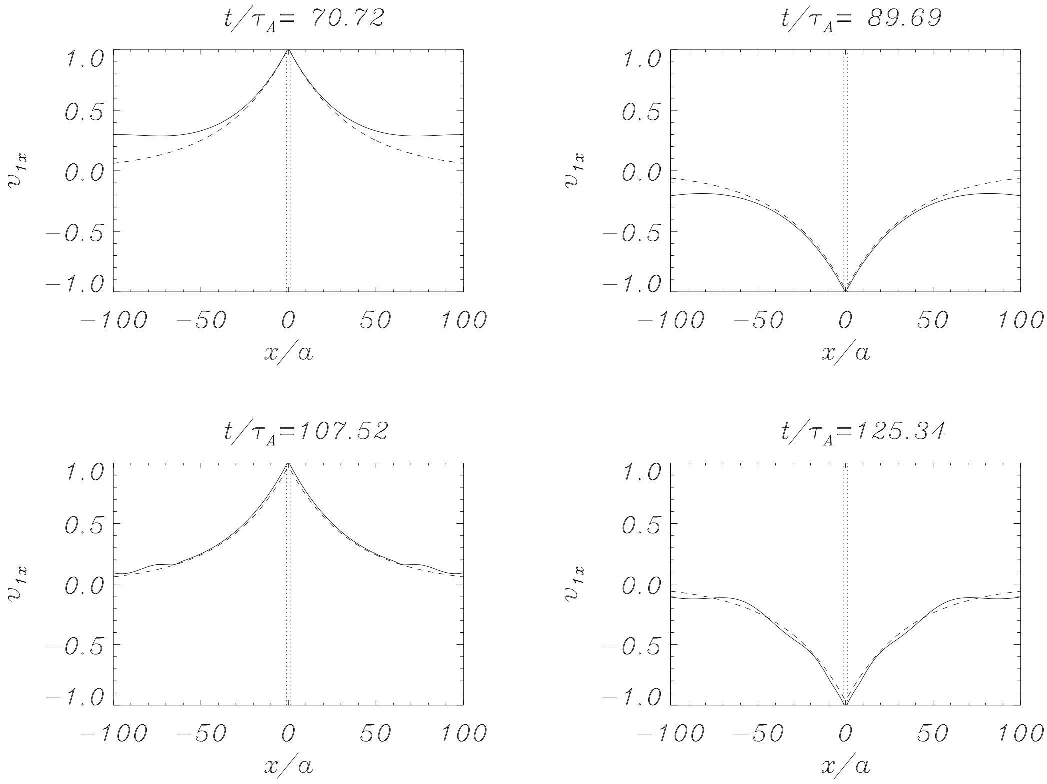

Figure 1.7: Same as Figure 1.6 but for latter times. See Movie 2 available in the DVD.

deposited in the loop is simply emitted through leaky modes, see Terradas et al. (2005) for a detailed discussion of the leaky modes. These authors refer to this phase as the impulsive leaky phase.

Once this phase ends, the shape of the velocity inside the slab and its near surroundings approaches the form of the fundamental kink mode eigenfunction which has an extremum at $x = 0$ and decreases exponentially outside the loop. In order to see it clearly, latter times of the temporal evolution are shown in Figure 1.7. In this figure we have over-plotted a dashed line which represents the temporal evolution of the theoretical fundamental kink mode presented before. Although the shape of the velocity has a good agreement with that of the normal mode, several differences are observed when we move away from the centre of the slab. These differences become smaller as the time grows which indicate the kink mode requires some time to become established. These snapshots are taken when the oscillation reaches to its maximum/minimum and reveals that both signals are oscillating with the same frequency which indicates that the slab is oscillating with this normal mode.

1.6.1.2 Arregui et al. (2007b) model

Normal mode analysis

Arregui et al. (2007b) considered the same model as Edwin and Roberts (1982) did but adding the perpendicular propagation of perturbations, i.e. $k_y \neq 0$. In order to easily compare with the results of the previous section we focus our attention in the fundamental kink mode when the same parameters are used. One

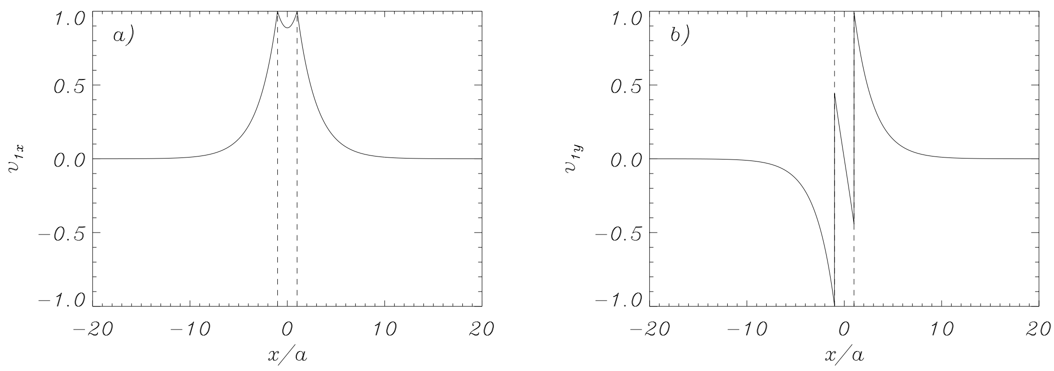

Figure 1.8: Cut at $z = 0$ of the real part of the (a) normal velocity component, v_{1x}, and (b) perpendicular velocity component, v_{1y}, of the fundamental kink mode when an equilibrium configuration with $k_z a = \pi/50$, $\rho_i/\rho_e = 10$ and $k_y a = 0.5$ is considered. Two vertical dashed lines represent where the slab is located.

of the most important consequences found by these authors is that both velocity components are coupled. This becomes clear by looking at Equations (1.47) and (1.48). Therefore, when they are solved, the normal mode spatial distribution consists in the spatial distribution given by both velocity components, v_{1x} and v_{1y}. Figure 1.8 shows a cut along the $z = 0$ axis of the perturbed normal and perpendicular velocities for the fundamental kink normal mode when the value of the perpendicular wavenumber is $k_y a = 0.5$. In this case the spatial distribution of the v_{1x} component is much less widespread over the space when it is compared to what is obtained when three-dimensional propagation is not considered, see Figures 1.8 and 1.5.

Regarding the frequency, Equations (1.47) and (1.48) lead to the dispersion relations which in this case are

$$\tanh m_i a = -\frac{\kappa_e}{\kappa_i}\frac{m_i}{m_e}, \tag{1.53}$$

for the kink modes and

$$\coth m_i a = -\frac{\kappa_e}{\kappa_i}\frac{m_i}{m_e}, \tag{1.54}$$

for sausage modes, where

$$m_e^2 = \left(k_y^2 + k_z^2 - \frac{\omega^2}{v_{Ae}^2}\right) \quad and \quad m_i^2 = \left(k_y^2 + k_z^2 - \frac{\omega^2}{v_{Ai}^2}\right). \tag{1.55}$$

Solutions to Equations (1.53) and (1.54) are found by means of a simple numerical program. Here appears another important consequence, the frequency, $\omega a/v_{Ai} = 0.101$, of this mode is lower than when propagation is constrained to the plane of the arcade, $\omega a/v_{Ai} = 0.1779$. A more detailed discussion of the solutions of this model can be found in Arregui et al. (2007b).

Next, it is possible to look for solutions to Equations (1.47) and (1.48) when an evanescent behavior of the perturbations far away from the slab is not demanded. Figure 1.9 shows a cut along the $z = 0$ axis of the perturbed normal and perpendicular velocities for a non-evanescent eigenmode. The frequency of

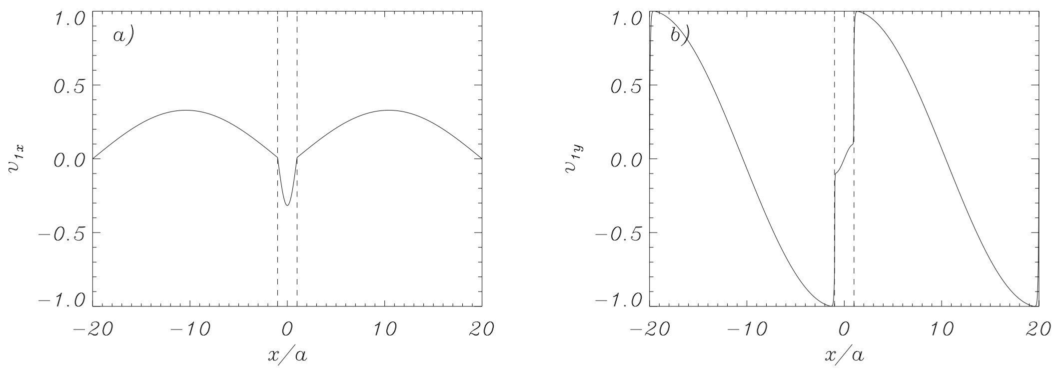

Figure 1.9: Cut at $z = 0$ of the real part of the (a) normal velocity component, v_{1x}, and (b) perpendicular velocity component, v_{1y}, for a non-evanescent eigenmode for an equilibrium configuration with $k_z a = \pi/50$, $\rho_i/\rho_e = 10$ and $k_y a = 0.5$. Two vertical dashed lines represent where the slab is located.

non-evanescent modes depends on where the limits of the domain are imposed so that it is reasonable to assert that they are not a physical modes. Having into account the numerical domain considered, we have found a non-evanescent mode whose frequency of oscillation is $\omega a/v_{Ai} = 1.675$. Here it is important to note that there are more non-evanescent eigenmodes across the field. Here we present this mode because it is the one with the simplest spatial distribution and if the flow-through boundary condition is not perfectly accomplished it is likely that can be excited. Once we know its frequency and spatial distribution if we find some of its signatures in the temporal simulations we can be sure about its non-physical nature.

Time-dependent analysis

In order to compare with normal mode solutions, Arregui et al. (2007b) obtain temporal solutions of Equations (1.42)–(1.46). As we focus on the excitation of the fundamental kink mode we present their performed numerical simulations with a symmetric initial disturbance of the form described in Equation (1.52).

A cut along $z = 0$ of the spatial distribution of the normal and perpendicular velocity components is plotted in Figure 1.10 at different times. After the impulsive leaky phase, the spatial distribution of both components reveals two extrema at the edges of the slab with an amplitude decreasing as we move away from them. In this figure we have over-plotted in a dashed line the same cut but done to the spatial distribution of the theoretical normal mode presented in Figure 1.8 which has a frequency $\omega a/v_{Ai} = 0.101$. Qualitatively we observe very similar results to the normal mode both spatially and temporally which allow to state that the fundamental kink mode has been excited. Regardless, several differences exist in the last two snapshots at the centre of the slab between the excited modes and the normal mode. This indicates that although the fundamental kink mode is mainly excited, other modes also have been excited through the initial Gaussian perturbation.

In Figure 1.11a the temporal evolution of the normal velocity component, v_{1x}, is presented at the loop center ($x = 0$, $z = 0$) as solid line, while the perpendicular velocity component, v_{1y}, is presented at the loop border ($x = 1$, $z = 0$) as a dotted

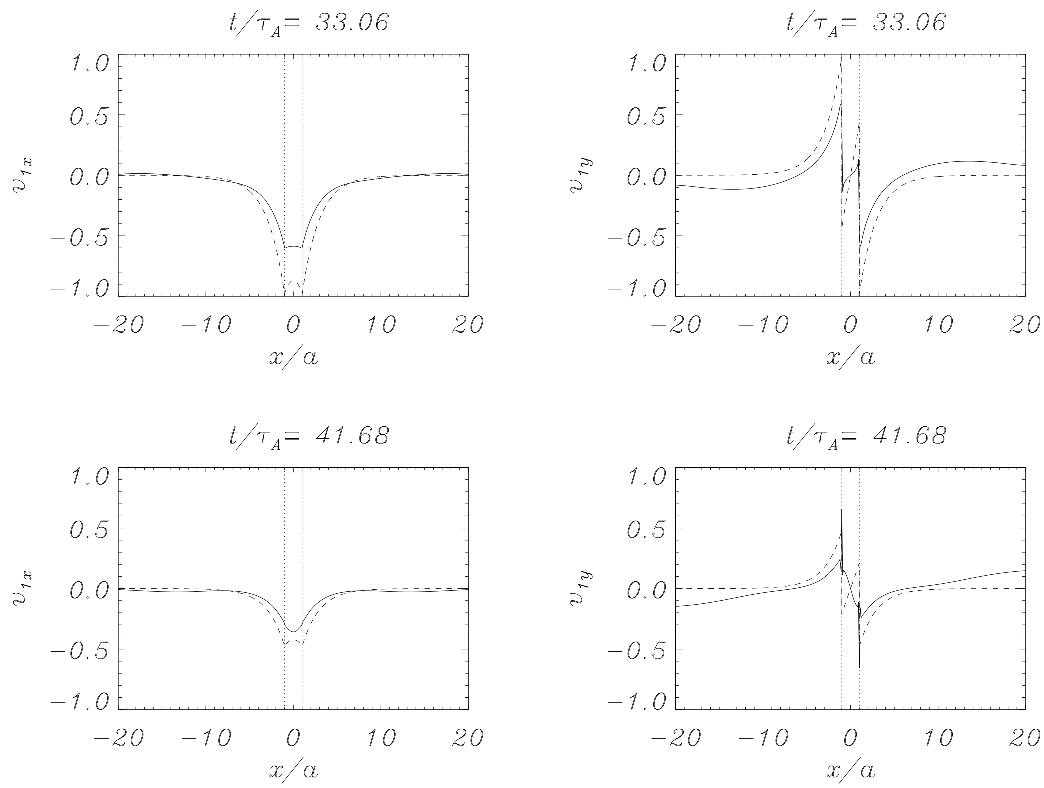

Figure 1.10: Several snapshots of the temporal evolution of a cut along $z = 0$ of the normal, v_{1x}, and the perpendicular, v_{1y}, velocity components when a density contrast $\rho_i/\rho_e = 10$ and a perpendicular wavenumber $k_y a = 0.5$ are considered. In each frame the time (in units of the Alfvén transit time $\tau_A = a/v_{Ai}$) is shown on top. The system is disturbed with the initial perturbation presented in Equation (1.52) with $x_0 = 0$ and $b = 2a$. The dashed line is the temporal evolution of the theoretical fundamental kink mode presented in Figure 1.8. In all figures, two dotted vertical lines represent where the slab is located. See Movie 3 available in the DVD.

line. At first sight the signals reveal several frequencies contributing in those points. On one hand, the low frequency could be associated with the fundamental kink mode whereas the high frequency's character is not clear.

To find out which modes are excited a frequency analysis of the signals presented in Figure 1.11a is done and then its results are compared with the theoretical results obtained before. Indeed due to the different range of frequencies involved, two frequency analysis are done to both signals, one in the lower and other in the high frequency range. Figure 1.11b shows the frequency analysis done in the low frequency range, $[0, 0.2]$, where only a frequency with a value of $\omega a/v_{Ai} = 0.101$ is obtained. This frequency matches the frequency predicted for the fundamental kink normal mode in the theoretical section. Whereas the frequency analysis done in the high frequency range, $[1, 2]$, presented in Figure 1.11c reveals two main frequencies with numerical values $\omega a/v_{Ai} = 1.59$ and 1.675. From the theoretical analysis of non-evenescent solutions we found a mode whose frequency coincides with the value $\omega a/v_{Ai} = 1.675$, see Figure 1.9, but the same does not apply to the frequency $\omega a/v_{Ai} = 1.59$ whose theoretical representation can not be found. Notwithstanding to definitively assert if the founded frequencies $\omega a/v_{Ai} = 0.101$

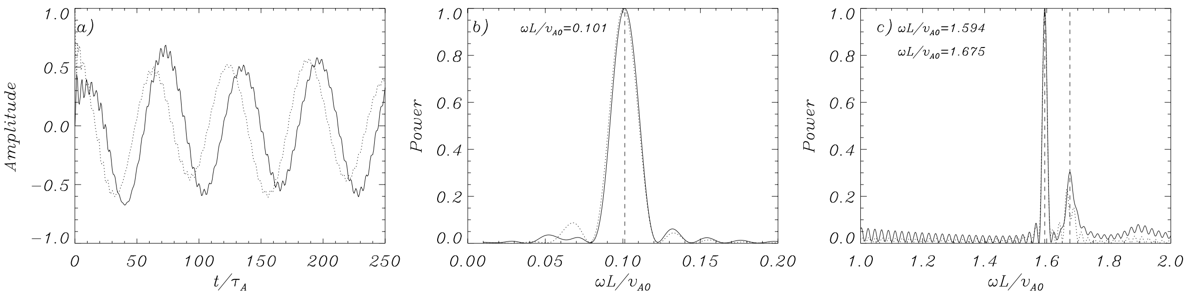

Figure 1.11: a) Temporal evolution of the velocity component v_{1x} (solid line) at the center of the loop ($x = 0$, $z = 0$), and v_{1y} (dotted line) at the border of the loop ($x = 0$, $z = 1$). (b) Power spectra of the signals shown in (a) in the low frequency range. (c) Power spectra of the signals shown in (a) in the high frequency range. The vertical lines correspond to the frequencies obtained

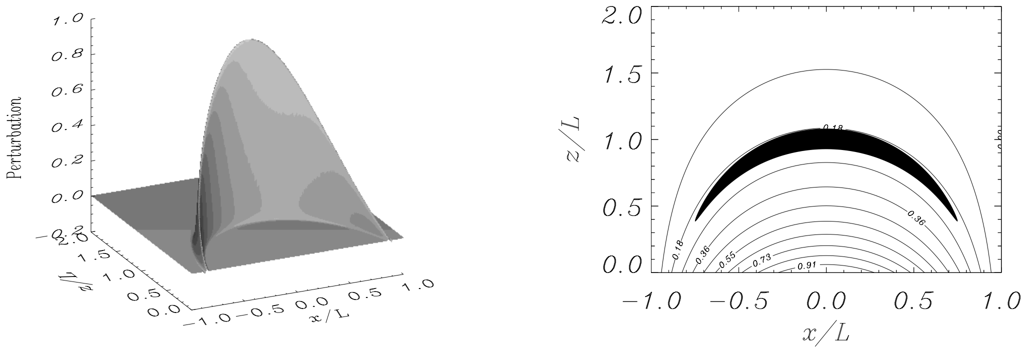

Figure 1.12: Plot of the normal mode-like initial perturbation on v_{1y}. The initial perturbation, see Equation (1.61), is centered at $x = 0$ and $z_0/L = 1$.

and 1.675 correspond to the theoretical modes obtained in the previous sections some additional proofs, which will be given later, are necessary.

1.6.2 Alfvén modes and waves in a two-dimensional potential arcade

We next present another example of MHD waves superimposed to a static magnetic structure which is the potential arcade introduced in § 1.4.2. This is a more complex model of a coronal structure due to the introduction of field curvature and non-uniformity of density and Alfvén speed. The main properties of MHD waves in two-dimensional curved structures have been studied by several authors from both a normal mode as well as a time-dependent point of view. In this section we present some of the results obtained by Oliver et al. (1993) and Terradas et al. (2008b).

They choose a potential arcade model whose boundaries are placed at $x = \pm L$, $z = 0$ and $z = 2L$, with L the half-width of the potential coronal arcade. Using this model, different density profiles produce different Alfvén speed configurations, see Equations (1.24) and (1.26) and these authors can select different equilibria by changing the value of the δ-parameter presented in Equation (1.26). Something

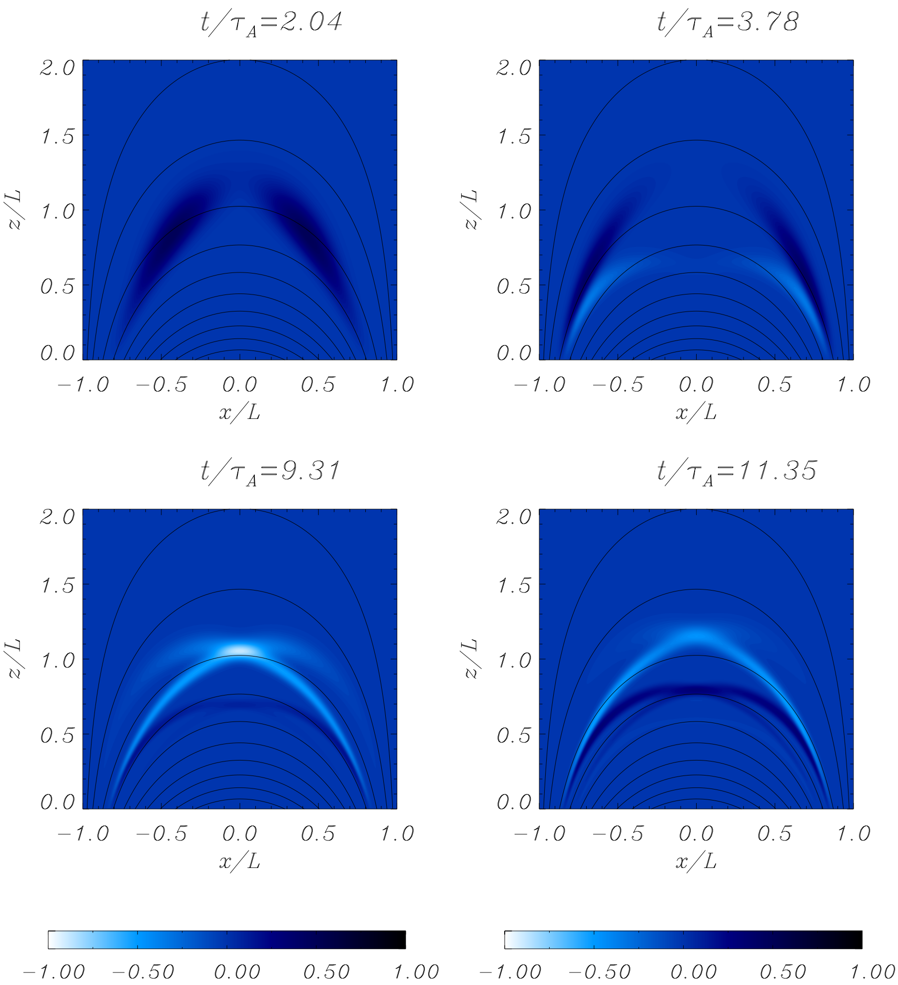

Figure 1.13: Alfvén wave: time evolution of the velocity component, v_{1y}, for $\delta = 0$. The initial perturbation in v_{1y} is a Gaussian profile with $x_s = 0$, $z_s = 1$, $a = 0.2L$ and $v_s = 1$. In each frame the time (in units of the Alfvén transit time $t/\tau_A = L/v_{A0}$) is shown on top. Black solid lines represent the magnetic field lines of the coronal arcade. See Movie 4 in the DVD.

that worth to mention is that when this equilibrium magnetic field is taken Oliver et al. (1993) and others have proved advantageous to use the field-related components, see Equation (1.23) and Figure 1.3, instead of Cartesian components.

Concerning the boundary conditions applied, they use the line-tying condition at $z = 0$ and flow-through conditions in the rest of the domain (top and lateral walls).

Normal mode analysis

As has been proved, it is useful to firstly study the properties of normal modes before going for the temporal solutions. Therefore, we are going to review several properties of the Alfvén normal modes of this system which have been obtained by Oliver et al. (1993).

According to Oliver et al. (1993), when $\delta = 0$ the analytic solution for the Alfvén normal mode is given by

$$\hat{v}_{1y} = C \sin k_x (x - x_0), \tag{1.56}$$

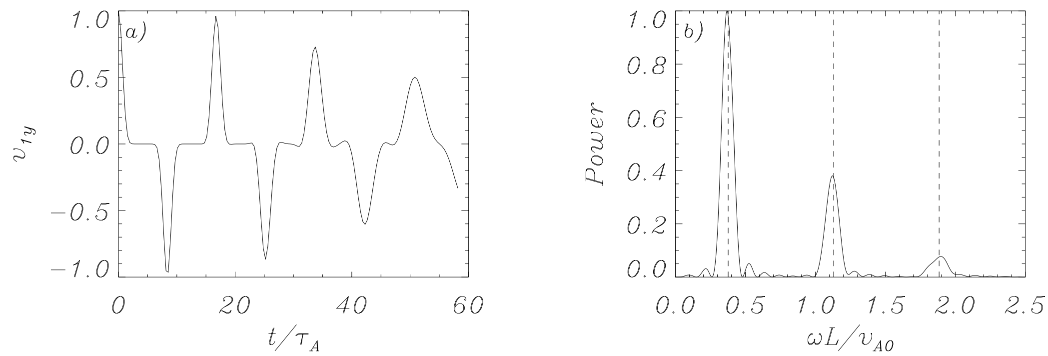

Figure 1.14: (a) Alfvén wave velocity at $x = 0$, $z/L = 1$ as a function of time. (b) Power spectrum of the signal in (a). Vertical dashed lines give the frequencies of the fundamental mode and its first harmonics coming from Equation (1.59) with $z_m/L = 1$.

where the wavenumber, k_x, and the frequency, ω, are related by the dispersion equation

$$\omega = k_x v_{A0} \cos\left(\frac{x_0}{\Lambda_B}\right), \tag{1.57}$$

with v_{A0} the Alfvén speed at $z = 0$ and x_0 the position of the magnetic field line footpoint, i.e. the place at which the field line reaches the base of the corona ($z = 0$). From Figure 1.3 it is clear that the length of the magnetic field line depends on the footpoint position. In this figure it is also clear that the maximum height of the field lines, z_m, is related to their footpoint position. This relation is given by

$$z_m = -\Lambda_B \log\left\{\cos\left(\frac{x_0}{\Lambda_B}\right)\right\}, \tag{1.58}$$

and so Equation (1.57) can be written as

$$\omega = k_x v_{A0} \exp\left(\frac{-z_m}{\Lambda_B}\right). \tag{1.59}$$

After imposing the boundary conditions (line-tying condition) to the solution, we obtain the following expression for the horizontal wavenumber.

$$k_x = \tfrac{n\pi}{2x_0}, \quad \text{with} \quad n = 1, 2, 3 \ldots \tag{1.60}$$

The solutions of this problem should depend on x and z, but we have to remember that x and z are related via the flux function, see Equation (1.21). Also it is important to note that these solutions have a well-defined parity with respect to the x-direction depending if n is chosen even or odd. Therefore, the ideal two-dimensional solution for $v_y(x, z)$ consists of a highly anisotropic solution confined to a particular magnetic surface (described by a uniform flux function $A(x, z)$), and can be written as

$$v_{1y}(x, z) = \hat{v}_{1y}(x)\delta(A(x, z) - A(x = 0, z_m)), \tag{1.61}$$

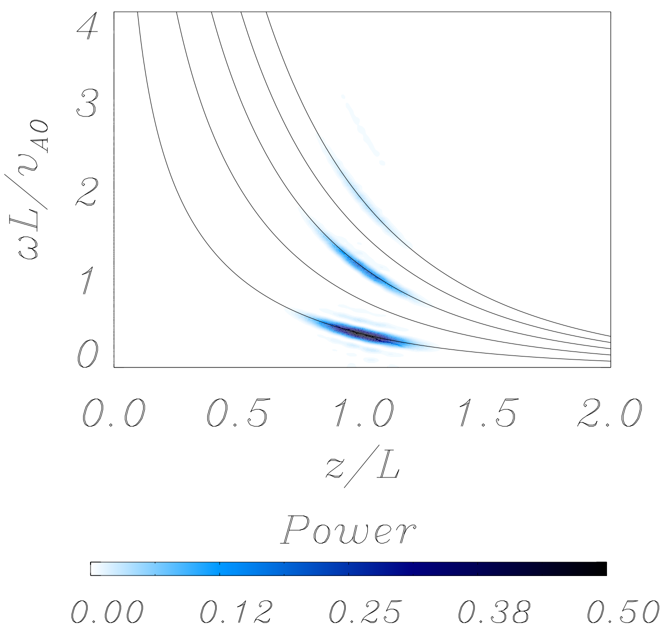

Figure 1.15: The colored contours are the power spectrum of v_{1y} at $x = 0$ as a function of maximum height of the field lines, z/L, and normalized frequency, $\omega L/v_{A0}$. From bottom to top different solid lines are the theoretical frequency of the fundamental mode and its harmonics for $\delta = 0$ given by Equation (1.59).

where z_m gives the maximum height of the field line at which the normal mode is excited. Figure 1.12 plots the shape of an Alfvén normal mode-like which consists in a sum of several Alfvén normal modes presented in Equation (1.61).

Time-dependent analysis

Once the Alfvén normal modes are introduced, we present the temporal results obtained by Terradas et al. (2008b). These authors initially disturb the velocity field of the system to obtain time-dependent solutions. They considered a disturbance which initially has (at time $t/\tau_A = 0$) the form

$$v_1 = v_s \exp - \left(\frac{(x - x_s)^2 + (z - z_s)^2}{a^2} \right), \tag{1.62}$$

where v_s is the amplitude of the velocity perturbation, x_s and z_s are the coordinates of the perturbation's center, and a is the width of the two-dimensional Gaussian profile at half height.

In this system a general perturbation can excite fast and Alfvén waves at the same time, but in order to better understand their features they impose in the initial velocity the dominant component of the particular MHD wave that they are interested in, whereas all other variables are initially set to zero. Therefore as they want to generate Alfvén waves, the Gaussian perturbation presented in Equation (1.62) is initially set in the v_{1y} component.

Figure 1.13 shows how the perturbation splits into two wave packets strictly traveling along the magnetic field lines. The initial circular shape of the perturbation changes as the wave packet moves towards the photosphere. This is basically due to two effects. First, the Alfvén speed is not uniform so the different parts of the disturbance travel at different velocities. Second, since in this equilibrium the magnetic field lines converge toward the photosphere, wave packets traveling along them tend to shrink for downward-propagating waves. The opposite effect happens for an upward-propagating wave. The conclusion is that the topology of magnetic field lines plays an important role for Alfvén waves.

In the present case we are also able to compare the numerical results with analytical expressions. One must take into account that for long times, waves bouncing at the base of the corona travel back and forth along filed lines and give rise to standing Alfvén oscillations in and around a particular field surface. Thus, a power spectrum of the v_{1y} component should reveal power peaks at the frequencies given by Equation (1.59). The v_{1y} signal at $x = 0$ and $z/L = 1$ and its corresponding power spectrum are presented in Figure 1.14. The temporal evolution at this point reveals a signal composed of several frequencies and this is later confirmed by the spectral analysis, which shows three main frequencies contributing to the signal. In Figure 1.14b also are shown the analytical frequencies obtained by Equation (1.59) as vertical lines and a good agreement between them has been found.

Next we repeat the spectral analysis of these oscillations for all the different heights of the structure. The results are shown in Figure 1.15. As described by Oliver et al. (1993), Alfvén waves are characterized by a continuous spectrum of frequencies, with motions in the v_{1y} component localized in magnetic surfaces with constant flux function $A(x, z)$. Therefore Equation (1.57) implies that different magnetic surfaces with different footpoints have different Alfvén frequencies. In Figure 1.15 the resulting power spectrum is compared to the Alfvén continuum frequencies obtained by Oliver et al. (1993). The power associated with the generated Alfvén waves coincides with the theoretical normal mode frequencies of the system at all heights and give us further confidence on the goodness of our code. But more properties of Alfvén waves are observed. In this figure Alfvén waves stay confined to the vertical range of magnetic surfaces that were excited by the initial disturbing (few magnetic surfaces) since Alfvén waves being incompressible, can not propagate energy across magnetic field lines. Also is clear how the initial perturbation is decomposed by the system in a linear combination of normal modes, but keeping the even parity with respect to $x = 0$ of the initial disturbance, so energy is found in the fundamental mode, the second harmonic, etc.

Chapter 2

Three-dimensional propagation of MHD waves in solar coronal arcades. Rial et al. (2010)

The Astrophysical Journal, 713:651–661, 2010 April 10 doi:10.1088/0004-637X/713/1/651

THREE-DIMENSIONAL PROPAGATION OF MAGNETOHYDRODYNAMIC WAVES IN SOLAR CORONAL ARCADES

S. Rial[1], I. Arregui[1], J. Terradas[1,2], R. Oliver[1], and J. L. Ballester[1]
[1] Departament de Física, Universitat de les Illes Balears, E-07122 Palma de Mallorca, Spain; samuel.rial@uib.es, inigo.arregui@uib.es, jaume.terradas@uib.es, ramon.oliver@uib.es, joseluis.ballester@uib.es
[2] Centrum voor Plasma Astrofysica, K.U. Leuven, Celestijnenlaan 200B, B-3001 Heverlee, Belgium
Received 2010 February 1; accepted 2010 March 1; published 2010 March 24

ABSTRACT

We numerically investigate the excitation and temporal evolution of oscillations in a two-dimensional coronal arcade by including the three-dimensional propagation of perturbations. The time evolution of impulsively generated perturbations is studied by solving the linear, ideal magnetohydrodynamic (MHD) equations in the zero-β approximation. As we neglect gas pressure, the slow mode is absent and therefore only coupled fast MHD and Alfvén modes remain. Two types of numerical experiments are performed. First, the resonant wave energy transfer between a fast normal mode of the system and local Alfvén waves is analyzed. It is seen how, because of resonant coupling, the fast wave with global character transfers its energy to Alfvénic oscillations localized around a particular magnetic surface within the arcade, thus producing the damping of the initial fast MHD mode. Second, the time evolution of a localized impulsive excitation, trying to mimic a nearby coronal disturbance, is considered. In this case, the generated fast wavefront leaves its energy on several magnetic surfaces within the arcade. The system is therefore able to trap energy in the form of Alfvénic oscillations, even in the absence of a density enhancement such as that of a coronal loop. These local oscillations are subsequently phase-mixed to smaller spatial scales. The amount of wave energy trapped by the system via wave energy conversion strongly depends on the wavelength of perturbations in the perpendicular direction, but is almost independent from the ratio of the magnetic to density scale heights.

Key words: Sun: atmosphere – Sun: corona – Sun: evolution – Sun: oscillations

Online-only material: animations, color figures

1. INTRODUCTION

The presence of waves and oscillations in the solar corona is a well-known feature that has been observed for long time. For an overview of the early observational background, see Tsubaki (1988). Nowadays, because of the increasing spatial and temporal resolution of the EUV instruments onboard the *Transition Region and Coronal Explorer* (*TRACE*), the *Solar and Heliospheric Observatory* (*SOHO*), and the *Hinode* spacecraft, accurate observations of oscillations in different coronal structures are accomplished. Many authors have reported observations of transversal coronal loop oscillations from both ground and space-based instruments (Aschwanden et al. 1999; Nakariakov et al. 1999; Aschwanden et al. 2002; Schrijver et al. 2002). When these observations are compared with theoretical models (Roberts et al. 1984; Nakariakov et al. 1999; Nakariakov & Ofman 2001), the possibility of inferring some plasma parameters, otherwise difficult to measure, and of improving the existing theoretical models is open; see Banerjee et al. (2007) for a review. Magnetohydrodynamics (MHD) is the underlying theory of coronal seismology and it is believed that all these observed oscillations and waves can be interpreted theoretically in terms of MHD modes of different coronal plasma structures.

The theoretical study of these oscillations and waves can be done from several points of view. The first approach is to make a normal mode analysis of the linearized MHD equations, which allows to obtain the spatial distribution of the eigenmodes of the structure together with the dispersion relation $\omega(\mathbf{k})$. Once the elementary building blocks of the MHD normal mode theory are described, the main properties of the resulting MHD waves can be outlined. Many authors have explored the normal modes of coronal structures, beginning with very simple cases such as the straight and infinite cylinder (Edwin & Roberts 1983). In the context of curved coronal magnetic structures, Goossens et al. (1985); Poedts et al. (1985); Poedts & Goossens (1988) investigated the continuous spectrum of ideal MHD. Oliver et al. (1993, 1996) and Terradas et al. (1999) derived the spectrum of modes in potential and non-potential arcades. More complex configurations, such as sheared magnetic arcades in the zero-β plasma limit, have been studied by Arregui et al. (2004a, 2004b). Other authors have studied eigenmodes in curved configurations with density enhancements that represent coronal loops (e.g., Van Doorsselaere et al. 2004; Terradas et al. 2006; Verwichte et al. 2006a, 2006b, 2006c; Díaz et al. 2006; Van Doorsselaere et al. 2009).

An alternative approach is to obtain the time-dependent solution of the MHD equations. Using this method, Čadež & Ballester (1995a, 1995b) studied analytically the propagation of fast waves in a two-dimensional coronal arcade for a particular equilibrium, namely one with uniform Alfvén speed. Oliver et al. (1998) studied the effect of impulsively generated fast waves in the same coronal structure. Del Zanna et al. (2005) studied the properties of Alfvén waves in an arcade configuration, including the transition region between the photosphere and the corona. Other studies have analyzed the effect of the loop structure on the properties of fast and slow waves in two-dimensional curved configurations (see, e.g., Murawski et al. 2005; Brady & Arber 2005; Brady et al. 2006; Selwa et al. 2006, 2007), see Terradas (2009) for a review.

The main aim of this paper is to analyze the effect of including three-dimensional propagation on the resulting MHD waves as a first step before considering more realistic situations like the one observed by Verwichte et al. (2004), where the effect of three-dimensional propagation is clear. In our model, there is no density enhancement like that of a loop and the zero-β approximation is assumed, so only the fast and Alfvén modes are present. We focus our attention on the mixed properties displayed by the generated MHD waves that arise due to the coupling when longitudinal propagation is allowed. The paper is arranged as follows. In Section 2, we briefly describe the equilibrium configuration as well as some of the approximations made in this work. In Section 3, we present our derivation of the linear ideal MHD wave equations with three-dimensional propagation of perturbations. In Section 4, the numerical code used in our study is described, together with several checks that have been performed by solving problems with known analytical or simple numerical solution. Our main results are shown in Section 5, where the linear wave propagation properties of coupled fast and Alfvén waves in a two-dimensional coronal arcade, allowing three-dimensional propagation, are described. Finally, in Section 6 the conclusions are drawn.

2. EQUILIBRIUM CONFIGURATION

We model a solar coronal arcade by means of a two-dimensional potential configuration contained in the xz-plane in a Cartesian system of coordinates (see Oliver et al. 1993). For this y-invariant configuration, the flux function is

$$A(x, z) = B\Lambda_B \cos\left(\frac{x}{\Lambda_B}\right) \exp\left(-\frac{z}{\Lambda_B}\right), \quad (1)$$

and the magnetic field components are given by

$$B_x(x, z) = B \cos\left(\frac{x}{\Lambda_B}\right) \exp\left(-\frac{z}{\Lambda_B}\right),$$
$$B_z(x, z) = -B \sin\left(\frac{x}{\Lambda_B}\right) \exp\left(-\frac{z}{\Lambda_B}\right). \quad (2)$$

In these expressions, Λ_B is the magnetic scale height, which is related to the lateral extent of the arcade, L, by $\Lambda_B = 2L/\pi$, and B represents the magnetic field strength at the photospheric level ($z = 0$). The overall shape of the arcade is shown in Figure 1.

In this paper, gravity is neglected and the $\beta = 0$ approximation is used for simplicity. Therefore, the equilibrium density can be chosen arbitrarily. We adopt the following one-dimensional profile:

$$\rho_0(z) = \rho_0 \exp\left(-\frac{z}{\Lambda}\right), \quad (3)$$

where Λ is the density scale height and ρ_0 is the density at the base of the corona. As shown by Oliver et al. (1993), the combination of magnetic field components given by Equation (2) with the density profile given by Equation (3) leads to a one-dimensional Alfvén speed distribution in the arcade that can be cast as

$$v_A(z) = v_{A0} \exp\left[-(2-\delta)\frac{z}{2\Lambda_B}\right]. \quad (4)$$

Here, $\delta = \frac{\Lambda_B}{\Lambda}$ represents the ratio of the magnetic scale height to the density scale height and v_{A0} is the Alfvén speed at the base of the corona. The δ parameter completely determines the behavior of the Alfvén speed profile and hence the wave propagation properties. The case $\delta = 2$ represents a uniform Alfvén speed model, while $\delta = 0$ corresponds to an exponentially decreasing Alfvén speed in a uniform density configuration. Other values of δ represent situations in which both the Alfvén speed and density depend on height in a different manner.

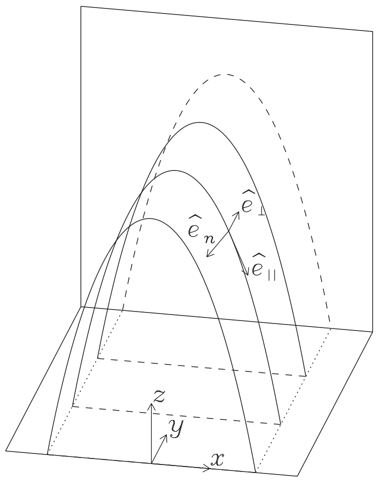

Figure 1. Sketch of the magnetostatic configuration of a potential coronal arcade, where the solid curves represent magnetic field lines, given by $A(x, z) =$ constant. These curves in the xz-plane become arcade surfaces in three dimensions. In this model, z measures the upward distance from the base of the corona (placed at $z = 0$). The three orthogonal unit vectors, $\hat{\mathbf{e}}_n$, $\hat{\mathbf{e}}_\perp$, and $\hat{\mathbf{e}}_\parallel$, defining the normal, perpendicular, and parallel directions, respectively, are also shown at a particular point.

3. LINEAR WAVES

In order to study small amplitude oscillations in our potential arcade, the previous equilibrium is perturbed. For linear and adiabatic MHD perturbations in the zero-β approximation, the relevant equations are

$$\rho_0 \frac{\partial \mathbf{v}_1}{\partial t} = \frac{1}{\mu_0}(\nabla \times \mathbf{B}) \times \mathbf{B}_1 + \frac{1}{\mu_0}(\nabla \times \mathbf{B}_1) \times \mathbf{B}, \quad (5)$$

$$\frac{\partial \mathbf{B}_1}{\partial t} = \nabla \times (\mathbf{v}_1 \times \mathbf{B}), \quad (6)$$

where μ_0 is the magnetic permeability of free space and the subscript "1" is used to represent perturbed quantities. These equations are next particularized to our two-dimensional potential arcade equilibrium. As the equilibrium is invariant in the y-direction, we can Fourier analyze all perturbed quantities in the y-direction by making them proportional to $\exp(ik_y y)$. In this way, three-dimensional propagation is allowed and each Fourier component can be studied separately. As a result of this Fourier analysis, the perpendicular perturbed velocity and magnetic field components appear accompanied by the purely imaginary number $i = \sqrt{-1}$. This is undesirable from a practical point of view, since Equations (5) and (6) will be solved numerically and the code is designed to handle real quantities only. Nevertheless, by making the appropriate redefinitions, namely $v_{1y} \equiv i\tilde{v}_{1y}$ and $B_{1y} \equiv i\tilde{B}_{1y}$, it turns out that our wave equations can be cast in the following form:

$$\frac{\partial v_{1x}}{\partial t} = \frac{1}{\mu_0 \rho_0}\left[\left(\frac{\partial B_{1x}}{\partial z} - \frac{\partial B_{1z}}{\partial x}\right) B_z\right], \quad (7)$$

$$\frac{\partial \tilde{v}_{1y}}{\partial t} = \frac{1}{\mu_0 \rho_0}\left[\left(B_x \frac{\partial \tilde{B}_{1y}}{\partial x} + B_z \frac{\partial \tilde{B}_{1y}}{\partial z}\right) + k_y (B_{1x} B_x + B_{1z} B_z)\right], \quad (8)$$

$$\frac{\partial v_{1z}}{\partial t} = -\frac{1}{\mu_0 \rho_0}\left[\left(\frac{\partial B_{1x}}{\partial z} - \frac{\partial B_{1z}}{\partial x}\right) B_x\right], \tag{9}$$

$$\frac{\partial B_{1x}}{\partial t} = -k_y \tilde{v}_{1y} B_x - \frac{\partial}{\partial z}\left(v_{1z} B_x - v_{1x} B_z\right), \tag{10}$$

$$\frac{\partial \tilde{B}_{1y}}{\partial t} = \frac{\partial}{\partial z}\left(\tilde{v}_{1y} B_z\right) + \frac{\partial}{\partial x}\left(\tilde{v}_{1y} B_x\right), \tag{11}$$

$$\frac{\partial B_{1z}}{\partial t} = -k_y \tilde{v}_{1y} B_z + \frac{\partial}{\partial x}\left(v_{1z} B_x - v_{1x} B_z\right). \tag{12}$$

These equations constitute a set of coupled partial differential equations with non-constant coefficients that describe the propagation of fast and Alfvén waves. As the plasma $\beta = 0$, slow waves are excluded from the analysis. When $k_y = 0$, Equations (7)–(12) constitute two independent sets of equations. The two equations for $\tilde{v}_{1y}$ and $\tilde{B}_{1y}$ are associated with Alfvén wave propagation. On the other hand, the four equations for the remaining variables, v_{1x}, v_{1z}, B_{1x}, B_{1z}, describe the fast wave propagation. The basic normal mode properties of fast and Alfvén modes in a potential arcade with $k_y = 0$ are described in Oliver et al. (1993), while the case $k_y \neq 0$ has been considered by Arregui et al. (2004a). The time-dependent propagation for $k_y = 0$ was analyzed by Terradas et al. (2008). When longitudinal propagation of perturbations is allowed ($k_y \neq 0$), the six equations and their solutions are coupled so we may anticipate fast and Alfvén wave propagation to display a mixed nature, in an analogous way to the mixed character of eigenmodes obtained by Arregui et al. (2004a) in their analysis of the normal modes of the present equilibrium with $k_y \neq 0$. In the following, the tildes in $\tilde{v}_{1y}$ and $\tilde{B}_{1y}$ are dropped.

4. NUMERICAL METHOD AND TEST CASES

4.1. Numerical Method

The set of differential Equations (7)–(12) is too complicated to have analytical or simple numerical solutions except for simplified configurations and under particular assumptions. For this reason, we solve them by using a numerical code although comparisons with known wave properties have been carried out whenever possible.

When considering a potential arcade as the equilibrium magnetic field, it is advantageous to use field-related components instead of Cartesian components in order to characterize the directions of interest related to the polarization of each wave type. The unit vectors in the directions normal, perpendicular, and parallel to the equilibrium magnetic field are given by

$$\hat{\mathbf{e}}_n = \frac{\nabla A}{|\nabla A|}, \quad \hat{\mathbf{e}}_\perp = \hat{\mathbf{e}}_y, \quad \hat{\mathbf{e}}_\parallel = \frac{\mathbf{B}}{|\mathbf{B}|}, \tag{13}$$

where A is the flux function given in Equation (1). These unit vectors are related to the Cartesian ones as follows:

$$\hat{\mathbf{e}}_n = \frac{(B_z \hat{\mathbf{e}}_x - B_x \hat{\mathbf{e}}_z)}{|\mathbf{B}|}, \quad \hat{\mathbf{e}}_\perp = \hat{\mathbf{e}}_y, \quad \hat{\mathbf{e}}_\parallel = \frac{(B_x \hat{\mathbf{e}}_x + B_z \hat{\mathbf{e}}_z)}{|\mathbf{B}|}, \tag{14}$$

with $|\mathbf{B}| = (B_x^2 + B_z^2)^{1/2}$. In the absence of longitudinal propagation (i.e., for $k_y = 0$), these three directions are associated with the three types of waves that can be excited, namely, v_{1n} for fast waves, $v_{1\perp}$ for Alfvén waves, and $v_{1\parallel}$ for slow waves.

Since we want to model a coronal disturbance with a localized spatial distribution, we have considered as the initial condition a two-dimensional Gaussian profile given by

$$v_1 = v_s \exp\left[-\frac{(x - x_s)^2 + (z - z_s)^2}{a^2}\right], \tag{15}$$

where v_s is the amplitude of the velocity perturbation, x_s and z_s are the coordinates of the perturbation's center, and a is the width of the Gaussian profile at half height. In the following, we use $v_1 = v_{1n}$ to excite fast waves and $v_1 = v_{1y}$ to excite Alfvén waves. When $k_y = 0$, the fast mode produces plasma motions purely normal to the magnetic field, while the Alfvén mode is characterized by a purely perpendicular velocity component. When propagation along the y-direction is considered, pure fast or Alfvén modes do not exist and both produce motions in the normal velocity component as well as in the perpendicular velocity component (Arregui et al. 2004a). It must be noted that the numerical code solves the time-dependent equations in Cartesian coordinates and so the solution has to be transformed following the expressions in Equation (14) to the field-related coordinates. The same applies to the initial perturbation, which must be transformed into the corresponding Cartesian components.

The numerical code (see Bona et al. 2009, for details about the method) uses the so-called method of lines for the discretization of the variables and the time and space variables are treated separately. For the temporal part, a fourth-order Runge–Kutta method is used. For the space discretization, a finite-difference method with a fourth-order centered stencil is chosen. For a given spatial resolution, the time step is selected so as to satisfy the Courant condition. As for the boundary conditions, as we computed the time evolution of two initial perturbations, two kinds of boundary conditions are used. First, when the initial perturbation in v_{1n} is the fundamental normal mode of the $k_y = 0$ problem, for the v_{1n} component line-tying conditions are chosen at all boundaries, while for the v_{1y} component, flow-through conditions are selected except at $z = 0$ where line-tying condition is used. On the other hand, when an initial perturbation like Equation (15) is considered, the large photospheric inertia is accomplished by imposing line-tying boundary conditions at $z = 0$. In all other boundaries, flow-through conditions are used so that perturbations are free to leave the system. In order to increase numerical stability, fourth-order artificial dissipation terms are included in the numerical scheme. In all the simulations, the effects of this artificial dissipation have been checked to ensure that they do not affect the obtained solution, but just contribute to eliminate undesired high-frequency numerical modes.

4.2. Test Cases

Some preliminary tests have been performed in order to figure out the appropriate values of numerical parameters, such as the grid resolution or the numerical dissipation, on the obtained results for fast and Alfvén waves. The first test we have conducted has been to run the code with no perturbation at all and to check that the structure remains stable. The results of this numerical run were completely satisfactory. Then the propagation of linear fast and Alfvén MHD waves in a potential coronal arcade has been considered.

4.2.1. Fast Wave

The temporal evolution of impulsively generated perturbations with rather similar conditions has been accomplished by several authors: Čadež & Ballester (1995a) obtained analytical expressions for the temporal evolution of perturbations when a coronal arcade is taken as the equilibrium state; Čadež & Ballester (1995b); Oliver et al. (1998) numerically computed such solutions when different initial perturbations are used; and more recently, Terradas et al. (2008) showed the main properties of the time evolution of fast and Alfvén waves in low-β environments. These works facilitate the comparison of our numerical results with known results as well as with analytical ones.

As shown by Terradas et al. (2008), when different resolutions are used time-dependent results reveal that the grid resolution in our two-dimensional domain is not a critical factor for the proper computation of fast waves and that a good representation of the temporal evolution of perturbations can be achieved even with a rather modest resolution of 50×50 grid points in the xz-plane. As mentioned above, numerical dissipation is introduced in our code in order to ensure numerical stability. This dissipation is proportional to an adjustable parameter, or dissipation factor, σ_n. We have conducted numerical simulations for different values of the dissipation factor and it turns out that the temporal evolution of fast wave perturbations is not modified.

4.2.2. Alfvén Wave

The properties of Alfvén continuum normal modes in a potential coronal arcade described by Oliver et al. (1993) allow us to anticipate and identify possible sources of difficulties in the numerical computation of Alfvén wave solutions. First of all, since they are oscillatory solutions, strongly confined around given magnetic surfaces (both when propagating or in their standing mode version), spatial scales quickly decrease with time and so we can expect a rather important dependence of the numerical solutions on the number of grid points used to cover the area in and around the excited magnetic surfaces. The situation becomes even worse if we take into account that computations in a Cartesian grid do not allow us to locate all the grid points along magnetic surfaces. This fact affects the numerical results and adds a numerical damping. Furthermore, when time-dependent simulations are considered the sampling rate is no more an independent parameter. When the spatial resolution of the grid is defined, the Courant condition gives a maximum value for the temporal resolution which in turn sets the maximum frequency that can be resolved.

We have first generated Alfvén waves in our potential arcade model by considering an impulsive initial excitation of the v_{1y} component given by Equation (15) with $z_s = 1$ and $x_s = 0$. This implies that the initial disturbance is even about $x = 0$ and so odd Alfvén modes are not excited. As described by Terradas et al. (2008), the spatial resolution of the numerical mesh affects the obtained amplitude and frequency values. Better resolution provides a closer value to the analytical frequency and less numerical damping. We have also checked the influence of numerical dissipation and the results show that only the amplitude, and therefore the damping time, decreases when the σ_n parameter is decreased. The spectral analysis of these oscillations at different heights in the structure is shown in Figure 2(a). The resulting power spectrum is compared to the Alfvén continuum frequencies obtained by Oliver et al. (1993). The frequency associated with the generated Alfvén waves coincides with the theoretical normal mode frequencies of the system, which gives us further confidence on the goodness of our code. Alfvén waves stay confined to the vertical range of magnetic surfaces that were excited by the initial disturbance, since they cannot propagate energy across magnetic surfaces. The initial perturbation is decomposed by the system in a linear combination of normal modes, but keeping the even parity of the initial disturbance with respect to $x = 0$, so energy is only found in the fundamental mode, the second harmonic, etc.

In order to better isolate and show the possible numerical artifacts that the code introduces into the numerical solution we have considered a simpler case, the excitation of a particular Alfvén mode around a magnetic surface. According to Oliver et al. (1993), Alfvén normal mode solutions can be obtained analytically when $\delta = 0$. For this reason, we now select $\delta = 0$.

The initial excitation could now be given by

$$v_{1y}(x, z) = \hat{v}_{1y}(x)\delta[A(x, z) - A(x = 0, z_m)], \qquad (16)$$

where $\hat{v}_{1y}$ is the regular part of the solution, $A(x,z)$ is the flux function defined by Equation (1), and z_m gives the maximum height of the magnetic field line in which the normal mode is excited. It is important to note that the regular solution has a well-defined parity with respect to the x-direction depending on whether n is chosen even or odd. However, since a delta function is difficult to handle from a numerical point of view, our normal-mode-like excitation is performed by an initial perturbation of the form

$$v_{1y}(x, z) = \hat{v}_{1y}(x) \exp\left[-\frac{A(x, z) - A(x = 0, z_m)}{a^2}\right]. \qquad (17)$$

For the regular part, $\hat{v}_{1y}(x)$, the fundamental mode with one maximum along the field lines has been chosen. It should be noted that the width, a, of the initial perturbation now causes the excitation of several Alfvén modes in a set of neighboring magnetic surfaces. It is important to consider an initial velocity profile which is sufficiently localized in the direction transverse to magnetic surfaces so that only a few of them are excited. As we concentrate on the dynamics of a restricted number of field lines around a magnetic surface, the consideration of other models, with different values of δ, would change quantitatively the generated frequencies, but not the overall qualitative conclusions shown here.

Figure 2(b) shows the temporal evolution of the excited v_{1y} component at a particular location as a function of time for three different values for the width of the initial disturbance. It is clear that three different solutions are obtained. The two corresponding to the largest widths are rather similar, but the one for the smaller width shows a strong damping. It must be said that the exact solution of this ideal system should display no time damping, hence we assert that this is a numerical effect that cannot be attributed to a real physical damping mechanism. This undesired effect is less important for larger widths of the initial perturbation since, for a given number of grid points, the initial condition is better resolved spatially.

We next fix the width of the initial disturbance, a, and vary the spatial resolution in our domain. Figure 3 shows several numerical simulations when an initial normal-mode-like excitation (Equation (17)) is made at different heights. It is clear that larger spatial resolution provides more accurately the undamped oscillatory solution.

Also from this analysis, we conclude that the spatial resolution is not a factor that should be taken into account in an isolated manner when considering the numerical description of Alfvén

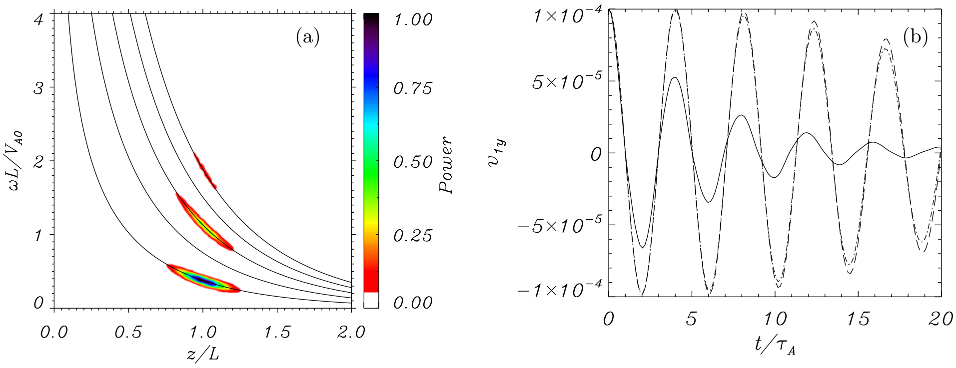

Figure 2. (a) Shaded contours are the power spectrum of v_{1y} at $x = 0$ as a function of height, z/L, and normalized frequency, $\omega L/v_{A0}$. In this simulation, the spatial grid is set to 600 × 600 while the numerical dissipation is fixed to $\sigma_n = 0.001$. Solid lines are the theoretical frequency of the normal Alfvén modes for $\delta = 0$, given by Oliver et al. (1993). From bottom to top, they represent the fundamental mode and its harmonics. (b) Temporal evolution of the v_{1y} component when the initial perturbation is an Alfvén normal mode of the system located at $x = 0$ and $z_m/L = 0.33$ (see Equation (17)). Here, $\delta = 0$, the numerical grid has 400 × 400 points, and $\sigma_n = 0.001$. Different solutions correspond to $a/L = 0.01$ (solid), $a/L = 0.1$ (dash-dotted), and $a/L = 0.2$ (long dashed). Time is given in units of $\tau_A = L/v_{A0}$. (A color version of this figure is available in the online journal.)

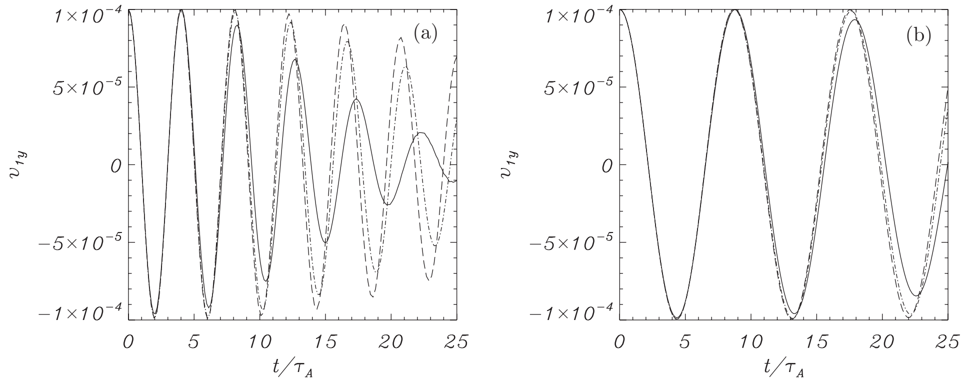

Figure 3. (a) Temporal evolution of the v_{1y} velocity component at $x = 0$ and $z_m/L = 0.33$ for an initial perturbation given by Equation (17) with $a/L = 0.2$ and $\sigma_n = 0.001$. (b) Temporal evolution of the v_{1y} velocity component at $x = 0$ and $z_m/L = 0.66$ for an initial perturbation with $a/L = 0.2$ and $\sigma_n = 0.001$. In both panels, solid, dash-dotted, and long dashed lines represent a resolution of 200 × 200, 400 × 400, and 600 × 600 points, respectively.

waves on given magnetic surfaces. Indeed, and because of the Cartesian distribution of grid points in a system of curved magnetic field lines, low-lying magnetic lines are poorly resolved when compared to high-lying magnetic lines for a given grid resolution. This has implications that are worth to be taken into account as can be seen in Figure 3. If we compare signals in Figure 3, we can see that all parameters being the same, closer results to the analytical solution are obtained for higher magnetic field lines. We can therefore assert that for the numerical simulation of Alfvén wave properties, the resolution of the grid is an important parameter and that it becomes more critical for low-lying magnetic field lines than for higher ones. It should be noted that the conclusions of these tests can also be applied to the case in which an impulsive excitation is set as the initial perturbation.

5. NUMERICAL RESULTS

In this section, we present the main results from our numerical investigation. For simplicity, first, the temporal evolution of a normal-mode-like fast disturbance is analyzed in order to show how and where resonant absorption, due to three-dimensional propagation of perturbations in a non-uniform medium, takes place. It turns out that previous results obtained for the normal modes of coupled fast and Alfvén waves in a potential arcade by Arregui et al. (2004a) can guide us to understand the time evolution of the system and the energy transfer between resonantly coupled modes. Then, a more complex situation is considered by analyzing the time evolution of the initial perturbation given by Equation (15). It should be noted that our first normal mode time evolution analysis has been proved very useful to further better understand the resulting coupling process between both velocity components when a localized impulsive disturbance is used.

5.1. Resonant Damping of Fast MHD Normal Modes in a Potential Arcade

In order to gain some insight into the propagation properties of coupled fast and Alfvén waves in our configuration, we first study the time evolution caused by an initial disturbance having the spatial structure of a fast normal mode for $k_y = 0$ (propagation in the xz-plane). As shown by Oliver et al. (1993), pure fast modes in a potential arcade are characterized by a global spatial structure determined by the wavenumbers k_x and k_z, which give rise to smooth distributions with a given number of maxima in the x- and z-directions. This results in a discrete spectrum of frequencies. The frequencies and spatial structure of the fast modes with $k_y \neq 0$ were computed by Arregui et al. (2004a), who showed that perpendicular propagation produces the coupling of the fast normal modes to Alfvén continuum solutions, resulting in modes with mixed properties. We have chosen as initial perturbation the velocity perturbation v_{1n} of the fundamental fast mode for $k_y = 0$, with one maximum in each

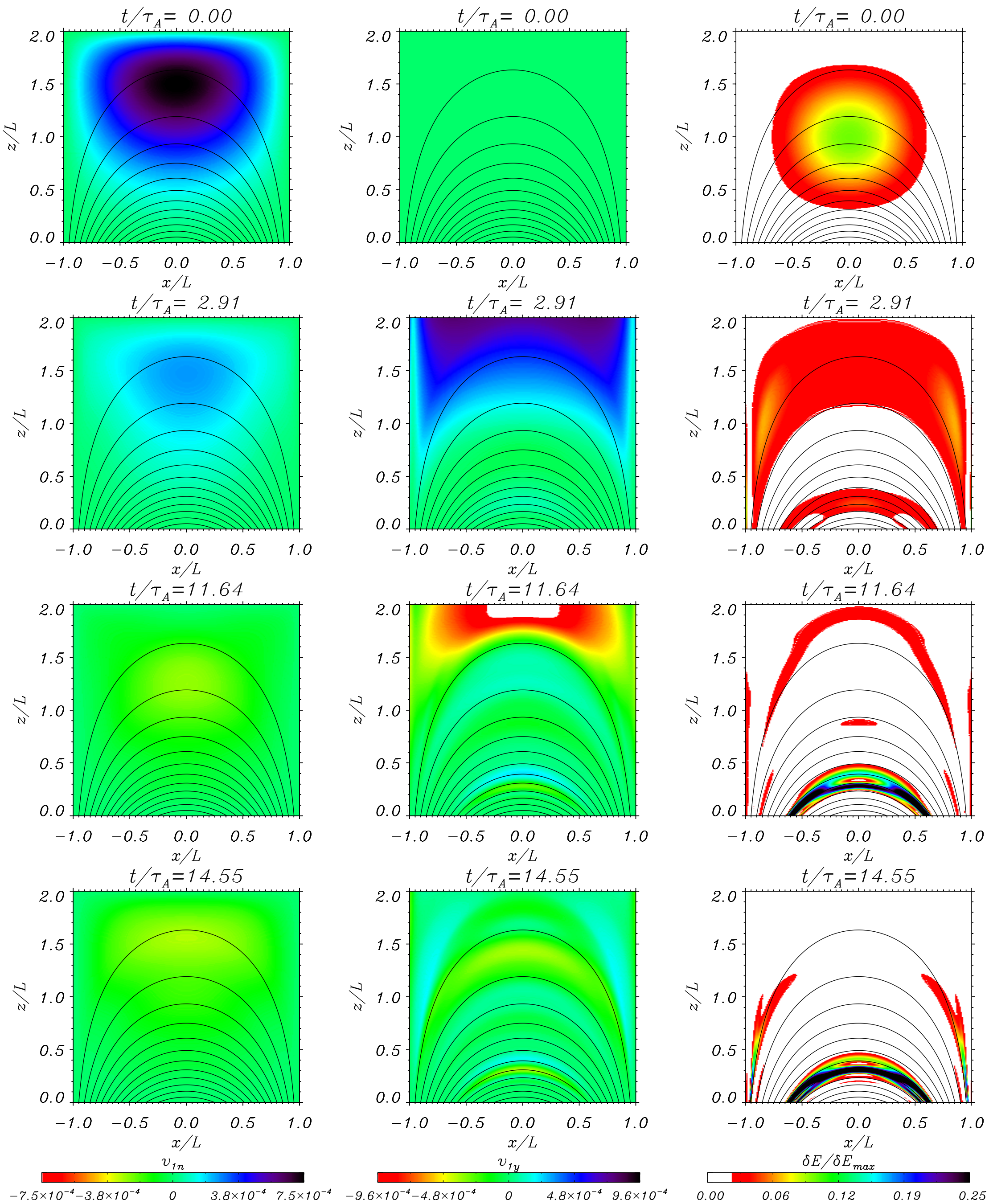

Figure 4. Several snapshots of the two velocity components, v_{1n} and v_{1y}, and of the total energy density in a potential arcade with $\delta = 2$ and for $k_y L = 1$. The initial perturbation in v_{1n} is the fundamental normal mode of the $k_y = 0$ problem. For this simulation, a 600×600 grid is used. Magnetic field lines are represented with white (left and middle panels) and black lines (right panels). A movie displaying the full time evolution is available in the electronic version of the journal.

(An animation and a color version of this figure are available in the online journal.)

direction in the xz-plane. When $k_y = 0$, this produces a standing harmonic oscillation of the system, as in an elastic membrane. When $k_y \neq 0$, this initial perturbation is not a normal mode of the system, but we expect that the obtained temporal evolution will not differ very much from the actual normal mode of the coupled solution.

Figure 4 displays the results of such simulation. The first frame for v_{1n} shows the initial spatial distribution of the perturbation. Initially, v_{1y}, the velocity component associated with Alfvén waves, is zero. As time evolves, a non-zero v_{1y} component appears because of the coupling introduced by the three-dimensional propagation. The panels for v_{1y} in Figure 4 show that unlike v_{1n} the excited transversal perturbations are not globally distributed in the potential arcade, but only at preferred locations, around a few magnetic surfaces. When the v_{1n} and v_{1y} signals are measured at one of those locations, $x = 0$, $z/L = 0.35$, it is seen that the amplitude related to the fast-like perturbation decreases in time, while the amplitude of the Alfvén-like component of the perturbation increases in time, see Figure 5. This is an indication of the wave energy transfer due

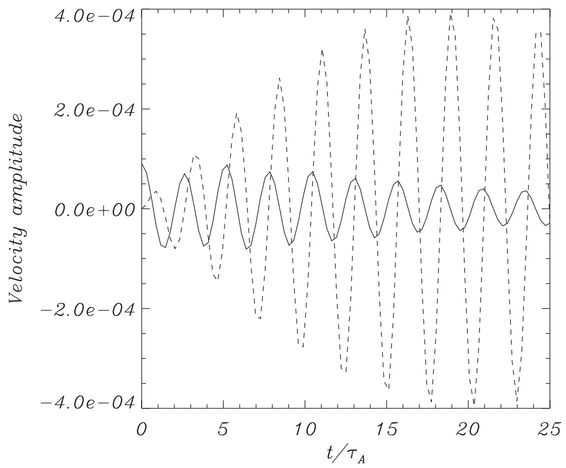

Figure 5. Temporal evolution of the normal, v_{1n} (solid line), and perpendicular, v_{1y} (dashed line), velocity components at $x = 0$, $z/L = 0.35$. Data taken from the simulation shown in Figure 4.

to the resonant coupling of the excited fast normal mode to the Alfvénic solution around the excited magnetic surface. For long times, a decrease in the amplitude of the velocity component, v_{1y}, can be appreciated and is attributed to numerical damping, for the reasons explained in Section 4.2.2.

Further confirmation of the resonant wave energy transfer occurring between the modes can be obtained by computing the time evolution of the total energy density in our system. This total wave energy can be computed as

$$\delta E(\mathbf{r}, t) = \frac{1}{2}\left[\rho_0\left(v_{1x}^2 + v_{1y}^2 + v_{1z}^2\right) + \frac{1}{\mu_0}\left(B_{1x}^2 + B_{1y}^2 + B_{1z}^2\right)\right]. \tag{18}$$

The right-hand side panels in Figure 4 show the spatial distribution of this quantity as a function of time. The different frames clearly indicate that, initially, the energy is distributed globally around the center of the system, which corresponds to the initial perturbation we have used. At later times, this energy is transferred to magnetic surfaces around the particular magnetic field line in the arcade where the signals in Figure 5 have been measured. The location of this energy deposition is not an arbitrary one. As previous theoretical works on the resonant energy transfer have shown (e.g., Wright 1992; Halberstadt & Goedbloed 1993; Ruderman et al. 1997; Arregui et al. 2004a; Russell & Wright 2010), global fast modes resonantly couple to localized Alfvén continuum modes at the magnetic surfaces where the frequency of the fast mode matches that of the corresponding Alfvén mode. In our case, the spectral analysis of the wave energy densities associated with the normal and perpendicular components, plotted in Figure 6, allow us to confirm the resonant energy transfer at the location where the fundamental fast mode frequency crosses the Alfvén continuum, that exactly corresponds to the magnetic surface where Alfvénic oscillations are excited and energy transfer occurs, see Figure 6(b). Although the fast mode frequency crosses other Alfvén continua, coupling can only occur if the parity of the fast and Alfvén eigenfunctions along the field lines is the same, see further details in Arregui et al. (2004a). This prevents the coupling with Alfvén continuum modes with two extrema along field lines. Even if the coupling with Alfvén modes with three extrema along field lines is allowed, we find no signatures of this resonant coupling in the power spectrum analysis nor the wave energy density evolution.

5.2. *Propagation of Coupled Fast and Alfvén Disturbances in a Potential Coronal Arcade*

Oscillations in coronal magnetic structures are believed to be generated by nearby disturbances, such as flares or filament eruptions. It is clear that such disturbances are far from being a normal mode of a particular structure as our potential arcade. Therefore, we have next considered the impulsive excitation of perturbations by means of a localized disturbance, which is expected to be a better representation of the real phenomena that often trigger waves and oscillations in the solar corona. In particular, a Gaussian velocity perturbation is considered and the response of the system is expected to be different from the one described in Section 5.1, since now the initial perturbation is likely to be decomposed in a linear combination of normal modes with different frequencies that will constitute the resulting propagating wave.

We have produced an impulsive excitation of the v_{1n} velocity component of the form given by Equation (15) and have considered $k_y \neq 0$. Time evolution of the velocity components and the total energy density are displayed in Figure 7, which shows that the generated wave has both normal and perpendicular velocity components. Note that $v_{1y} = 0$ in the absence of k_y (see Terradas et al. 2008). It is clear in Figure 7 that the perturbed

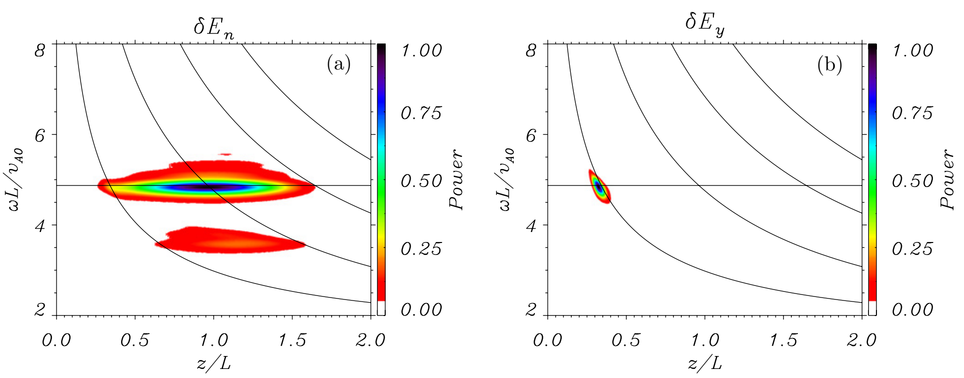

Figure 6. Shaded contours represent the power spectrum of (a) δE_n and (b) δE_y as a function height, z/L, at the symmetry plane $x = 0$, for the simulation shown in Figure 4. Note that because of the quadratic nature of the wave energy density, the curved lines have double the frequency of the Alfvén continua given by Oliver et al. (1993) and the horizontal lines have double the frequency of the fast normal mode.

(A color version of this figure is available in the online journal.)

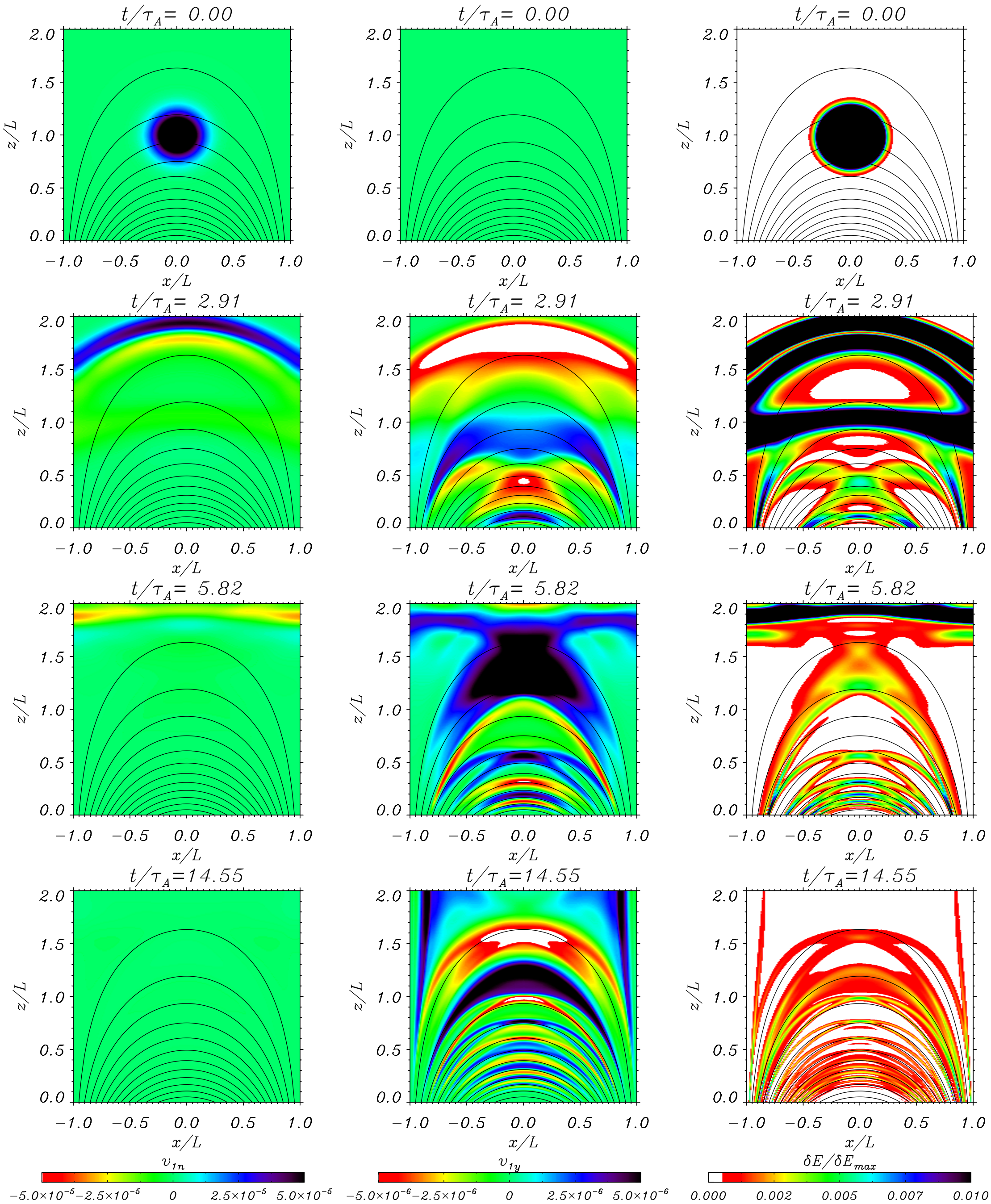

Figure 7. Time evolution of the v_{1n} (left panels), v_{1y} (middle panels) velocity components, and of the total energy density (right panels) in a potential arcade with $\delta = 1$. The initial perturbation is imposed on the v_{1n} component with $x_s = 0$, $z_s = 1$, $v_s = 10^{-4} v_{A0}$, $a = 0.2L$ (see Equation (15)), and $k_y L = 1$. For this simulation, a 600×600 grid is used. Magnetic field lines are represented with white (left and middle panels) and black lines (right panels). A movie displaying the full time evolution is available in the electronic version of the journal.

(An animation and a color version of this figure are available in the online journal.)

normal velocity component evolution is similar to the one presented by Terradas et al. (2008) for the decreasing Alfvén speed model with constant density and $k_y = 0$. For the normal velocity component, the shape of the wavefront is not circular, due to the fact that perturbations propagate faster toward the photosphere. For large times, the front tends to be planar as the initial curvature of the wave packet is lost. As for the perpendicular velocity perturbation that is excited because of the three-dimensional character of the wave, its spatial distribution is highly anisotropic, with the signal concentrated around many magnetic surfaces. A wavefront with fast-like properties, similar to the one present in v_{1n}, can also be seen to propagate upwards producing v_{1y} perturbations until it leaves the system. At the end, a collection of Alfvénic oscillations are generated in the arcade. By comparing with the results presented in the previous section, we can think about them as being generated by the resonant coupling between the fast-like wavefront and several Alfvén continuum solutions, instead of the single resonance case

No. 1, 2010 THREE-DIMENSIONAL PROPAGATION OF MAGNETOHYDRODYNAMIC WAVES 659

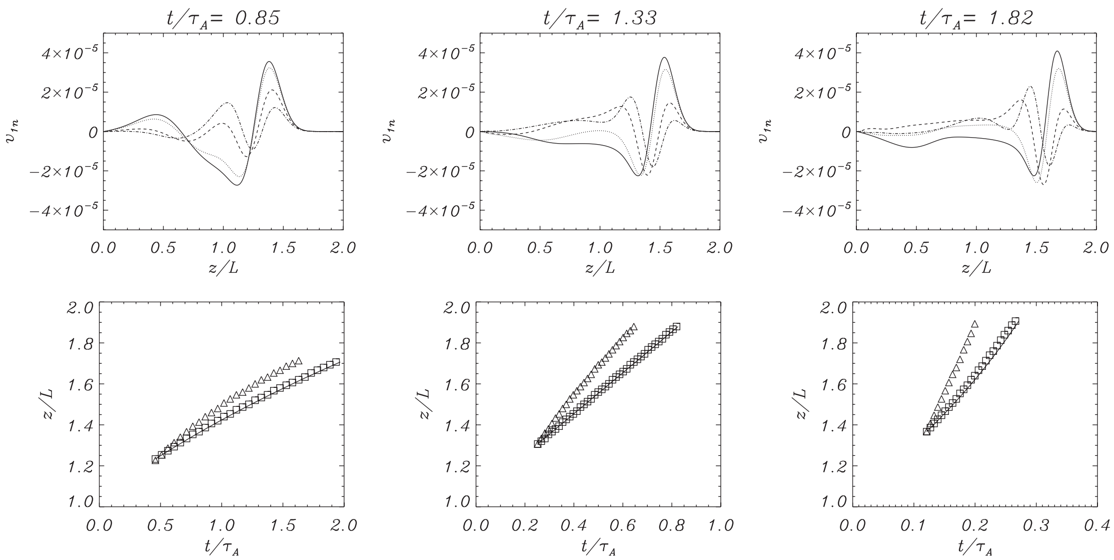

Figure 8. Top panels: several snapshots of the spatial distribution of the normal velocity component along $x = 0$. The values of the longitudinal wavenumber are $k_y = 0$ (solid line), $k_y L = 3$ (dotted), $k_y L = 7$ (dashed), and $k_y L = 10$ (dash-dotted). Bottom panels: position of the wavefront as a function of time when different values of the delta parameter, $\delta = 1$ (left), $\delta = 2$ (middle), and $\delta = 3$ (right), and longitudinal wavenumber, $k_y = 0$ (squares) and $k_y L = 10$ (triangles), are selected. The solid line shows the analytical solution for the wavefront position when longitudinal propagation is not allowed ($k_y = 0$), see Equation (19).

shown in Section 5.1. Once excited, magnetic surfaces remain oscillating with their natural period and for large times they are phase-mixed because of the transverse non-uniformity.

We have next analyzed in a quantitative way the effect of k_y on the properties of the generated fast-like wavefront and the induced Alfvénic oscillations. Regarding the fast-like wavefront, Figure 8 (top panels) shows different snapshots of the cut along $x = 0$ of the v_{1n} component for different values of k_y. These figures indicate that the larger the value of k_y, the faster the wavefront propagates. The propagation velocity can be measured by plotting the position of the wavefront maximum as a function of time (see Figure 8, bottom left). The time evolution of the wavefront is followed for $t \geqslant t_0$ and the initial position of the maximum is denoted by z_0. For this relatively simple case, the numerical results can be compared with the analytical formula obtained by the integration of the local Alfvén speed profile (see Equation (5) in Oliver et al. 1998). The resulting expression is

$$z(t) = \frac{2\Lambda_B}{2-\delta} \log\left[\pm v_{A0}\frac{2-\delta}{2\Lambda_B}(t-t_0) + \exp\left(\frac{2-\delta}{2\Lambda_B} z_0\right)\right], \tag{19}$$

where the + and − signs correspond to upward and downward propagation, respectively. Figure 8 (bottom panels) shows a perfect correspondence between the numerically measured speed and the analytical expression when different models of the solar atmosphere are considered. The increase of the travel speed of fast-like wavefronts when $k_y \neq 0$ is an important property to be taken into account in the three-dimensional problem.

For the Alfvénic oscillations, the power spectrum is analyzed in a cut along $x = 0$, which allows us to study the power on different magnetic surfaces. Figure 9 shows power at a large number of magnetic surfaces, not just around a selected group of field lines around a given magnetic surface, so a wide range of magnetic surfaces are excited because of the coupling. Also, not just the fundamental mode is excited, but also several higher harmonics. All of them have even parity with respect to $x = 0$, which corresponds to the parity of the v_{1n} perturbation and the

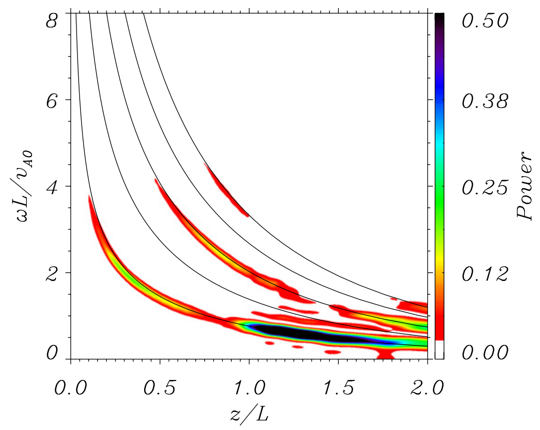

Figure 9. Shaded contours represent the normalized power spectrum of the v_{1y} velocity component corresponding to the simulation shown in Figure 7 as a function of the maximum height of field lines, z/L, and normalized frequency, $\omega L/v_{A0}$. Solid lines are the theoretical frequency of the Alfvén normal mode obtained by Oliver et al. (1993). The frequency analysis is made at the symmetry plane, $x = 0$.

(A color version of this figure is available in the online journal.)

parity rule for $k_y \neq 0$ (Arregui et al. 2004a). When comparing the power spectrum obtained from the numerical solution with the analytical Alfvén continuum frequencies given by Oliver et al. (1993) for the case $k_y = 0$, we see that the signal coincides with the analytical curves for $k_y = 0$. As expected, perpendicular propagation has no effect on the frequencies of Alfvén waves generated on different magnetic surfaces in the arcade. This is a known result since $\omega \sim (\mathbf{k} \cdot \mathbf{B})$.

As with the normal mode case, a quantitative analysis of the time evolution of the wave energy of the system helps to better understand the process of energy conversion between fast and Alfvén waves. Figure 7 (right-hand side panels) shows the evolution of the total energy density as a function of time. At early stages, this quantity shows a clear signature of a fast-like wavefront propagating through the domain. For long times, the energy deposition is spatially distributed on the whole system,

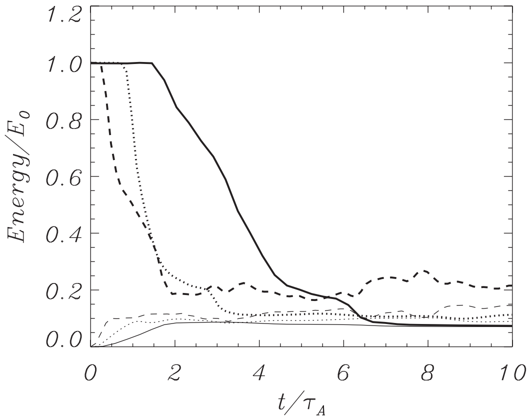

Figure 10. Solid ($\delta = 1$), dotted ($\delta = 2$), and dashed ($\delta = 3$) lines are the normalized total energy (thick lines) and the normalized total energy associated with the y-direction (thin lines) as a function of time for $k_y L = 1$.

not only on a single magnetic surface, as in the previous section. Although a large part of the energy leaves the system in the form of fast-like wavefronts, part of the energy remains trapped in the Alfvénic oscillations that are resonantly excited in the arcade. The amount of energy trapped in the system can be calculated by the integration of the total energy density (see Equation (18)) in the whole domain as a function of time. The result is shown in Figure 10 (solid line). For short times the total energy remains almost constant, but when the fast front reaches the boundaries of the system a strong decrease of this quantity is seen. Resonant wave conversion very quickly produces velocity perturbations in the y-direction and the energy associated with these Alfvénic components grows up to its maximum value before the fast wavefront leaves the system. At later stages, a fraction of around 5%–10% of the initial total energy is retained in the system and the total energy remains almost constant in the subsequent time evolution. We must note that this energy is trapped even in the absence of any density enhancement or wave cavity.

So far, we have used fixed values for the perpendicular propagation wavenumber, k_y, and the ratio of magnetic to density scale heights, δ. We have next analyzed the influence of these parameters on the obtained results concerning the energy transfer between fast and Alfvén waves. Figure 11 shows the total energy time evolution for different values of k_y. Several conclusions can be extracted. First, the amount of energy that is trapped by the system in the form of Alfvénic oscillations increases with k_y and is above 40% for the largest value of this parameter that we have considered. This can be understood in terms of stronger resonant coupling occurring for larger values of k_y. The relation between the total energy and the energy associated with the y-direction also changes with k_y, in such a way that, while for relatively small k_y almost all the energy of the system is stored in oscillations in the y-direction, for larger values of k_y there is a difference between the total energy and the Alfvénic energy for large times. To understand this, we need to mention that for $k_y \neq 0$ Alfvén waves have both perpendicular and normal velocity components and so Alfvén wave energy is not only contained in the y-direction. Although this effect is less visible in the simulations it can be measured, as shown in Figure 11. Note also that for large times the two energy densities decay. This is due to numerical damping, since when very small

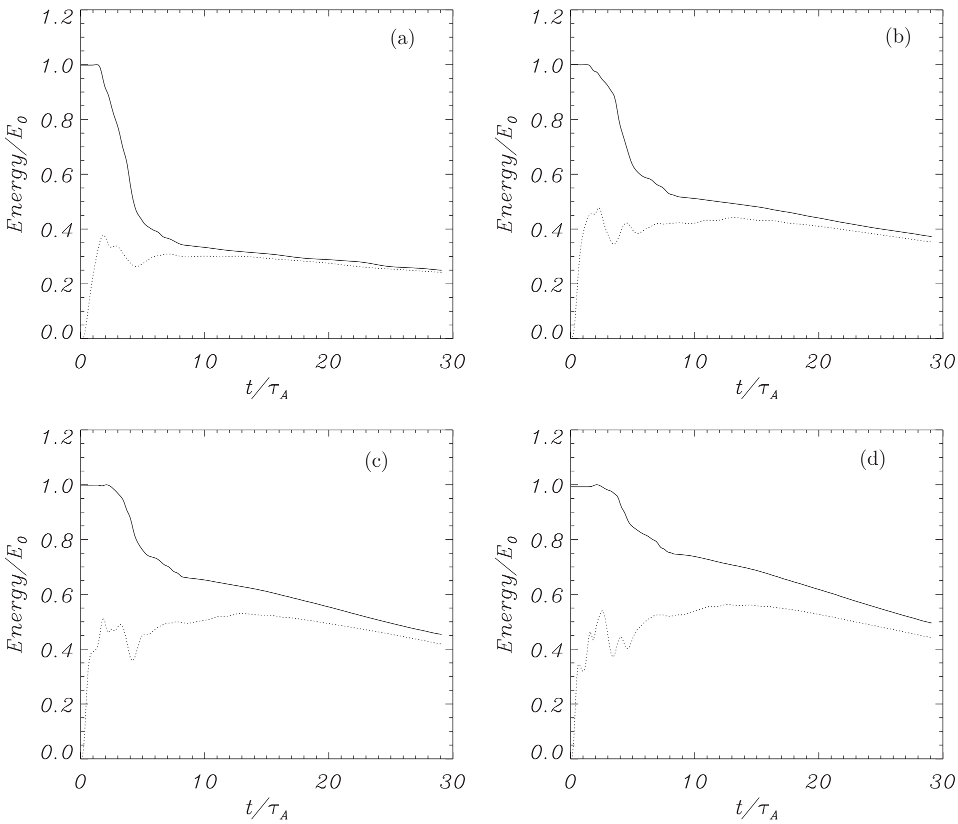

Figure 11. Normalized total energy of the system as a function of time (solid line) and normalized energy associated with the y-direction (dotted line) for $\delta = 1$ and different values of the longitudinal wavenumber: (a) $k_y L = 3$, (b) $k_y L = 5$, (c) $k_y L = 7$, and (d) $k_y L = 9$.

scales are created the spatial resolution used is not fine enough to handle the localized Alfvénic oscillations that are phase-mixed for large times (see Section 4.2.2).

As for the δ parameter, it controls our model atmosphere, since it allows us to select different ratios of the magnetic scale height to the density scale height. By repeating the previous numerical experiments for two additional values of this parameter, the following results are obtained (see Figure 8, bottom panels). Depending on the value of δ, the Alfvén speed profile in the vertical direction has a steeper or flatter profile. This means that the time that a fast-like perturbation needs to reach the boundaries of the system and leave, it varies with δ. Therefore, the time at which the sudden decrease of the total energy of the system occurs differs for different values of δ, see Figure 10. However, the fractional amount of wave energy that is transferred to Alfvén waves and is trapped in the system does not depend on the model atmosphere we use. Nevertheless, the rate at which the energy transfer occurs does depend on the model atmosphere that can be appreciated from the different slopes of the energy in Figure 10.

6. CONCLUSIONS

In this paper, we have studied the temporal evolution of coupled fast and Alfvén waves in a potential coronal arcade when three-dimensional propagation is allowed. Because of the inclusion of three-dimensional dependence on the perturbed quantities, fast and Alfvén waves are coupled and the resulting solutions display a mixed fast/Alfvén character. The non-uniform nature of the considered medium produces the coupling to be of resonant nature, in such a way that transfer of energy and wave damping occur in the system.

First, the nature of resonant coupling between a fast normal mode of the system and Alfvén continuum modes has been analyzed. It is seen that the fast mode with a global nature resonantly couples to localized Alfvén waves around a given magnetic surface in the arcade, thus transferring its energy to the latter. The position of the resonant surface perfectly agrees with the resonant frequency condition predicted by several authors in previous studies of this kind, and with the parity rules given by Arregui et al. (2004a).

Next, the temporal evolution of a localized impulsive disturbance has been analyzed. The inclusion of perpendicular propagation produces an increase in the wave propagation speed for the fast-like wavefront when compared to the purely poloidal propagation case. As in the previous case, perpendicular propagation induces the excitation of Alfvénic oscillations around magnetic surfaces, due to the resonant coupling between fast and Alfvén waves. Now these oscillations cover almost the whole domain in the arcade, so that the energy of the initial perturbation is spread into localized Alfvénic waves. The frequency of the induced Alfvénic oscillations is seen to be independent from the perpendicular wavenumber. As time progresses and the initial wavefront leaves the system, part of the energy is stored in these Alfvén waves which remain confined around magnetic surfaces. Phase mixing then gives rise to smaller and smaller spatial scales, until the numerical code is unable to properly follow the subsequent time evolution. The energy trapping around magnetic surfaces occurs even in the absence of a density enhancement or a wave cavity structure, and is only due to the non-uniformity of the density profile and the magnetic structuring, which lead to a non-uniform Alfvén speed distribution.

Finally, the efficiency of this wave energy transfer between large-scale disturbances and small-scale oscillations has been studied as a function of the perpendicular wavenumber and for different values of the ratio of the magnetic scale height to the density scale height. It is seen that the first factor strongly affects the amount of energy trapped by Alfvén waves. The amount of energy trapped by the arcade increases for increasing value of the perpendicular wavenumber. The particular ratio of magnetic to density scale heights determines how fast the available fast wave energy leaves the system and, therefore, the rate at which energy can be transferred to Alfvén waves, but not the final amount of energy stored by the arcade in the form of Alfvénic oscillations.

The authors acknowledge the Spanish MCyT for the funding provided under project AYA2006-07637 and D. Fanning (http://www.dfanning.com/) for his helpful advices about IDL. S.R. also acknowledges MCyT for a fellowship.

REFERENCES

Arregui, I., Oliver, R., & Ballester, J. L. 2004a, A&A, 425, 729
Arregui, I., Oliver, R., & Ballester, J. L. 2004b, ApJ, 602, 1006
Aschwanden, M. J., de Pontieu, B., Schrijver, C. J., & Title, A. M. 2002, Sol. Phys., 206, 99
Aschwanden, M. J., Fletcher, L., Schrijver, C. J., & Alexander, D. 1999, ApJ, 520, 880
Banerjee, D., Erdélyi, R., Oliver, R., & O'Shea, E. 2007, Sol. Phys., 246, 3
Bona, C., Bona-Casas, C., & Terradas, J. 2009, J. Comput. Phys., 228, 2266
Brady, C. S., & Arber, T. D. 2005, A&A, 438, 733
Brady, C. S., Verwichte, E., & Arber, T. D. 2006, A&A, 449, 389
Čadež, V. M., & Ballester, J. L. 1995a, A&A, 296, 537
Čadež, V. M., & Ballester, J. L. 1995b, A&A, 296, 550
Del Zanna, L., Schaekens, E., & Velli, M. 2005, A&A, 431, 1095
Díaz, A. J., Zaqarashvili, T., & Roberts, B. 2006, A&A, 455, 709
Edwin, P. M., & Roberts, B. 1983, Sol. Phys., 88, 179
Goossens, M., Poedts, S., & Hermans, D. 1985, Sol. Phys., 102, 51
Halberstadt, G., & Goedbloed, J. P. 1993, A&A, 280, 647
Murawski, K., Selwa, M., & Nocera, L. 2005, A&A, 437, 687
Nakariakov, V. M., & Ofman, L. 2001, A&A, 372, L53
Nakariakov, V. M., Ofman, L., Deluca, E. E., Roberts, B., & Davila, J. M. 1999, Science, 285, 862
Oliver, R., Ballester, J. L., Hood, A. W., & Priest, E. R. 1993, A&A, 273, 647
Oliver, R., Hood, A. W., & Priest, E. R. 1996, ApJ, 461, 424
Oliver, R., Murawski, K., & Ballester, J. L. 1998, A&A, 330, 726
Poedts, S., & Goossens, M. 1988, A&A, 198, 331
Poedts, S., Hermans, D., & Goossens, M. 1985, A&A, 151, 16
Roberts, B., Edwin, P. M., & Benz, A. O. 1984, ApJ, 279, 857
Ruderman, M. S., Goossens, M., Ballester, J. L., & Oliver, R. 1997, A&A, 328, 361
Russell, A. J. B., & Wright, A. N. 2010, A&A, 511, A17
Schrijver, C. J., Aschwanden, M. J., & Title, A. M. 2002, Sol. Phys., 206, 69
Selwa, M., Murawski, K., Solanki, S. K., & Wang, T. J. 2007, A&A, 462, 1127
Selwa, M., Solanki, S. K., Murawski, K., Wang, T. J., & Shumlak, U. 2006, A&A, 454, 653
Terradas, J. 2009, Space Sci. Rev., 149, 255
Terradas, J., Oliver, R., & Ballester, J. L. 1999, ApJ, 517, 488
Terradas, J., Oliver, R., & Ballester, J. L. 2006, ApJ, 650, L91
Terradas, J., Oliver, R., Ballester, J. L., & Keppens, R. 2008, ApJ, 675, 875
Tsubaki, T. 1988, in Solar and Stellar Coronal Structures and Dynamics, ed. R. C. Altrock (Sunspot, NM: National Solar Observatory), 140
Van Doorsselaere, T., Debosscher, A., Andries, J., & Poedts, S. 2004, A&A, 424, 1065
Van Doorsselaere, T. V., Verwichte, E., & Terradas, J. 2009, Space Sci. Rev., 149, 299
Verwichte, E., Foullon, C., & Nakariakov, V. M. 2006a, A&A, 446, 1139
Verwichte, E., Foullon, C., & Nakariakov, V. M. 2006b, A&A, 449, 769
Verwichte, E., Foullon, C., & Nakariakov, V. M. 2006c, A&A, 452, 615
Verwichte, E., Nakariakov, V. M., Ofman, L., & Deluca, E. E. 2004, Sol. Phys., 223, 77
Wright, A. N. 1992, J. Geophys. Res., 97, 6429

Chapter 3

Wave Leakage and Resonant Absorption in a Loop Embedded in a Coronal Arcade. (Rial et al. (2013)).

The Astrophysical Journal, 763:16 (11pp), 2013 January 20 doi:10.1088/0004-637X/763/1/16

WAVE LEAKAGE AND RESONANT ABSORPTION IN A LOOP EMBEDDED IN A CORONAL ARCADE

S. Rial[1], I. Arregui[2], J. Terradas[1], R. Oliver[1], and J. L. Ballester[1]
[1] Departament de Física, Universitat de les Illes Balears, E-07122, Palma de Mallorca, Spain; samuel.rial@uib.es, jaume.terradas@uib.es, ramon.oliver@uib.es, joseluis.ballester@uib.es
[2] Instituto de Astrofísica de Canarias, E-38205 La Laguna, Tenerife, Spain; iarregui@iac.es
Received 2012 January 19; accepted 2012 September 30; published 2012 December 28

ABSTRACT

We investigate the temporal evolution of impulsively generated perturbations in a potential coronal arcade with an embedded loop. For the initial configuration we consider a coronal loop, represented by a density enhancement, which is unbounded in the ignorable direction of the arcade. The linearized time-dependent magnetohydrodynamic equations have been numerically solved in field-aligned coordinates and the time evolution of the initial perturbations has been studied in the zero-β approximation. For propagation constrained to the plane of the arcade, the considered initial perturbations do not excite trapped modes of the system. This weakness of the model is overcome by the inclusion of wave propagation in the ignorable direction. Perpendicular propagation produces two main results. First, damping by wave leakage is less efficient because the loop is able to act as a better wave trap of vertical oscillations. Second, the consideration of an inhomogeneous corona enables the resonant damping of vertical oscillations and the energy transfer from the interior of the loop to the external coronal medium.

Key words: Sun: atmosphere – Sun: corona – Sun: oscillations – Sun: surface magnetism

Online-only material: animations, color figures

1. INTRODUCTION

A phenomenon that has attracted the attention of solar physicists in the last years is the discovery of transverse oscillations of coronal loops observed in EUV wavelengths (171 Å) with the *Transition Region and Coronal Explorer* in 1998. The oscillatory amplitude and period are of the order of a few Mm and a few minutes, respectively, and one of the most interesting features of these oscillations is that their amplitude decreases quickly with time, typically in a few periods. Some examples of this oscillatory phenomenon, namely flare-excited transversal oscillations, were reported by Aschwanden et al. (1999), Nakariakov et al. (1999), and more recently by Wang & Solanki (2004), Hori et al. (2005), Verwichte et al. (2009, 2010), Aschwanden & Schrijver (2011), White & Verwichte (2012), and Wang et al. (2012). Extensive overviews of this phenomenon can be found in Aschwanden et al. (2002, 2009) and Schrijver et al. (2002).

The first theoretical studies of the oscillatory modes of coronal flux tubes modeled as straight magnetic cylinders were done by Wentzel (1979), Spruit (1981), Edwin & Roberts (1983), and Roberts et al. (1984). Later, flare-generated transverse oscillations were interpreted as fast kink eigenmode oscillations of straight cylindrical tubes (Nakariakov & Ofman 2001; Ruderman & Roberts 2002; Goossens et al. 2002). In the context of curved coronal magnetic structures, Goossens et al. (1985), Poedts et al. (1985), and Poedts & Goossens (1988) investigated the continuous spectrum of ideal magnetohydrodynamics (MHD). Oliver et al. (1993, 1996) and Terradas et al. (1999) derived the spectrum of modes in potential and non-potential arcades. More complex configurations, such as sheared magnetic arcades in the zero plasma-β limit, have been studied by Arregui et al. (2004a, 2004b). Other authors have studied eigenmodes in curved configurations with density enhancements that represent coronal loops (e.g., Smith et al. 1997; Van Doorsselaere et al. 2004; Terradas et al. 2006b; Verwichte et al. 2006a, 2006b, 2006c; Díaz et al. 2006; Van Doorsselaere et al. 2009). The fact that the corona is a highly inhomogeneous and structured medium complicates the theoretical description of MHD waves and it is believed that this could be the underlying cause of the observed wave damping. Several mechanisms of wave damping have been proposed, the most popular being phase mixing (Heyvaerts & Priest 1983), resonant absorption (Hollweg & Yang 1988; Goossens 1991; Goossens et al. 2002; Ruderman & Roberts 2002; Van Doorsselaere et al. 2004, and references therein), and more recently wave leakage by tunneling (Brady & Arber 2005; Brady et al. 2006; Verwichte et al. 2006a, 2006b, 2006c; Díaz et al. 2006).

Although normal modes should be seen as the building blocks for the interpretation of coronal loop oscillations they do not represent the whole picture, but their study provides a basis for understanding the dynamics of the system. To have a more complete description, the time-dependent problem needs to be analyzed. Using this method, Čadež & Ballester (1995a, 1995b) studied analytically the propagation of fast waves in a two-dimensional coronal arcade with uniform Alfvén speed. Oliver et al. (1998) studied the effect of impulsively generated fast waves in the same coronal structure. Del Zanna et al. (2005) studied the properties of Alfvén waves in an arcade configuration, including a transition region between the photosphere and the corona. Terradas et al. (2008b) used a potential arcade embedded in a low β environment to study the properties of linear waves. Other studies have analyzed the effect of the loop structure on the properties of fast and slow waves in two-dimensional curved configurations (see, e.g., Brady & Arber 2005; Murawski et al. 2005; Brady et al. 2006; Selwa et al. 2006, 2007); see Terradas (2009) for a review.

The aim of this work is to examine two physical mechanisms that may be involved in the fast attenuation of the observed vertical coronal loop oscillations, namely wave leakage through wave tunneling and resonant absorption. Regarding wave tunneling, Brady & Arber (2005) considered a curved flux tube with enhanced density at the center and excited transverse motions of the tube with a driver located at one footpoint. Among other results, they showed that in this model there are no perfectly confined modes, only modes with varying degrees of leakage by tunneling. Verwichte et al. (2006a) considered the same semicircular slab with a piecewise density. The density profile can

The Astrophysical Journal, 763:16 (11pp), 2013 January 20 Rial et al.

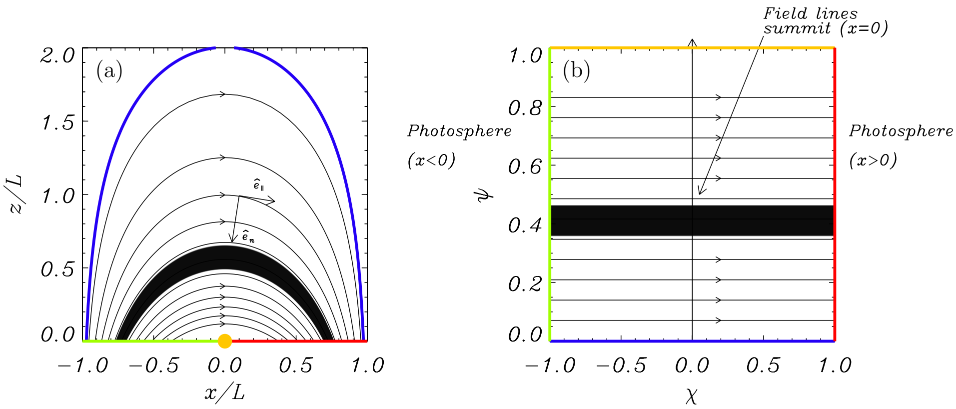

Figure 1. (a) Magnetostatic configuration of the potential coronal arcade described by Equations (1) and (2), where the solid curves represent magnetic field lines, given by $A(x, z) =$ constant. These curves in the xz-plane become arcade surfaces in three dimensions. In this model, z measures the vertical distance from the base of the corona (placed at $z = 0$). The black region represents a coronal loop embedded in the arcade. The two orthogonal unit vectors defining the normal and the parallel directions, $\hat{e}_n$ and $\hat{e}_\parallel$, are also shown at a particular point. (b) Same as (a) in the $\chi\psi$-plane. Curved magnetic field lines in the xz-plane become straight lines in this flux coordinate system and therefore a curved loop becomes a straight slab. The four boundaries are color-coded to show their correspondence with lines and points in panel (a).

be modified by means of a parameter, and the authors concluded that only for a particular value of this parameter, which leads to an Alfvén speed linearly varying with r, can the system support trapped wave modes. Later, Brady et al. (2006) studied a straight slab model that includes a variable tunneling region in order to compare the results for a straight cylinder and the semi-circular slab considered by Brady & Arber (2005). Finally, in Verwichte et al. (2006b) the authors extended the study done by Verwichte et al. (2006a) by considering the models for which non-trapped modes can be found. They concluded that the resulting modes are damped by lateral leakage, which includes the wave tunneling mechanism. In this paper the authors classified the modes that leak energy into leaky and tunneling. The model used by these authors is very similar to our model when perpendicular propagation is not considered. Damping by resonant absorption, which is caused by the inhomogeneity of the medium, has mainly been studied in single magnetic slabs (Terradas et al. 2005; Arregui et al. 2007) and in single magnetic cylinders (Ruderman & Roberts 2002; Terradas et al. 2006a), for example. Nevertheless, more complex equilibrium models have also been considered (Van Doorsselaere et al. 2004; Terradas et al. 2006b, 2008a). Rial et al. (2010) have recently considered the coupling of fast and Alfvén modes in a potential coronal arcade with a three-dimensional propagation of perturbations. This study shows that because of the inclusion of perpendicularly propagating fast wave, energy can easily be converted into Alfvén wave energy at given magnetic surfaces by means of resonant coupling. Our analysis aims to extend the model of Rial et al. (2010) by including a density enhancement in a curved magnetic configuration in order to study how three-dimensional propagation affects the efficiency of the damping of vertical loop oscillations by wave leakage and how the inhomogeneity of the corona can produce coupling of modes and energy transfer. Our preferred procedure to perform this investigation is to first study the normal modes of the equilibrium configuration, which allows us to obtain insight into its dynamics. Nevertheless, we lack a suitable tool for this task, and for this reason we numerically solve the initial value problem using the linearized MHD equations.

The paper is organized as follows. In Section 2, we describe the equilibrium configuration as well as the approximations made in this work. In Section 3, we present the linear ideal MHD wave equations with three-dimensional propagation of perturbations. In Section 4, we describe the numerical setup together with the initial and boundary conditions. In Section 5, we will describe the linear wave propagation properties of coupled fast and Alfvén waves in a two-dimensional coronal loop including three-dimensional propagation. Finally, in Section 6 we will give the conclusions and a discussion of the results.

2. EQUILIBRIUM CONFIGURATION

The equilibrium magnetic field is a potential arcade contained in the xz-plane (see Oliver et al. 1993 for more details). In Cartesian coordinates the flux function is

$$A(x, z) = B_0\Lambda_B \cos\left(\frac{x}{\Lambda_B}\right) \exp\left(-\frac{z}{\Lambda_B}\right), \quad (1)$$

and the magnetic field components are given by

$$B_x(x, z) = B_0 \cos\left(\frac{x}{\Lambda_B}\right) \exp\left(-\frac{z}{\Lambda_B}\right),$$

$$B_z(x, z) = -B_0 \sin\left(\frac{x}{\Lambda_B}\right) \exp\left(-\frac{z}{\Lambda_B}\right). \quad (2)$$

In these expressions, Λ_B is the magnetic scale height, which is related to the lateral extent of the arcade, $2L$, by $\Lambda_B = 2L/\pi$, and B_0 is the magnetic field strength at the base of the corona ($z = 0$). The overall shape of the arcade is shown in Figure 1(a).

In this paper, gravity is neglected and the $\beta = 0$ approximation is used. Under these assumptions the equilibrium density, ρ, can be chosen arbitrarily. We consider a loop with uniform density, ρ_0, embedded in a corona whose density, ρ_e, is also uniform and smaller than that of the loop by a factor 10, i.e., $\rho_e = \rho_0/10$; see Figure 1(a). This density configuration is chosen so as to minimize numerical problems in the time-dependent simulations. The vertical density profile at the arcade center is shown in Figure 2(b).

The combination of the magnetic field of Equation (2) with this sharp density profile leads to the following Alfvén speed distribution:

$$v_A(x, z) = \begin{cases} v_{A0} \exp\left(-\frac{z}{\Lambda_B}\right), & \text{inside the loop,} \\ v_{Ae} \exp\left(-\frac{z}{\Lambda_B}\right), & \text{otherwise,} \end{cases} \quad (3)$$

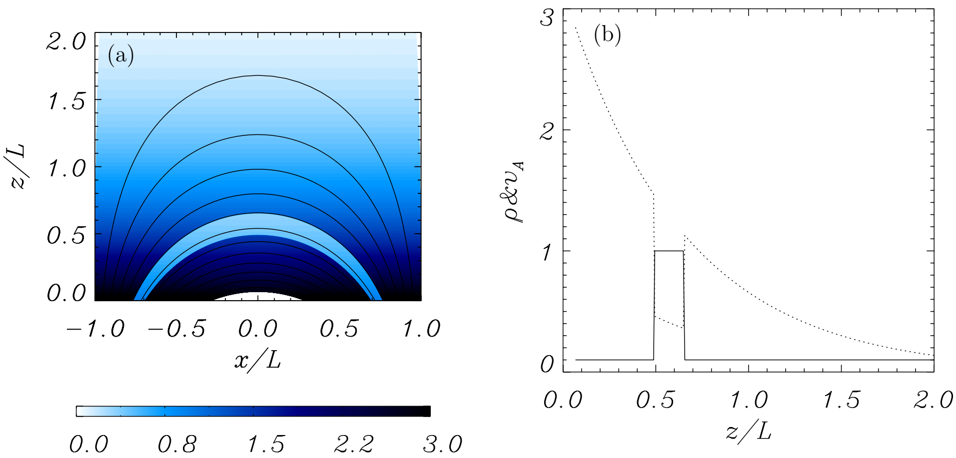

Figure 2. (a) Two-dimensional distribution of the Alfvén speed in Cartesian coordinates. Some magnetic field lines (black curves) have been represented. (b) Vertical variation along the z-axis of the density (solid line) and Alfvén speed (dotted line) for the coronal loop configuration of Figure 1.

(A color version of this figure is available in the online journal.)

where $v_{A0} = B_0/\sqrt{\rho_0\mu_0}$ and $v_{Ae} = B_0/\sqrt{\rho_e\mu_0}$ are the Alfvén speed inside and outside the loop at the base of the corona ($z = 0$). This formula gives v_A at any point on the xz-plane. Note that the Alfvén speed varies both along and across magnetic field lines in our curved configuration; see Figure 2(a). Our choice of the density profile leads to a plasma field structuring that is inherently two-dimensional.

Oliver et al. (1996) and Arregui et al. (2004a) showed that an appropriate description of normal modes in a curved structure, such as the one considered here, can be obtained by solving the MHD equations in flux coordinates, which are determined by the previous selection of the equilibrium field in Equation (2). Appropriate flux coordinates are given by the following expressions:

$$\psi(x,z) = \cos\left(\frac{x}{\Lambda_B}\right)\exp\left(-\frac{z}{\Lambda_B}\right), \quad 0 \leqslant \psi \leqslant 1, \tag{4}$$

$$\chi(x,z) = \frac{\sin\left(\frac{x}{\Lambda_B}\right)\exp\left(-\frac{z}{\Lambda_B}\right)}{(1-\psi^2)^{1/2}}, \quad -1 \leqslant \chi \leqslant 1, \tag{5}$$

where ψ and χ are the coordinates across and along the equilibrium magnetic field lines. The normalization of the length of all field lines to the same value is achieved by the factor $(1-\psi^2)^{1/2}$ in the denominator of Equation (5). One of the advantages of using this coordinate system is that it enables us to include the whole coronal arcade in the finite domain $\psi \in [0, 1]$, $\chi \in [-1, 1]$. In this domain magnetic field lines are straight and each of them is represented by a different value of ψ. In addition, the magnetic field strength depends on both ψ and χ. The shape of the potential arcade and the coronal loop in these field-related coordinates is shown in Figure 1(b).

3. MAGNETOHYDRODYNAMIC EQUATIONS AND LINEAR WAVES

In order to study small-amplitude oscillations in our potential arcade with an embedded loop the previous equilibrium is perturbed. For linear and adiabatic MHD perturbations in the zero-β approximation the relevant equations are

$$\rho\frac{\partial \mathbf{v}_1}{\partial t} = \frac{1}{\mu_0}(\nabla\times\mathbf{B}_1)\times\mathbf{B}, \tag{6}$$

$$\frac{\partial \mathbf{B}_1}{\partial t} = \nabla\times(\mathbf{v}_1\times\mathbf{B}), \tag{7}$$

where ρ and $\mathbf{B}$ are the equilibrium density and magnetic field and the subscript 1 is used to represent the perturbed velocity, $\mathbf{v}_1$, and magnetic field, $\mathbf{B}_1$.

The numerical procedure to solve Equations (6) and (7) is first presented for a general equilibrium structure. In order to characterize the directions of interest related to the polarization of each wave type it is advantageous to use field-related components instead of Cartesian ones. The unit vectors in the directions normal, perpendicular, and parallel to the equilibrium magnetic field are given by

$$\hat{e}_n = \frac{\nabla A}{|\nabla A|},$$
$$\hat{e}_\perp = \hat{e}_y,$$
$$\hat{e}_\parallel = \frac{\mathbf{B}}{|\mathbf{B}|}, \tag{8}$$

where A is the flux function, given by Equation (1), and $|\mathbf{B}| = B_0\exp(-z/\Lambda_B)$ is the magnetic field strength at a point (x, z). Using this new basis the perturbed velocity and magnetic field are written as $\mathbf{v}_1 = v_{1n}\hat{e}_n + v_{1y}\hat{e}_y + v_{1\parallel}\hat{e}_\parallel$ and $\mathbf{B}_1 = B_{1n}\hat{e}_n + B_{1y}\hat{e}_y + B_{1\parallel}\hat{e}_\parallel$. In a low-$\beta$ plasma and in the absence of perpendicular propagation, the three components are associated with the velocity perturbation of the three types of waves that can be excited, namely v_{1n} for fast waves, v_{1y} for Alfvén waves, and $v_{1\parallel}$ for slow waves. Note that here $v_{1\parallel} = 0$ because $\beta = 0$.

As the equilibrium is invariant in the y-direction, we can Fourier analyze all perturbed quantities in the y-direction by making them proportional to $\exp(ik_y y)$, where k_y is the perpendicular wave number. In this way, three-dimensional propagation is introduced and each Fourier component can be studied separately. As a result of this Fourier analysis, the perturbed perpendicular velocity and magnetic field components are purely imaginary quantities and as our code is designed to handle real quantities—it is necessary to make the appropriate redefinitions (see Rial et al. 2010, for more details) to treat them as real. The field-related components of the MHD wave equations can be cast in the following manner:

$$\frac{\partial v_{1n}}{\partial t} = \frac{|\mathbf{B}|}{\mu_0 \rho}[(B_a - \psi_a \partial_\psi - \chi_a \partial_\chi) B_{1\|} + (\psi_s \partial_\psi + \chi_s \partial_\chi - B_s) B_{1n}], \tag{9}$$

$$\frac{\partial v_{1y}}{\partial t} = \frac{|\mathbf{B}|}{\mu_0 \rho}[(\psi_s \partial_\psi + \chi_s \partial_\chi) B_{1y} + k_y B_{1\|}], \tag{10}$$

$$\frac{\partial B_{1n}}{\partial t} = |\mathbf{B}|(\psi_s \partial_\psi + \chi_s \partial_\chi + B_s) v_{1n}, \tag{11}$$

$$\frac{\partial B_{1y}}{\partial t} = |\mathbf{B}|(\psi_s \partial_\psi + \chi_s \partial_\chi) v_{1y}, \tag{12}$$

$$\frac{\partial B_{1\|}}{\partial t} = -|\mathbf{B}|[k_y v_{1y} + (\psi_a \partial_\psi + \chi_a \partial_\chi + B_a) v_{1n}], \tag{13}$$

where ∂_ψ and ∂_χ are the derivatives normal and parallel to field lines,

$$\begin{aligned} \partial_\psi &\equiv \hat{e}_n \cdot \nabla, \\ \partial_\chi &\equiv \hat{e}_\| \cdot \nabla. \end{aligned} \tag{14}$$

Furthermore, the quantities ψ_s, ψ_a, χ_s, χ_a, B_s, and B_a, which represent the derivatives of the flux coordinates and the unperturbed magnetic field strength along (subscript "s") and across (subscript "a") magnetic field lines, are defined in Oliver et al. (1996),

$$\begin{aligned} \psi_a &= \frac{1}{|\mathbf{B}|}(\nabla A \cdot \nabla)\psi, \quad \psi_s = \frac{1}{|\mathbf{B}|}(\mathbf{B} \cdot \nabla)\psi, \\ \chi_a &= \frac{1}{|\mathbf{B}|}(\nabla A \cdot \nabla)\chi, \quad \chi_s = \frac{1}{|\mathbf{B}|}(\mathbf{B} \cdot \nabla)\chi, \\ B_a &= \frac{1}{|\mathbf{B}^2|}(\nabla A \cdot \nabla)B, \quad B_s = \frac{1}{|\mathbf{B}^2|}(\mathbf{B} \cdot \nabla)B. \end{aligned} \tag{15}$$

Note that this general derivation and implementation of the governing equations enables us to apply the scheme to other configurations for which flux coordinates can be defined. It is only necessary to provide expressions for the variables in Equations (15), which in the present configuration are

$$\begin{aligned} \psi_a &= \frac{(\psi^2 + \chi^2(1-\psi^2))^{1/2}}{\Lambda_B}, \quad \psi_s = 0, \\ \chi_a &= \frac{(\psi^2 + \chi^2(1-\psi^2))^{1/2}\psi^2}{\Lambda_B(1-\psi^2)}, \quad \chi_s = \frac{(\psi^2 + \chi^2(1-\psi^2))^{1/2}}{\Lambda_B(1-\psi^2)^{1/2}}, \\ B_a &= \frac{\psi}{(\psi^2 + \chi^2(1-\psi^2))^{1/2}\Lambda_B}, \quad B_s = \frac{\chi(1-\psi^2)^{1/2}}{(\psi^2 + \chi^2(1-\psi^2))^{1/2}\Lambda_B}. \end{aligned} \tag{16}$$

Equations (9)–(13) constitute a set of coupled partial differential equations with non-constant coefficients that describe the propagation of fast and Alfvén waves. When $k_y = 0$, Equations (9)–(13) constitute two independent sets of equations. The two equations for v_{1y} and B_{1y} are associated with Alfvén wave propagation. On the other hand, the three equations for the remaining variables, v_{1n}, B_{1n}, $B_{1\|}$, describe fast wave propagation.

4. NUMERICAL METHOD AND INITIAL AND BOUNDARY CONDITIONS

The obtained set of differential equations are too complicated to have analytical or simple numerical solutions. For this reason we have solved them with a numerical code, called MoLMHD, using flux coordinates. This particular choice of coordinates is crucial for the proper computation of the solutions, and has been overlooked in previous numerical studies. The numerical code (see Bona et al. 2009; Terradas et al. 2008b, for details about the method) makes use of the so-called method of lines for the discretization of the derivatives and the time and space variables are treated separately. For the temporal part, a fourth-order Runge-Kutta method is used, while for the spatial discretization a finite-difference method with a fourth-order centered stencil is chosen. For a given spatial resolution, the time step is selected so as to satisfy the Courant condition. Finally, a fourth-order artificial dissipation has been added to have more robust stability. In the simulations, we have checked that the effect of the artificial dissipation does not affect the solution, while it is enough to eliminate possible high-frequency numerical modes.

We try to mimic the observed vertical oscillations of coronal loops in the corona when a sudden release of energy occurs and perturbs the structure. Since we are concerned with the excitation of fast waves, our initial perturbation is such that only the normal velocity component is disturbed, whereas all the other variables (v_{1y}, B_{1n}, B_{1y}, $B_{1\|}$) are initially set to zero. To initially excite the system we have chosen a two-dimensional profile in v_{1n} with, respectively, a cosine function and a Gaussian profile along and across field lines,

$$v_{1n}(\chi, \psi) = v_0 \cos(k_\| \chi) \exp\left[-\left(\frac{\psi - \psi_0}{a}\right)^2\right]. \tag{17}$$

This expression represents an initial disturbance that perturbs a range of field lines centered about the field line $\psi = \psi_0$. Here v_0 is the initial amplitude of the disturbance, a is related to the range of field lines initially affected by the perturbation, and $k_\|$ is the wave number of the disturbance along the magnetic field. This symmetric initial profile does not represent a general disturbance in the solar corona, but it is selected in order to mainly excite the vertical fundamental fast kink mode, with one maximum along field lines. This can be achieved by an adequate choice of $k_\|$. Nevertheless, this initial disturbance does not ensure that only the fundamental mode will be excited because its longitudinal dependence is not sinusoidal.

The implementation of the appropriate boundary conditions in the numerical code is an important issue. The reflection of waves at the bottom boundary, due to the large inertia of the photospheric plasma, is accomplished by imposing line-tying boundary conditions at $z = 0$. This is achieved by imposing the velocity field and the derivative perpendicular to the boundary of the velocity and magnetic field to zero. In the rest of the boundaries (top and lateral walls), the spatial derivative of the velocity and magnetic field is set to zero, providing quite realistic flow-through conditions. For the numerical scheme used here, these boundary conditions have been shown to be in general quite stable. As the equations are solved in flux coordinates, one then needs to know the correspondence between the system boundaries from Cartesian to field-related coordinates, see Figure 1, to apply the correct boundary conditions. Although the whole arcade can be reproduced in flux coordinates, considering the complete range $0 \leqslant \psi \leqslant 1$ causes numerical issues, so we restrict ourselves to the range $[0.034, 0.9]$ in the ψ-direction. This implies that extremely low and extremely high field lines are discarded in the numerical simulations.

5. NUMERICAL RESULTS

The results presented in this section have been obtained with the numerical solution of Equations (9)–(13) after an initial

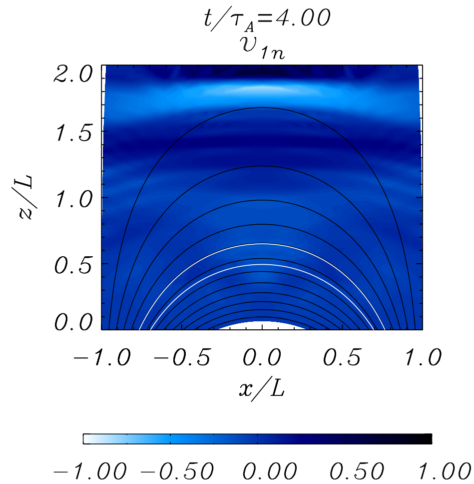

Figure 3. Snapshot of the two-dimensional distribution of the normal velocity component for $k_y = 0$. Some magnetic field lines (black curves) and the edge of the coronal loop (white lines) have been represented.

(An animation and color version of this figure is available in the online journal.)

perturbation given by Equation (17) with $\psi_0 = 0.41$ and $a = 0.05$ is launched. Different values of k_y have been considered ($k_y L = 0, 5, 16, 60$). The two-dimensional variation of v_{1n} and v_{1y} for some of these simulations is presented as animations associated with Figures 3 and 5. Time in these animations and in subsequent plots is given in units of $\tau_A = L/v_{A0}$.

5.1. Wave Propagation in the Plane of the Arcade—Wave Leakage

We first consider wave propagation in the plane of the arcade ($k_y = 0$). As can be seen in the animation accompanying Figure 3, the initial perturbation produces traveling disturbances across the magnetic surfaces that propagate away from the density enhancement. After a short time ($t/\tau_A \sim 5$) the loop contains very little energy, and so these disturbances can be interpreted as a combination of leaky modes that the loop structure is unable to confine. This interpretation is also supported by the time evolution of the normal velocity component at the center of the loop (Figure 4(a)), which displays a strong damping such that, for $t/\tau_A \gtrsim 5$, the velocity has an almost null amplitude inside the loop.

A convenient way to quantify the wave energy leakage and the damping is to use the total energy density computed both in the full domain and in the interior of the loop. We use the following formula to calculate the energy density at a given position and time,

$$\delta E(\mathbf{r}, t) = \frac{1}{2}\left[\rho\left(v_{1n}^2 + v_{1y}^2\right) + \frac{1}{\mu_0}\left(B_{1n}^2 + B_{1y}^2 + B_{1\|}^2\right)\right]. \quad (18)$$

The total energy density in a spatial domain, D, of the xz-plane can be computed from the spatial integration of $\delta E(\mathbf{r}, t)$,

$$E(t) = \int_D \delta E(\mathbf{r}, t)\, dx\, dz. \quad (19)$$

In our plots, this quantity is normalized by dividing it by the initial energy density over the whole numerical domain, $E(0)$.

Figure 4(b) shows the total energy density integrated over the full domain, the interior of the loop, and the external region. We can see that the loop is unable to trap wave energy and that, after a little more than $5\tau_A$, it has already transferred all its energy to the outside medium. After this time, the wave energy outside the loop equals the energy in the full domain. Because of this wave leakage, the total energy of the system continuously decreases and when the last leaky waves carrying a non-negligible amount of energy reach the domain boundaries (i.e., at $t/\tau_A \sim 10$), it is practically zero; see also the animation of Figure 3.

These results differ from what is obtained in a line-tied straight slab model of a coronal loop (Terradas et al. 2005), in which the kink mode of the loop remains oscillating after the initial leaky phase, since the density enhancement is able to trap part of the energy of the initial perturbation. In a curved magnetic topology in which the magnetic field strength drops with height, the presumed density structure in and around coronal loops is such that the Alfvén frequency above the loop is smaller than that of the transverse modes and so the energy deposited initially in the loop is simply radiated as a combination of leaky modes, and thus no trapped solutions are found, as was already pointed out by Murawski et al. (2005), Selwa et al. (2005), Selwa et al. (2006), Brady & Arber (2005), Verwichte et al. (2006a, 2006b), and Selwa et al. (2007).

5.2. Wave Propagation in Three Dimensions—Wave Trapping

Terradas et al. (2006b) showed that in a toroidal loop structure wave leakage is much less effective than in slab geometry. Following the same idea, Arregui et al. (2007) used a simple three-dimensional straight slab model to demonstrate that in the case of a slab, introducing oblique propagation increases

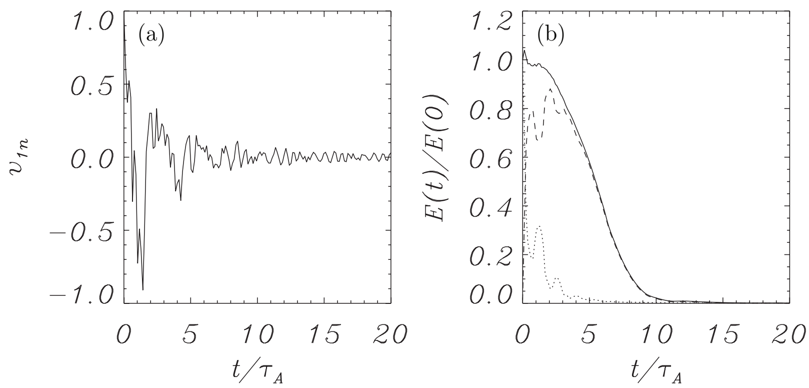

Figure 4. Results for $k_y = 0$. (a) Temporal evolution of the normal velocity component, v_{1n}, at the loop center ($x = 0$, $z/L = 0.56$). (b) Normalized energy density in the whole domain (solid thick line), inside the loop (dotted line), and outside the loop (dashed line) as a function of time. The two-dimensional temporal evolution of v_{1n} is presented in the animation associated with Figure 3.

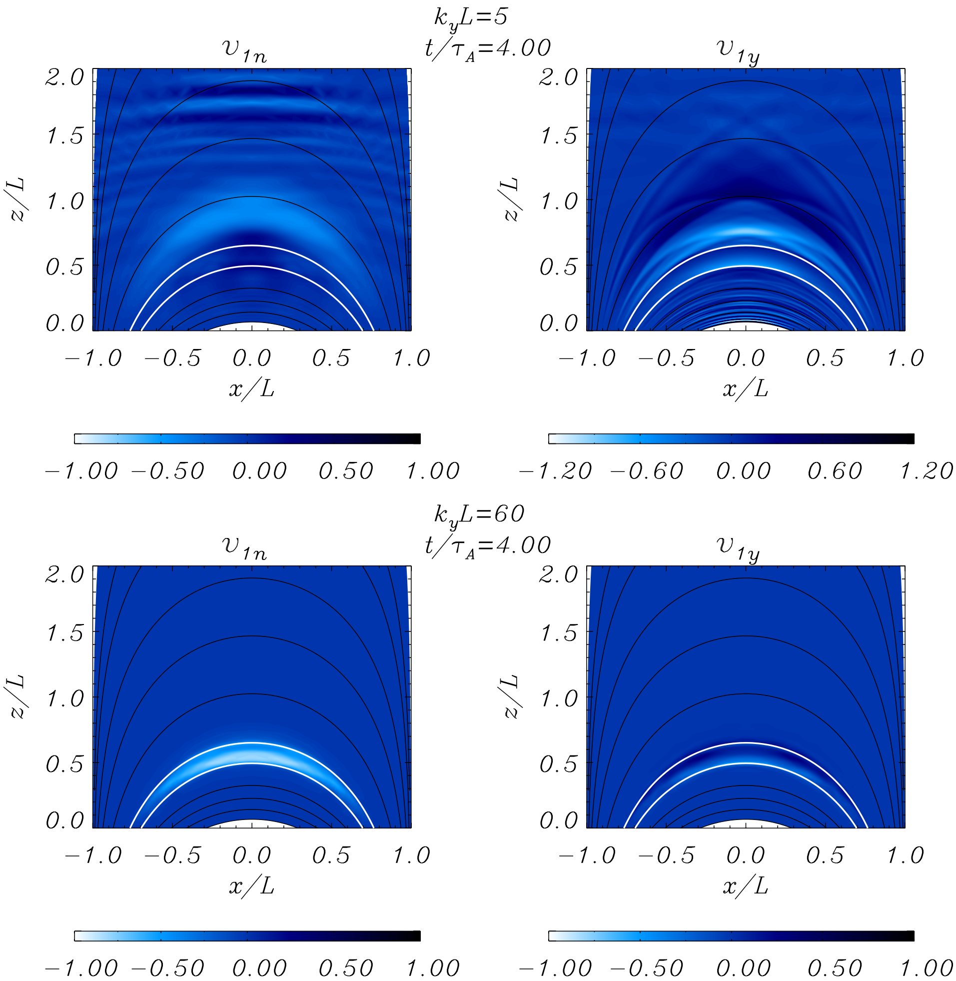

Figure 5. Snapshots of the two-dimensional distribution of the normal and perpendicular velocity components for $k_y L = 5$ (top panels) and $k_y L = 60$ (bottom panels). Some magnetic field lines (black curves) and the edge of the coronal loop (white lines) have been represented.
(Animations and color version of this figure are available in the online journal.)

the spatial confinement of the kink mode around the loop. Van Doorsselaere et al. (2009) have also shown that a cylindrical tube is a more efficient wave guide than the slab model, and less energy is allowed to leak. When a potential arcade is used as the equilibrium structure, the oblique propagation of the slab corresponds to perpendicular propagation, which means the introduction of the k_y wave number. If the previous results for the kink mode with oblique propagation in a coronal slab are also valid in the present loop configuration, we expect that an initial perturbation will excite both leaky waves (which will leave the system in a similar manner as found in Section 5.1) and trapped modes (which will retain energy in the system). A comment about the term "trapped" mode used in this paper is in order. In our plasma configuration, the local cutoff frequency depends on position because of the Alfvén speed inhomogeneity and the inclusion of perpendicular wave propagation. For this reason, an eigenfunction that is evanescent in a certain region can change its character to propagating in another part of the system, and so wave energy leakage can arise. For this reason we warn that modes termed "trapped" here may actually lose energy by this mechanism. If leakage is very small the modes have, for all practical purposes, a trapped behavior.

As in Section 5.1, we have considered an impulsive excitation of the normal velocity component, but now $k_y L = 5$. The temporal evolution of the normal and perpendicular velocity components (see the animations accompanying the top panel of Figure 5) illustrate that there are important differences compared to the case $k_y = 0$ (Figure 3). First of all, some of the energy contained in the initial perturbation goes to the perpendicular variables because $k_y \neq 0$ implies that the perturbed perpendicular components (v_{1y} and B_{1y}) are no longer independent of the normal and parallel ones (v_{1n}, B_{1n}, and $B_{1\|}$). In addition, we have just discussed that for $k_y = 0$ most energy has left the system at $t/\tau_A \sim 10$. For $k_y L = 5$, however, it is apparent that some energy remains in the loop and part of the arcade above it for much longer times. This is interpreted as a signature of the excitation of one or more trapped modes of the system. We next substantiate this claim with a careful inspection of v_{1n}.

We consider the temporal variation of the normal velocity component near the loop center (Figure 6(a)). It displays two distinct behaviors: for $t/\tau_A \lesssim 5$, very short periods are prominent. They correspond to leaky modes that propagate quickly away from the loop. After this leaky phase all that remains is a gentle, damped oscillation. This damping will be discussed in detail later, but let us mention that it is milder than that of the $k_y = 0$ case (Figure 4(a)). The power spectrum of the v_{1n} signal (Figure 6(b)) shows two clear peaks that, according to the interpretation in the previous paragraph, simply reflect the power contained in two trapped modes excited by the initial

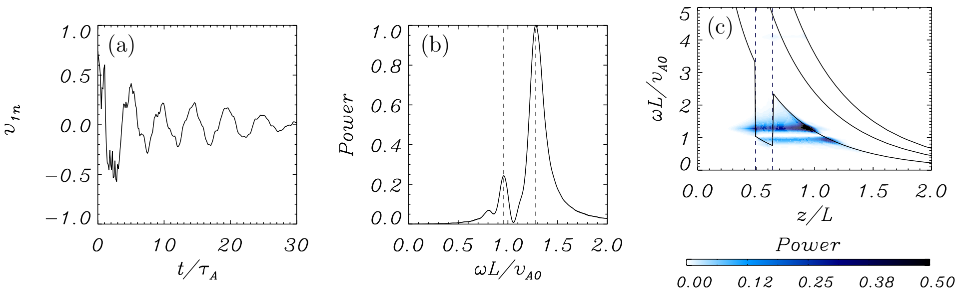

Figure 6. Results for $k_y L = 5$. (a) Temporal evolution of v_{1n} near the loop center ($x = 0$, $z/L = 0.52$). (b) Normalized power spectrum of the signal of panel (a). (c) Power spectrum of v_{1n} at $x = 0$ as a function of height. The three solid lines are, from bottom to top, the frequency of the fundamental Alfvén mode and its first two harmonics. The two dashed lines mark the limits of the coronal loop.

(A color version of this figure is available in the online journal.)

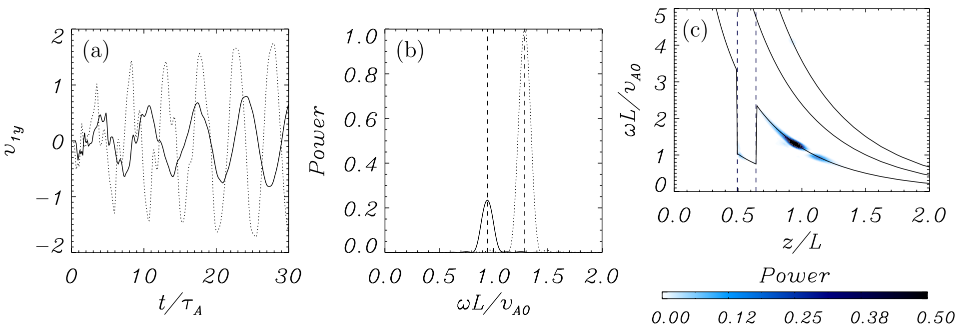

Figure 7. Results for $k_y L = 5$. (a) Temporal evolution of v_{1y} at the points $x = 0$, $z/L = 1.12$ (solid line) and $x = 0$, $z/L = 0.96$ (dotted line). (b) Normalized power spectrum of the signals of panel (a). (c) Power spectrum of v_{1y} at $x = 0$ as a function of height. The three solid lines are, from bottom to top, the frequency of the fundamental Alfvén mode and its first two harmonics. The two dashed lines mark the limits of the coronal loop.

(A color version of this figure is available in the online journal.)

perturbation. An evidence of this would be the presence of power peaks at nearly the same frequency in neighboring points. To investigate this possibility, we consider v_{1n} as a function of t for $x = 0$ and different values of z, compute their power spectra, and stack them in a contour plot (Figure 6(c)). The result is the presence of significant power at two horizontal contours whose frequencies coincide with those found in Figure 6(b), each of them with its characteristic range of heights. From Figure 6(c) we see that the fundamental mode frequency is $\omega L/v_{A0} \sim 0.95$ and that this mode covers the range $0.5 \lesssim z/L \lesssim 1.15$ for $x = 0$. The first harmonic has $\omega L/v_{A0} \sim 1.28$ and covers the range $0.3 \lesssim z/L \lesssim 0.95$ for $x = 0$.

Hence, we conclude that two trapped modes of the system have been excited by the initial perturbation and that this is the reason why the normal velocity component is less strongly attenuated for $k_y = 5$ than for $k_y = 0$. Both modes are spatially distributed over the coronal loop and a large region above it, that is, perpendicular wave propagation increases the wave confinement in the present equilibrium configuration, although for $k_y L = 5$ wave energy around the loop is also found.

5.3. Mode Coupling and Resonant Energy Transfer

Additional information about the temporal evolution of the system comes from the perpendicular velocity component. In Figure 7(a), this perturbed variable is plotted at two different positions at the arcade center ($x = 0$). In both cases v_{1y} displays an oscillatory behavior with a monotonically increasing amplitude and it is evident that the oscillatory period is different at the two positions. This is confirmed by the power spectra of these two signals, each displaying a single peak at one of the frequencies of the normal velocity components found in Figures 6(b) and (c). Next, power spectra of v_{1y} as a function of t along the z-axis are computed and stacked together (Figure 7(c)) and it becomes clear that most of the power of this velocity component is concentrated at two particular heights. To explain this result we recall that in Section 5.2 we mentioned that after the initial perturbation, trapped modes of the system were established by a transfer of energy from v_{1n} to the other perturbed variables, including v_{1y}. But a second, more efficient, process takes place here: the resonant transfer of energy from the trapped modes to the Alfvén modes whose frequencies match those of the former. Figure 6(c) shows that the frequency of the two prominent trapped modes found in Section 5.2 ($\omega L/v_{A0} \sim 0.95$ and $\omega L/v_{A0} \sim 1.28$) intersect the lowest one of the three solid lines included in this plot. These solid lines are the frequencies of the Alfvén continua corresponding to the fundamental mode and its first two harmonics (Oliver et al. 1993). Hence, we conclude that the frequencies of the two trapped modes match that of the fundamental Alfvén mode at two particular heights, namely $z/L \sim 1.12$ and $z/L \sim 0.96$, so that these are the positions where Alfvén energy appears, in agreement with Figure 7(c).

It should be noted that the trapped mode frequencies also match the frequency of Alfvén harmonics, but this happens for heights at which the trapped mode amplitude is negligible. Arregui et al. (2004a) showed that for $k_y \neq 0$ resonant coupling between fast and Alfvén modes can only happen for modes with the same parity along **B**. As a consequence, resonant absorption with Alfvén modes other than the fundamental one does not take place.

So far our description of the resonant absorption process is incomplete because it relies on the information along the z-axis. The animation of the top panel of Figure 5 shows that the largest amplitudes of v_{1y} for $t/\tau_A \gtrsim 10$ are in two ranges of

The Astrophysical Journal, 763:16 (11pp), 2013 January 20 Rial et al.

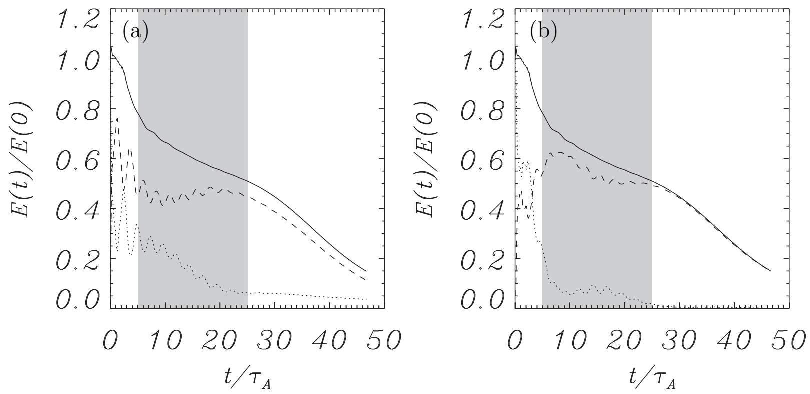

Figure 8. Results for $k_y L = 5$. (a) Normalized energy density integrated over the whole system (solid line), integrated over the coronal loop (dotted line), and integrated over the region outside the loop (dashed line). (b) Normalized energy density integrated over the whole system contained in all perturbed variables (solid line; same as the solid line of panel (a)), in the "fast" perturbed variables, $E_{\rm fast}(t)$ (dotted line), and in the Alfvénic perturbed variables, $E_{\rm Alfven}(t)$ (dashed line).

magnetic surfaces centered about the field lines whose apexes are at $z/L \sim 0.96$ and $z/L \sim 1.12$ (i.e., at the resonant positions in Figure 7(c)). A relevant issue is that the Alfvén frequency varies in each of these two ranges of magnetic surfaces and so the resulting Alfvén oscillations soon become out of phase. For long times this phase mixing creates small spatial scales that cannot be resolved by the grid. This leads to the numerical dissipation of wave energy. The importance of this effect will soon become clear.

Equation (19) gives a measure of the energy density in a domain of our system from the spatial integration of Equation (18). In these definitions, $\delta E(\mathbf{r}, t)$ and $E(t)$ contain the contribution from both the Alfvénic perturbed variables (i.e., v_{1y} and B_{1y}) and the perturbed variables characteristic of fast modes for $k_y = 0$ (i.e., v_{1n}, B_{1n}, and $B_{1\|}$). We denote by $E_{\rm Alfven}(t)$ and $E_{\rm fast}(t)$ the spatial integral of these two contributions over the whole system,

$$E_{\rm Alfven}(t) = \int \frac{1}{2}\left(\rho v_{1y}^2 + \frac{1}{\mu_0} B_{1y}^2\right) dx\, dz,$$

$$E_{\rm fast}(t) = \int \frac{1}{2}\left[\rho v_{1n}^2 + \frac{1}{\mu_0}\left(B_{1n}^2 + B_{1\|}^2\right)\right] dx\, dz. \quad (20)$$

Since these two integrals are carried out over the full arcade, it is clear that $E_{\rm Alfven}(t) + E_{\rm fast}(t)$ is equal to $E(t)$ of Equation (19) when D is the complete numerical domain.

Figure 8(a) shows the energy density in the system, inside the loop, and outside it. The first of these three quantities presents three phases: for $t/\tau_A \lesssim 5$ the total energy in the whole system decreases rapidly because of the emission of leaky waves. Then, for $5 \lesssim t/\tau_A \lesssim 25$ (shaded region) the rate of energy decrease is slower, and for $t/\tau_A \gtrsim 25$ it becomes stronger again. To understand the last two phases one must bear in mind the energy loss due to the numerical dissipation of Alfvén waves. During the phase $5 \lesssim t/\tau_A \lesssim 25$ there is a substantial amount of energy in the loop (dotted line in Figure 8(a)) that is slowly transferred to the surrounding medium (dashed line in Figure 8(a)). We know that this process is caused by resonant absorption, by which the energy that could not leak in the initial phase is transferred to the two resonant positions. After $t/\tau_A \sim 25$ almost all the energy in the trapped modes has been given to Alfvén modes, which implies that these modes can no longer "feed" from their previous energy "reservoir." As a result, the numerical dissipation of phase-mixed Alfvén waves proceeds at a faster pace. Figure 8(b) provides support to this interpretation: at $t/\tau_A \sim 10$ almost all the energy has been converted from the "fast"-like perturbations to the Alfvénic ones, but $E_{\rm fast}$ does not become negligible until $t/\tau_A \sim 30$. This means that some conversion to $E_{\rm Alfven}$ still takes place for $10 \lesssim t/\tau_A \lesssim 30$, and so the dissipation of Alfvén waves is slower than in the later phase.

A possible way to quantify what percentage of the initial energy is lost/transformed between leakage and resonant absorption is to evaluate the energy flux in the numerical domain by computing the Poynting vector. Nevertheless, since both mechanisms are acting at the same time it is not straightforward to calculate the individual contributions to the Poynting vector. In addition, when perpendicular wave propagation is considered, fast and Alfvén modes have mixed properties. As a consequence the initial disturbance excites several modes of the system, some of which contribute to the signal (e.g., v_n or v_y) at all times while others have a transitory nature. For these reasons a clear picture cannot be directly obtained from the present results unless the intervening normal modes can be isolated from our simulations. This study is left for future works.

5.4. *Wave Confinement and Resonant Absorption for Large k_y*

To evaluate the influence of the perpendicular wave number on the confinement of wave energy by trapped modes of the loop and the loss of this energy by resonant absorption to Alfvén continuum modes, we consider $k_y L = 60$. We first inspect the two-dimensional temporal evolution of the perturbed velocity components (see animations associated with the bottom panel of Figure 5). There are obvious differences from the numerical simulation with $k_y L = 5$: first of all, there is a lack of wave leakage at the beginning of the simulation, shortly after the initial impulse is released. Second, large velocity amplitudes are only found inside the loop structure, both for the v_{1n} and the v_{1y} components. And third, since the excited trapped modes are not spread outside the loop, there is no resonant absorption at large heights. In summary, these animations seem to indicate a much stronger confinement of the wave energy by the loop. Next, let us confirm this preliminary result.

Now, we consider the temporal variation of the normal and perpendicular velocity components along the z-axis and compute the power spectra of these two signals, which are then stacked to produce a contour plot of the power as a function of height along the z-axis and frequency. Figure 9 reveals that the power of v_{1n} and v_{1y} is concentrated inside the loop and that these signals contain two frequencies around $\omega L/v_{A0} = 0.6$. A comparison of these graphs with Figures 6(c) and 7(c) gives a

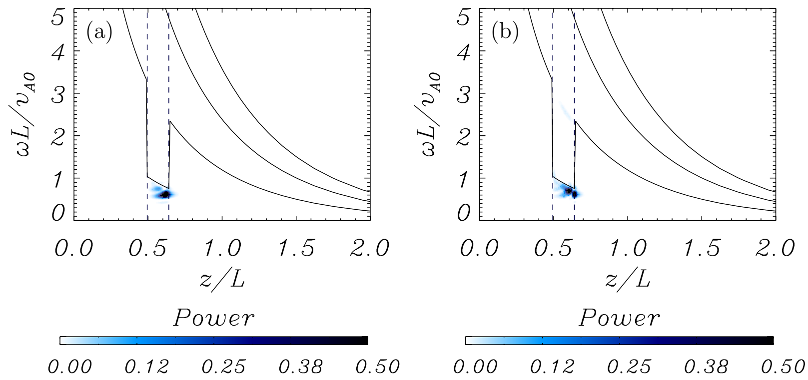

Figure 9. Results for $k_y L = 60$. Power spectrum of (a) v_{1n} and (b) v_{1y} at $x = 0$ as a function of height. The three solid lines are, from bottom to top, the frequency of the fundamental Alfvén mode and its first two harmonics. The two dashed lines mark the limits of the coronal loop.

(A color version of this figure is available in the online journal.)

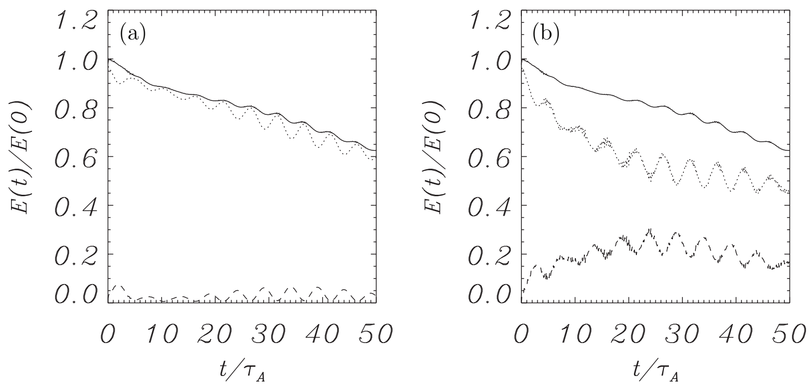

Figure 10. Results for $k_y L = 60$. (a) Normalized energy density integrated over the whole system (solid line), integrated over the coronal loop (dotted line), and integrated over the region outside the loop (dashed line). (b) Normalized energy density integrated over the whole system contained in all perturbed variables (solid line; same as the solid line of panel (a)), in the "fast" perturbed variables, $E_{\text{fast}}(t)$ (dotted line), and in the Alfvénic perturbed variables, $E_{\text{Alfven}}(t)$ (dashed line).

clear confirmation of the stronger wave confinement achieved by the loop for $k_y L = 60$, or in other words, the stronger spatial confinement of the trapped modes of the system. Moreover, since these modes do not extend to large heights, resonant absorption is irrelevant in the present numerical simulation. For resonant absorption to be possible, the trapped modes should have power at a height $z/L \sim 1.5$.

We finally turn our attention to the energetics. Figure 10(a) shows that during the entire simulation there is almost no energy outside the loop, in agreement with our previous findings about the wave guiding properties of the loop for a large perpendicular wave number. Regarding the energy transfer from the "fast" to the Alfvén perturbed variables, Figure 10(b) indicates that while some energy is transferred from the first to the second ones, in the long term the "fast" components retain a larger proportion of energy. The total energy of the system presents a decay in time that, unlike that described in Section 5.3, is constant during the entire simulation. There are two reasons for this difference. First, the loop is such a good wave guide for transverse oscillations when $k_y L = 60$ that very little wave energy is carried out of the system by leaky waves. Then, the initial leaky phase of Figure 8 is not found in Figure 10. Second, for $k_y L = 5$ resonant absorption brings energy to Alfvénic motions at large heights, where the spatial mesh is coarser. This enhances numerical dissipation of Alfvén waves, which results in a strong wave damping. For $k_y L = 60$, however, all wave energy is retained at small heights, where the spatial mesh is denser. Hence, although numerical dissipation cannot be removed from our numerical experiments, it is greatly reduced.

5.5. Realistic Three-dimensional Coronal Loop

Some authors (see, for example, Hollweg & Yang 1988) have extended the results of slab models to cylindrical geometry by using the equivalent of the azimuthal wave number in Cartesian coordinates. The formula that relates both wave numbers is

$$k_y = \frac{m}{r}, \tag{21}$$

where r is the loop radius and m is the azimuthal wave number. Since we are interested in vertical oscillations, caused by the kink mode, we take $m = 1$. Regarding the loop radius, it is obvious from Figure 1(a) that it changes with height, being largest at the apex and smallest at the feet. Since the physical conditions at the loop top are the most determinative for the kink mode properties, r is taken as the loop half width at the apex. Then we obtain $k_y L = 16$.

To study the properties of vertical oscillations for this value of k_y we first consider the temporal evolution of v_{1n} at a point inside the loop (see Figure 11(a)). The periodic behavior that was found for $k_y L = 5$ is also present in this case, although the attenuation rate is smaller now (compare with Figure 6(a)). This suggests a better confinement of the vertical oscillations for $k_y L = 16$ and to quantify this effect we compute the power spectra of v_{1n} along the z-axis and plot them together as a contour plot, which is presented in Figure 11(c). It is clear that two trapped modes, with frequencies $\omega L/v_{A0} = 0.74$ and $\omega L/v_{A0} = 0.88$, are excited by the initial perturbation and that they are spatially spread along a wide range of heights. Although most of the energy is contained in the fundamental trapped mode and, in particular, inside the

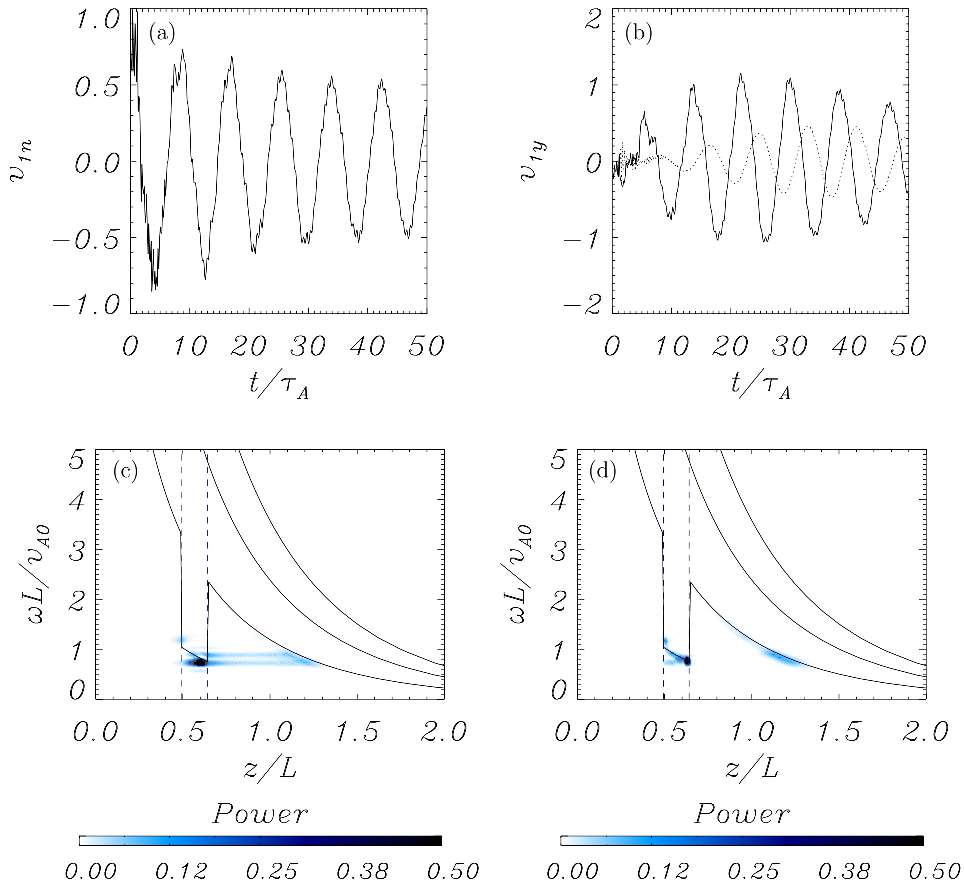

Figure 11. Results for $k_y L = 16$. (a) Temporal evolution of the v_{1n} velocity component at $x = 0$, $z/L = 0.61$. (b) Temporal evolution of the v_{1y} velocity component at $x = 0$, $z/L = 0.61$ (solid line) and at $x = 0$, $z/L = 1.2$ (dotted line). Power of the normal velocity component for $x = 0$ as a function of z and the dimensionless frequency. (d) Power of the perpendicular velocity component for $x = 0$ as a function of z and the dimensionless frequency. In panels (c) and (d), the solid lines are the theoretical frequencies of the Alfvén continua given by Oliver et al. (1993).

(A color version of this figure is available in the online journal.)

loop, the two trapped mode frequencies match the fundamental continuum Alfvén frequency around $z/L = 1.1$–1.3. This opens the possibility of resonant absorption playing a role in the damping of the trapped modes. To investigate this effect, we plot the perpendicular velocity component at two points along the z-axis (Figure 11(b)).

The first of these two signals is taken inside the loop, at its top boundary, while the second signal is gathered at one of the resonant positions. Their amplitude aside, these two signals are different in that the first one has an appreciable amplitude just after the initial leaky phase (i.e., for $t/\tau_A \gtrsim 5$), whereas the second one is initially negligible and only starts to grow after $t/\tau_A \sim 10$, at a rate larger than that of its counterpart inside the loop. To understand these two behaviors we plot the power spectrum of v_{1y} as a function of height and frequency (cf. Figure 11(d)), which confirms the presence of large power in the transverse velocity component both inside the loop and in the resonant position. The power in the range $z/L = 1.1$–1.3 is concentrated around the Alfvén continuum frequency and we interpret this to be the signature of resonant absorption. On the other hand, inside the loop (i.e., in the range $z/L = 0.5$–0.64 there is power at the Alfvén continuum frequency but also for $\omega L/v_{A0} \sim 0.74$, that is, at the frequency of the fundamental mode detected in the normal velocity component. We thus conclude that the perpendicular velocity component inside the loop exists both as part of the trapped mode excited by the initial perturbation and by the resonant transfer of energy from this trapped mode to Alfvén continuum modes.

6. CONCLUSIONS

In this paper, we have studied the temporal evolution of fast and Alfvén waves in a curved coronal loop embedded in a magnetic potential arcade, in order to assess the relevance of three-dimensional propagation of perturbations on the damping of vertical loop oscillations by wave leakage and resonant absorption.

When perpendicular propagation is not included (i.e., when waves are constrained to propagate in the plane of the arcade), a transverse impulsive perturbation produces a combination of leaky modes and the loop is unable to trap energy in the form of vertical kink oscillations. The energy deposited initially in the loop is emitted rapidly to the external medium. This result confirms previous findings in the sense that in a curved coronal loop slab model damping by wave leakage is an efficient mechanism for the attenuation of vertical loop oscillations.

When three-dimensional propagation of waves is considered, two new effects are found. First, damping by wave leakage is less efficient and the loop is able to trap part of the energy deposited by the initial disturbance in transverse oscillations. The amount of energy trapped by the structure increases for increasing values of the perpendicular wave number. Second, the inclusion of the perpendicular wave number in an inhomogeneous corona produces the resonant coupling between fast and Alfvén modes at those positions where the trapped mode frequency matches that of Alfvén waves. This resonant coupling produces the transfer of energy from the fast wave components to the Alfvénic oscillations. In our model, the loop boundary is sharp and so there is no smooth density transition that allows resonant absorption to happen in this position. Hence, this energy transfer does not occur at the loop boundary, but at locations in the external medium, in particular above the coronal loop.

The numerical simulations presented in this work show vertical loop oscillations that are damped by a competition between wave leakage from the slab and resonant absorption in the environment. It would be interesting to know how much of the initial pulse energy is lost by each of these two mechanisms, but this is beyond the scope of this paper and will be investigated in the future.

Let us stress that slab models of curved coronal loops in the absence of perpendicular propagation give rise, in general, to damping times by wave leakage shorter than those observed. On the contrary, as we have demonstrated in this work, perpendicular propagation is a way to obtain damping times compatible with observations. It must be noted that the efficiency of wave leakage strongly depends on the chosen Alfvén frequency profile and the loop density contrast (which in turn determine the thickness of the evanescent barrier) and observed damping times can be reproduced for certain parameter values. In our work, we have only examined one specific Alfvén frequency profile and we therefore cannot come to a full conclusion on the role of wave leakage and the external resonant absorption for our field topology. Resonant absorption at the loop boundary should be added to the present model to achieve a better description of damped transverse loop oscillations.

The authors acknowledge MICINN and MINECO for the funding provided under projects AYA2006-07637, AYA2011-22846, and FEDER funds and the Government of the Balearic Islands for the funding provided through the Grups Competitius scheme and FEDER funds.

REFERENCES

Arregui, I., Oliver, R., & Ballester, J. L. 2004a, A&A, 425, 729
Arregui, I., Oliver, R., & Ballester, J. L. 2004b, ApJ, 602, 1006
Arregui, I., Terradas, J., Oliver, R., & Ballester, J. L. 2007, SoPh, 246, 213
Aschwanden, M. J. 2009, SSRv, 149, 31
Aschwanden, M. J., de Pontieu, B., Schrijver, C. J., & Title, A. M. 2002, SoPh, 206, 99
Aschwanden, M. J., Fletcher, L., Schrijver, C. J., & Alexander, D. 1999, ApJ, 520, 880
Aschwanden, M. J., & Schrijver, C. J. 2011, ApJ, 736, 102
Bona, C., Bona-Casas, C., & Terradas, J. 2009, JCoPh, 228, 2266
Brady, C. S., & Arber, T. D. 2005, A&A, 438, 733
Brady, C. S., Verwichte, E., & Arber, T. D. 2006, A&A, 449, 389
Čadež , V. M., & Ballester, J. L. 1995a, A&A, 296, 537
Čadež , V. M., & Ballester, J. L. 1995b, A&A, 296, 550
Del Zanna, L., Schaekens, E., & Velli, M. 2005, A&A, 431, 1095
Díaz, A. J., Zaqarashvili, T., & Roberts, B. 2006, A&A, 455, 709
Edwin, P. M., & Roberts, B. 1983, SoPh, 88, 179
Goossens, M. 1991, in Mechanisms of Chromospheric and Coronal Heating, ed. P. Ulmschneider, E. R. Priest, & R. Rosner (Berlin: Springer-Verlag), 480
Goossens, M., Andries, J., & Aschwanden, M. J. 2002, A&A, 394, 39
Goossens, M., Poedts, S., & Hermans, D. 1985, SoPh, 102, 51
Heyvaerts, J., & Priest, E. R. 1983, A&A, 117, 220
Hollweg, J. V., & Yang, G. 1988, JGR, 93, 5423
Hori, K., Ichimoto, K., Sakurai, T., Sano, I., & Nishino, Y. 2005, ApJ, 618, 1001
Murawski, K., Selwa, M., & Nocera, L. 2005, A&A, 437, 687
Nakariakov, V. M., & Ofman, L. 2001, A&A, 372, 53
Nakariakov, V. M., Ofman, L., Deluca, E. E., Roberts, B., & Davila, J. M. 1999, Sci, 285, 862
Oliver, R., Ballester, J. L., Hood, A. W., & Priest, E. R. 1993, A&A, 273, 647
Oliver, R., Hood, A. W., & Priest, E. R. 1996, ApJ, 461, 424
Oliver, R., Murawski, K., & Ballester, J. L. 1998, A&A, 330, 726
Poedts, S., & Goossens, M. 1988, A&A, 198, 331
Poedts, S., Hermans, D., & Goossens, M. 1985, A&A, 151, 16
Rial, S., Arregui, I., Terradas, J., Oliver, R., & Ballester, J. L. 2010, ApJ, 713, 651
Roberts, B., Edwin, P. M., & Benz, A. O. 1984, ApJ, 279, 857
Ruderman, M. S., & Roberts, B. 2002, ApJ, 577, 475
Schrijver, C. J., Aschwanden, M. J., & Title, A. M. 2002, SoPh, 206, 69
Selwa, M., Murawski, K., Solanki, S. K., & Wang, T. J. 2007, A&A, 462, 1127
Selwa, M., Murawski, K., Solanki, S. K., Wang, T. J., & Tóth, G. 2005, A&A, 440, 385
Selwa, M., Solanki, S. K., Murawski, K., Wang, T. J., & Shumlak, U. 2006, A&A, 454, 653
Smith, J. M., Roberts, B., & Oliver, R. 1997, A&A, 317, 752
Spruit, H. C. 1981, A&A, 98, 155
Terradas, J. 2009, SSRv, 149, 255
Terradas, J., Arregui, I., Oliver, R., et al. 2008a, ApJ, 679, 1611
Terradas, J., Oliver, R., & Ballester, J. L. 1999, ApJ, 517, 488
Terradas, J., Oliver, R., & Ballester, J. L. 2005, A&A, 441, 371
Terradas, J., Oliver, R., & Ballester, J. L. 2006a, ApJ, 642, 533
Terradas, J., Oliver, R., & Ballester, J. L. 2006b, ApJ, 650, 91
Terradas, J., Oliver, R., Ballester, J. L., & Keppens, R. 2008b, ApJ, 675, 875
Van Doorsselaere, T., Debosscher, A., Andries, J., & Poedts, S. 2004, A&A, 424, 1065
Van Doorsselaere, T., Verwichte, E., & Terradas, J. 2009, SSRv, 149, 299
Verwichte, E., Aschwanden, M. J., Van Doorsselaere, T., Foullon, C., & Nakariakov, V. M. 2009, ApJ, 698, 397
Verwichte, E., Foullon, C., & Nakariakov, V. M. 2006a, A&A, 446, 1139
Verwichte, E., Foullon, C., & Nakariakov, V. M. 2006b, A&A, 449, 769
Verwichte, E., Foullon, C., & Nakariakov, V. M. 2006c, A&A, 452, 615
Verwichte, E., Foullon, C., & Van Doorsselaere, T. 2010, ApJ, 717, 458
Wang, T., Ofman, L., Davila, J. M., & Su, Y. 2012, ApJL, 751, 27
Wang, T. J., & Solanki, S. K. 2004, A&A, 421, 33
Wentzel, D. G. 1979, A&A, 76, 20
White, R. S., & Verwichte, E. 2012, A&A, 537, A49

Chapter 4

Normal modes of transverse coronal loop oscillations from numerical simulations. Rial et al. (2019)

The Astrophysical Journal, 876:86 (12pp), 2019 May 1 https://doi.org/10.3847/1538-4357/ab1417

Normal Modes of Transverse Coronal Loop Oscillations from Numerical Simulations. I. Method and Test Case

S. Rial[1], I. Arregui[2], R. Oliver[1,3], and J. Terradas[1,3]
[1] Departament de Física, Universitat de les Illes Balears, E-07122 Palma de Mallorca, Spain; ramon.oliver@uib.es
[2] Departamento de Astrofísica, Universidad de La Laguna, E-38206 La Laguna, Tenerife, Spain
[3] Institute of Applied Computing & Community Code (IAC3), UIB, Spain
Received 2019 February 1; revised 2019 March 26; accepted 2019 March 26; published 2019 May 7

Abstract

The purpose of this work is to develop a procedure to obtain the normal modes of a coronal loop from time-dependent numerical simulations with the aim of better understanding observed transverse loop oscillations. To achieve this goal, in this paper we present a new method and test its performance with a problem for which the normal modes can be computed analytically. In a follow-up paper, the application to the simulations of Rial et al. is tackled. The method proceeds iteratively and at each step consists of (i) a time-dependent numerical simulation followed by (ii) the Complex Empirical Orthogonal Function (CEOF) analysis of the simulation results. The CEOF analysis provides an approximation to the normal mode eigenfunctions that can be used to set up the initial conditions for the numerical simulation of the following iteration, in which an improved normal mode approximation is obtained. The iterative process is stopped once the global difference between successive approximate eigenfunctions is below a prescribed threshold. The equilibrium used in this paper contains material discontinuities that result in one eigenfunction with a jump across these discontinuities and two eigenfunctions whose normal derivatives are discontinuous there. After six iterations, the approximations to the frequency and eigenfunctions are accurate to $\lesssim 0.7\%$ except for the eigenfunction with discontinuities, which displays a much larger error at these positions.

Key words: methods: numerical – Sun: oscillations – techniques: miscellaneous

1. Introduction

The solar atmosphere is the site of a diversity of magnetohydrodynamic waves and oscillations. Transverse coronal loop oscillations are a prominent example of such events. They take place when a large energy deposition, usually caused by a flare, perturbs an active region magnetic structure, which sets some loops into oscillation (see, e.g., Aschwanden et al. 1999; Nakariakov et al. 1999, for some early observations). These events have been modeled with the help of slab and straight cylindrical loop models, whose normal modes can often be obtained by either analytical or numerical means (see Ruderman & Erdélyi 2009, for a review). Starting with the simplest model that considers the fundamental transverse oscillation of a magnetic flux tube (Roberts 1981; Edwin & Roberts 1983; Nakariakov & Verwichte 2005) several model improvements have included other effects, such as the curvature of coronal loops (van Doorsselaere et al. 2004, 2009; Terradas et al. 2006), longitudinal density stratification (Andries et al. 2005a, 2005b), magnetic field expansion (Ruderman et al. 2008), departure from circular cross section of the tubes (Ruderman 2003), or coronal loop cooling (Aschwanden & Terradas 2008; Morton & Erdélyi 2009). These ingredients have been seen to produce effects on the main wave properties, such as shifts on the frequency and position of the antinodes of the eigenfunctions. Also, the presence of internal fine structuring (Terradas et al. 2008) and/or a continuous cross-field inhomogeneity in density is known to produce important effects, making possible physical processes such as phase-mixing (Heyvaerts & Priest 1983) and resonant damping (Hollweg & Yang 1988; Goossens et al. 2002; Ruderman & Roberts 2002). The more general the model, the more difficult it is to calculate the eigenmodes of the structure, and one has to resort to the study of time-dependent numerical simulations to study these transverse oscillations (Selwa et al. 2006, 2007, 2011a, 2011b; Rial et al. 2013). However, a comparison between the obtained numerical results to observed properties is not as straightforward as it is using simple models. In these simulations, the initial disturbance excites different oscillatory harmonics, whose presence in the results is easily detected by a Fourier analysis of the variables collected at different points in the numerical domain, but this does not give information about the spatial structure of the eigenmodes. Hence, direct comparison between the observed wave properties and the possibly present normal modes becomes difficult. For this reason, we have decided to devise the algorithm described in this paper, which allows us to isolate the eigenmodes present in a numerical simulation. Given the space required to present the algorithm, its application to the time-dependent numerical simulations of Rial et al. (2013), who used a model that takes into account effects such as density stratification, curvature, etc., is left for the second part of this work (S. Rial et al. 2019, in preparation).

Normal modes provide a physical basis for understanding the dynamics of a system. When the equilibrium configuration does not allow a simple solution of the normal mode problem, numerical techniques must be used to determine the normal modes' eigenfunctions and eigenfrequencies. However, general purpose (i.e., for arbitrary equilibria) numerical codes that provide this information cannot be readily found. On the other hand, general purpose numerical codes to solve time-dependent equations are much more abundant. For this reason, being able to determine the normal modes of a system from time-dependent numerical simulations is a practical effort. A spectral analysis of the variables at different points in the spatial domain gives a good indication of the frequencies present in the results, but the very relevant spatial structure of the associated eigenmodes cannot be easily achieved with such analysis. Hence, a means of extracting the spatial profile of eigenfunctions together with their associated oscillatory frequencies from time-dependent simulations is desirable. In this way, the results can be compared to observations to ascertain the presence of a given normal mode in the coronal structure under study. The Complex Empirical Orthogonal Function (CEOF; see von Storch & Zwiers 1999; Hannachi et al. 2007) analysis is a tool that satisfies these requirements: it takes as its input the numerical values of one or more variables over a spatial domain and for a given time span, and returns the spatial and temporal information about the main modes of variability contained in the data, which in our case will be the main eigenmodes present in the time-dependent numerical simulations. Thus, the aim of retrieving the normal mode features is feasible with this procedure.

The main advance of this paper is the repeated application of the described combination of time-dependent numerical simulations and CEOF analysis. The latter results allow us to determine initial conditions (for the numerical simulations) that more accurately resemble those of the normal mode, resulting in a numerical simulation in which the amplitude of all other normal modes is reduced with respect to the previous iteration. Therefore, a repetition of this process leads to successively better approximations to a normal mode and convergence to a prescribed accuracy can be achieved. Since our aim is to test the feasibility of the new method, we keep our model as simple as possible, considering a slab loop model and neglecting the model improvements mentioned above (coronal loop curvature, longitudinal density stratification, magnetic field expansion, …). In the presentation of the iterative method we follow a textbook approach: a simple test case with a known solution is used, approximate solutions are found, the evolution of the error with the iterations is studied, and a proxy for this error that can be used in the stopping criterion is defined in terms of two successive approximations to the solution.

This paper is organized as follows. The equilibrium configuration and the equations for small amplitude perturbations are presented in Section 2. Analytical expressions for the normal modes of this system are introduced in Section 3. The time-dependent equations are solved in Section 4 for a prescribed initial condition and the CEOF analysis is applied to the results of this simulation; hence, the first iteration is complete, which allows us to give an approximation to the normal mode eigenfunctions and eigenfrequency. We next apply repeatedly the last two steps in an iterative process that improves the accuracy of the normal mode approximation (Section 6). Our conclusions are discussed in Section 7.

2. Equilibrium and Zero-β Governing Equations

We use the Cartesian coordinate system shown in Figure 1. The equilibrium is invariant in the y-direction and consists of a dense plasma slab of width $2a$ that extends between $x = -a$ and $x = a$ and is embedded in a rarer environment that fills the space $|x| > a$. The whole system is bounded by the two planes $z = \pm L/2$, with L being the slab length. In the equilibrium the magnetic field is uniform and points in the direction of the slab axis: $\boldsymbol{B}_0 = B_0\hat{\boldsymbol{e}}_z$; in addition, the plasma is at rest. This configuration has been often used to study the oscillations of a coronal loop. The x- and z-coordinates represent the directions transverse and longitudinal to the loop, respectively.

The equilibrium density is expressed as

$$\rho_0(x) = \begin{cases} \rho_i, & |x| \leqslant a, \\ \rho_e, & |x| > a. \end{cases} \tag{1}$$

The internal (i.e., inside the slab) and external Alfvén velocities are

$$v_A(x) = \begin{cases} v_{Ai} \equiv \dfrac{B_0}{\sqrt{\mu\rho_i}}, & |x| \leqslant a, \\ v_{Ae} \equiv \dfrac{B_0}{\sqrt{\mu\rho_e}}, & |x| > a, \end{cases} \tag{2}$$

with μ being the permeability of free space.

We next introduce perturbations whose evolutions are described by the ideal MHD equations; that in the zero-β limit (i.e., zero plasma pressure) and in the absence of gravity read (Priest 2014)

$$\frac{\partial \rho}{\partial t} = -\nabla \cdot (\rho \boldsymbol{V}), \tag{3}$$

$$\rho\frac{\partial \boldsymbol{V}}{\partial t} = -\rho(\boldsymbol{V}\cdot\nabla)\boldsymbol{V} + \frac{1}{\mu}(\nabla \times \boldsymbol{B}) \times \boldsymbol{B}, \tag{4}$$

$$\frac{\partial \boldsymbol{B}}{\partial t} = \nabla \times (\boldsymbol{V} \times \boldsymbol{B}). \tag{5}$$

Here ρ, $\boldsymbol{V}$, and $\boldsymbol{B}$ are the total (equilibrium plus perturbed) density, velocity, and magnetic field. Assuming small amplitude perturbations, Equations (3)–(5) can be linearized. The density perturbation is only present in the first of these equations, so that it is a secondary quantity that can be obtained once the velocity ($\boldsymbol{v}$) and magnetic field ($\boldsymbol{b}$) perturbations are known. The linearized momentum and induction equations can be expressed as follows:

$$\rho_0\frac{\partial \boldsymbol{v}}{\partial t} = \frac{1}{\mu}(\nabla \times \boldsymbol{b}) \times \boldsymbol{B}_0, \tag{6}$$

$$\frac{\partial \boldsymbol{b}}{\partial t} = \nabla \times (\boldsymbol{v} \times \boldsymbol{B}_0), \tag{7}$$

where $\boldsymbol{v}$ and $\boldsymbol{b}$ are both functions of position and time.

Now, perturbations are assumed to propagate in the y-direction with wavenumber k_y, so the y-dependence of $\boldsymbol{v}$ and $\boldsymbol{b}$ is of the form $\exp(-ik_y y)$. The Cartesian components of Equations (6) and (7) then reduce to[4]

$$\frac{\partial v_x}{\partial t} = \frac{B_0}{\mu\rho_0}\left(\frac{\partial b_x}{\partial z} - \frac{\partial b_z}{\partial x}\right), \tag{8}$$

$$\frac{\partial v_y}{\partial t} = \frac{B_0}{\mu\rho_0}\left(\frac{\partial b_y}{\partial z} + ik_y b_z\right), \tag{9}$$

$$\frac{\partial b_x}{\partial t} = B_0\frac{\partial v_x}{\partial z}, \tag{10}$$

$$\frac{\partial b_y}{\partial t} = B_0\frac{\partial v_y}{\partial z}, \tag{11}$$

$$\frac{\partial b_z}{\partial t} = -B_0\left(\frac{\partial v_x}{\partial x} - ik_y v_y\right). \tag{12}$$

[4] The right side of the z-component of Equation (6) is equal to zero, so it leads to $v_z = 0$.

The Astrophysical Journal, 876:86 (12pp), 2019 May 1 Rial et al.

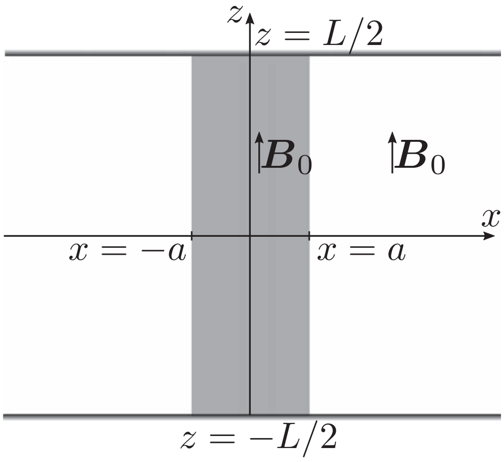

Figure 1. Sketch of the equilibrium configuration, made of a plasma slab (hatched area) of width $2a$, length L, and density ρ_i embedded in an environment with density ρ_e.

The velocity and magnetic field perturbations in these expressions are $\boldsymbol{v}(x, z, t) = v_x(x, z, t)\hat{\boldsymbol{e}}_x + v_y(x, z, t)\hat{\boldsymbol{e}}_y$ and $\boldsymbol{b}(x, z, t) = b_x(x, z, t)\hat{\boldsymbol{e}}_x + b_y(x, z, t)\hat{\boldsymbol{e}}_y + b_z(x, z, t)\hat{\boldsymbol{e}}_z$.

In this paper we impose that the slab has a finite length, L, in the z-direction (Figure 1) and that its ends are line-tied, that is, that the velocity perturbations are zero there. Moreover, in what follows we use the parameter values $\rho_i/\rho_e = 10$, $L = 50a$, and $k_y a = 0.5$. Dimensionless values are obtained with the help of the length a, the velocity v_{Ai}, and the time $\tau_{Ai} = a/v_{Ai}$.

3. Normal Modes

Given that the plasma properties are uniform along the slab, the z-dependence of v_x and v_y is $\cos(k_z z)$. Equations (8)–(12) then reveal that the z-dependence of b_z is $\cos(k_z z)$, while that of b_x and b_y is $\sin(k_z z)$. To satisfy the boundary conditions at the slab ends, k_z must be equal to $(n + 1)\pi/L$, with $n = 0$ for the longitudinally fundamental mode, $n = 1$ for its first longitudinal overtone, etc. To study normal modes, a temporal dependence of the form $\exp(i\omega t)$ is also imposed, so the perturbed velocity and magnetic field components are (the y-dependence is omitted)

$$\begin{aligned} v_x(x, z, t) &= \hat{v}_x(x)\cos(k_z z)e^{i\omega t},\\ v_y(x, z, t) &= \hat{v}_y(x)\cos(k_z z)e^{i\omega t}, \end{aligned} \tag{13}$$

$$\begin{aligned} b_x(x, z, t) &= \hat{b}_x(x)\sin(k_z z)e^{i\omega t},\\ b_y(x, z, t) &= \hat{b}_y(x)\sin(k_z z)e^{i\omega t}, \end{aligned} \tag{14}$$

$$b_z(x, z, t) = \hat{b}_z(x)\cos(k_z z)e^{i\omega t}. \tag{15}$$

Equations (8)–(12) now reduce to

$$\omega\hat{v}_x = -\frac{B_0}{\mu\rho_0}\left[k_z(i\hat{b}_x) - \frac{d}{dx}(i\hat{b}_z)\right], \tag{16}$$

$$\omega(i\hat{v}_y) = \frac{B_0}{\mu\rho_0}[k_z\hat{b}_y + k_y(i\hat{b}_z)], \tag{17}$$

$$\omega(i\hat{b}_x) = -B_0 k_z\hat{v}_x, \tag{18}$$

$$\omega\hat{b}_y = B_0 k_z(i\hat{v}_y), \tag{19}$$

$$\omega(i\hat{b}_z) = -B_0\left[\frac{d\hat{v}_x}{dx} - k_y(i\hat{v}_y)\right]. \tag{20}$$

Now, the problem is to compute the x-dependence of the eigenfunctions $\hat{v}_x$, $i\hat{v}_y$, $i\hat{b}_x$, $\hat{b}_y$, and $i\hat{b}_z$, which are all real, and the eigenvalue ω.

It is straightforward to eliminate all variables in favor of $\hat{v}_x$, which leads to the following ordinary differential equation,

$$\frac{d^2\hat{v}_x}{dx^2} = m^2\hat{v}_x, \tag{21}$$

with

$$m^2 = k_y^2 + k_z^2 - \frac{\omega^2}{v_A^2}. \tag{22}$$

The parameter m takes the value $m_{i,e}$ when the Alfvén speed is substituted by its value $v_{Ai,e}$ inside and outside the slab, respectively. After determining $\hat{v}_x$ one can obtain $i\hat{v}_y$ and $i\hat{b}_z$ from

$$i\hat{v}_y = \frac{k_y}{m^2}\frac{d\hat{v}_x}{dx}, \tag{23}$$

$$\frac{i\hat{b}_z}{B_0} = -\frac{1}{\omega}\frac{\kappa^2}{m^2}\frac{d\hat{v}_x}{dx}, \tag{24}$$

where

$$\kappa^2 = k_z^2 - \frac{\omega^2}{v_A^2} \equiv m^2 - k_y^2. \tag{25}$$

Again, κ takes the values $\kappa_{i,e}$ inside and outside the slab, respectively. The eigenfunctions $i\hat{b}_x$ and $\hat{b}_y$ follow from Equations (18) and (19), and are just proportional to $\hat{v}_x$ and $i\hat{v}_y$, respectively.

To solve Equation (21) one must impose boundary conditions in the x-direction, together with the proper jump conditions at the $x = \pm a$ interfaces, which, according to, e.g., Goedbloed & Poedts (2004), are the continuity of the normal velocity component ($\hat{v}_x$) and of the total pressure, which in turn leads to the continuity of $i\hat{b}_z$.

Because of the symmetry[5] of the equilibrium and of Equations (16)–(20) with respect to $x = 0$, eigenfunctions are either even or odd. For kink modes $\hat{v}_x$ and $i\hat{b}_x$ are even about the slab axis, while $i\hat{v}_y$, $\hat{b}_y$, and $i\hat{b}_z$ are odd; for sausage modes, the parity of the five eigenfunctions is the opposite. In our simulations only kink solutions are excited, so we restrict our analysis to these normal modes.

3.1. Laterally Evanescent Normal Modes

Arregui et al. (2007) solved the eigenproblem of Equations (16)–(20) for solutions that are laterally evanescent, that is, for which the perturbations vanish as $x \to \pm\infty$; see their Section 3 and also Roberts (1981) for the treatment of the $k_y = 0$ case. The kink solution that satisfies these constraints has the following x-velocity component:

$$\hat{v}_x(x) = \begin{cases} C\exp(m_e x), & \text{for } x < -a,\\ A\cosh(m_i x), & \text{for } -a \leqslant x \leqslant a,\\ C\exp(-m_e x), & \text{for } x > a, \end{cases} \tag{26}$$

[5] The imposed boundary conditions in the x-direction are also symmetric: see Sections 3.1 and 3.2.

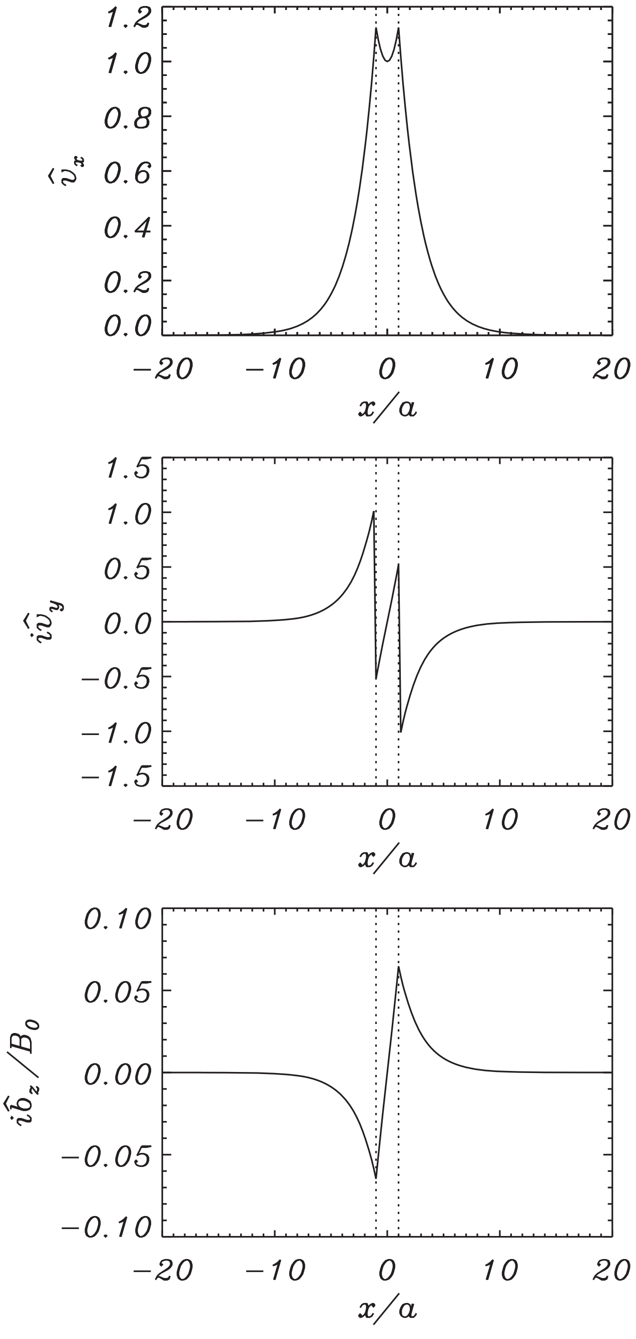

Figure 2. Normal mode: from top to bottom, eigenfunctions $\hat{v}_x$, $i\hat{v}_y$, and $i\hat{b}_z$ for the fundamental evanescent kink mode. The two dotted lines correspond to the slab boundaries.

where the positive value of m_e is taken and

$$C = A\exp(m_e a)\cosh(m_i a). \tag{27}$$

The constant A can be arbitrarily chosen, so we set $A = 1$. The eigenfrequency is the solution to the dispersion relation

$$\tanh(m_i a) = -\frac{\kappa_e^2}{\kappa_i^2}\frac{m_i}{m_e}. \tag{28}$$

Figure 2 displays the eigenfunctions $\hat{v}_x$, $i\hat{v}_y$, and $i\hat{b}_z$ for the fundamental kink mode. They possess the parity and continuity properties described above: $\hat{v}_x$ is even, $i\hat{v}_y$ and $i\hat{b}_z$ are odd, and $\hat{v}_x$ and $i\hat{b}_z$ are continuous at the interfaces $x = \pm a$. On the other hand, $i\hat{v}_y$ jumps abruptly at these boundaries. In addition, these functions decay exponentially with x, as described by Equation (26). The longitudinal harmonics have a similar spatial structure of eigenfunctions. The frequencies for the $n = 0, 2, 4$ longitudinal harmonics are $\omega/\tau_{Ai} = 0.1011, 0.2989, 0.4852$.

3.2. Laterally Confined Normal Modes

In Section 4 we solve numerically the initial value problem made of Equations (8)–(12) with suitable initial and boundary conditions. We consider the spatial domain $-20a \leqslant x \leqslant 20a$. Given that the boundaries are sufficiently far from the slab, the evanescent eigensolution of Figure 2 is almost zero at the edges of the numerical domain, so it is, in practice, a solution to the initial value problem. Placing the boundaries at a finite distance from the slab, however, adds new, non-evanescent eigensolutions that can be excited by the initial perturbation. By replicating the analysis of Section 3.1 with the boundary condition $\hat{v}_x = 0$ at $x = \pm L_x$ the laterally confined eigenfunctions can be obtained. It will suffice to say that the fundamental confined mode has $\omega = 1.676/\tau_{Ai}$.

4. Time-dependent Numerical Simulations

4.1. Simulation Setup and Numerical Method

We now solve numerically Equations (8)–(12) in the region $-L_x \leqslant x \leqslant L_x$, $-L/2 \leqslant z \leqslant L/2$; see Figure 1. The coefficients of the system of partial differential equations can be made real using the independent variables v_x, iv_y, b_x, ib_y, and b_z. Our initial disturbance is such that the full slab is subject to an initial transverse forcing given by

$$v_x(x, z, t = 0) = v_0 \exp\left(-\frac{x^2}{a^2}\right)\exp\left(-\frac{z^2}{a^2}\right), \tag{29}$$

while all other variables are initially zero. This initial perturbation represents a sudden deposition of energy at the slab center. The v_x perturbation is even about $x = 0$ and so can only excite kink modes. Since the transverse profile of v_x resembles that of the laterally evanescent kink modes (top panel of Figure 2), a large portion of the energy in the initial disturbance will go to these modes. But one can expect that the laterally confined mode of Section 3.2 will also be excited.

The simulation box is determined by the lengths $L_x = 20a$ and $L = 50a$, and a uniform grid of 4001 × 51 points in the x- and z-directions is used. The grid is coarser along the slab because it is sufficient to capture well the smooth sinusoidal dependence of normal modes in the z-direction; on the other hand, the grid is much finer across the slab because normal modes have much more structure in this direction. The numerical simulation is stopped at $t \simeq 280\tau_{Ai}$, which is ~4.5 and ~75 periods of the fundamental laterally evanescent and confined modes, respectively. The time step is $\Delta t = 0.704\tau_{Ai}$.

The numerical method used to solve the linearized wave equations is based on the method of lines. Time and space are treated independently, using a third-order Runge–Kutta method and a six-order finite difference method, respectively. Artificial dissipation is included to avoid oscillations on the grid scale. This method has been used successfully in the past (e.g., Bona et al. 2009) and has a weak effect on the attenuation of the physical oscillations reported in the simulations. Since the linear hyperbolic MHD equations are solved explicitly, the time step is subject to the CFL condition. Note that in the linearized MHD equations there are terms proportional to k_y: these terms are incorporated to the code as simple source terms.

Although we solve the linearized MHD equations, there are jumps in the perturbed variables (in iv_y and b_y) due to the discontinuities in the equilibrium variables. We have decided to use a simple numerical scheme that is not shock-capturing (better suited for discontinuities) because the effect of the jump is rather small in the temporal evolution of the different quantities.

Line-tying conditions are applied at $z = \pm L/2$, meaning that the velocities are zero, while for the rest of variables the derivatives with respect to z are zero. At $x = \pm L_x$ we impose that the derivatives with respect to x of all the variables are zero. This condition does not allow a perfect outward transmission of the waves and some reflections are produced. A direct consequence of these reflections is the presence of the laterally confined normal mode in our simulations.

4.2. Results

The initial condition excites a large number of longitudinal harmonics, both evanescent and confined in the x-direction, together with leaky waves that travel away from the slab. The emission of these leaky waves is clear until $t \simeq 50\tau_{Ai}$, after which only the kink normal modes of Sections 3.1 and 3.2 remain. Evidence of the presence of these normal modes comes from the spectral analysis of v_x, iv_y, and b_z at a given location, which is selected so that normal modes have a non-negligible amplitude. Thus, for the transverse velocity component, v_x, we choose the point $x = 0$, $z = 0$, while for the other two variables the position $x = a$, $z = 0$ is preferred. The Lomb–Scargle periodograms (Lomb 1976; Scargle 1982) at these points are shown in Figure 3. The three panels display the largest power peaks at $\nu = 0.01601/\tau_{Ai}$ (i.e., $\omega = 0.1006/\tau_{Ai}$), $\nu = 0.04721/\tau_{Ai}$ ($\omega = 0.2966/\tau_{Ai}$), and $\nu = 0.07681/\tau_{Ai}$ ($\omega = 0.4826/\tau_{Ai}$); these values are in excellent agreement with those of the lowest three laterally evanescent harmonics. The periodograms also show large power above $\nu = 0.2/\tau_{Ai}$ caused by the excitation of laterally confined normal modes. Indeed, the largest peak in this frequency range is at $\nu = 0.2544/\tau_{Ai}$ (i.e., $\omega = 1.598/\tau_{Ai}$), again in good agreement with the value quoted in Section 3.2. It is worth noting that the power at $\omega = 0.1011/\tau_{Ai}$ is 2–3 orders of magnitude higher than that at $\omega = 1.676/\tau_{Ai}$ for v_x and iv_y, although in the case of b_z the two peaks are of similar magnitude. The reason for this is that the height of a power peak comes from the combination of the energy deposited by the initial disturbance in each normal mode (which is much larger for the evanescent one) and the amplitude of each variable (which in the case of b_z is much smaller for the evanescent normal mode than for the confined one). The combination of these two factors results in the function b_z containing similar power in the evanescent and confined normal modes in this numerical simulation.

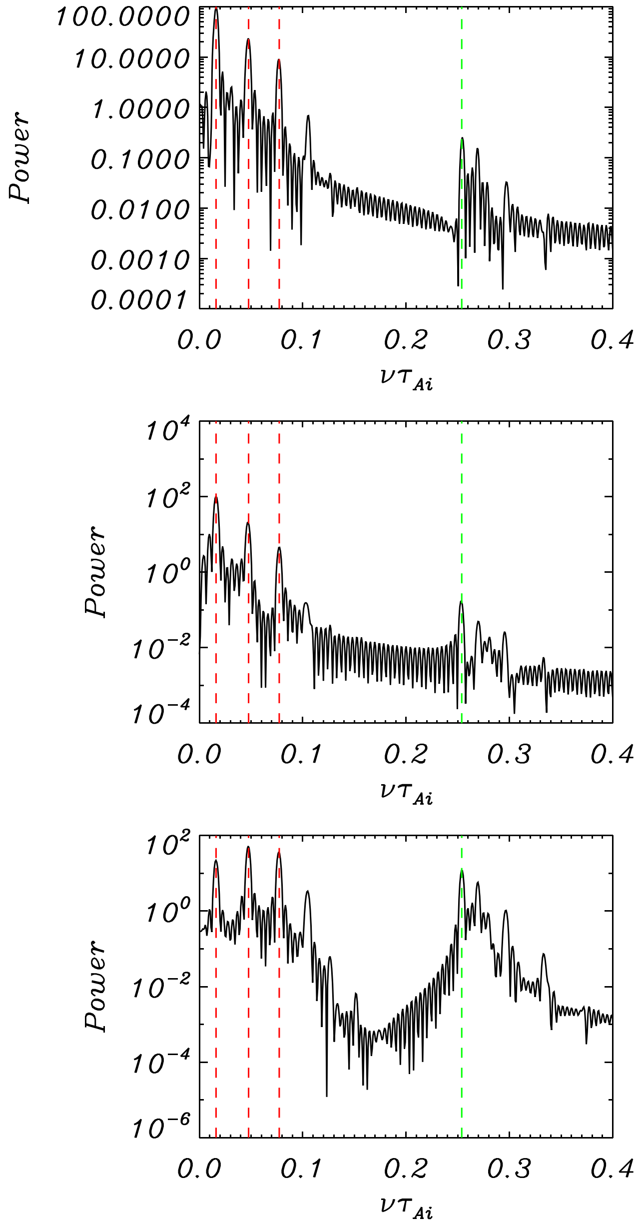

Figure 3. Numerical simulation: Lomb–Scargle periodogram of v_x at position $x = 0$, $z = 0$ (top), iv_y at position $x = a$, $z = 0$ (middle), and b_z at position $x = a$, $z = 0$ (bottom). To compute the power spectra, only data for $t \geqslant 50\tau_{Ai}$ are kept so as to remove the effect of the transient in the frequency estimation. Vertical red (green) lines are drawn at the frequencies of the first laterally evanescent (laterally confined) harmonics.

5. CEOF Analysis

In this section we go beyond the normal mode frequency we just obtained and attempt to determine the normal mode eigenfunction structure using the CEOF analysis. We will here give a very brief summary of this method; a detailed description can be found in Horel (1984), Wallace & Dickinson (1972), von Storch & Zwiers (1999), and Hannachi et al. (2007; where it is called Complex Hilbert EOF); and an application to the study of coronal oscillations in Terradas et al. (2004).

The CEOF analysis is a numerical method that takes as its input a field $U(\boldsymbol{r}, t_l)$ discretized over a spatial mesh of points $\boldsymbol{r} = (x_i, y_j, z_k)$ and evaluated at the discrete times t_l. Its output is a set of CEOF modes, which are not necessarily associated with physical modes of the system under study, each of them described by four measures called the temporal amplitude and phase and the spatial amplitude and phase. Together with these measures, the CEOF analysis associates with each mode a fraction of the total field variance. Once the CEOF code is fed

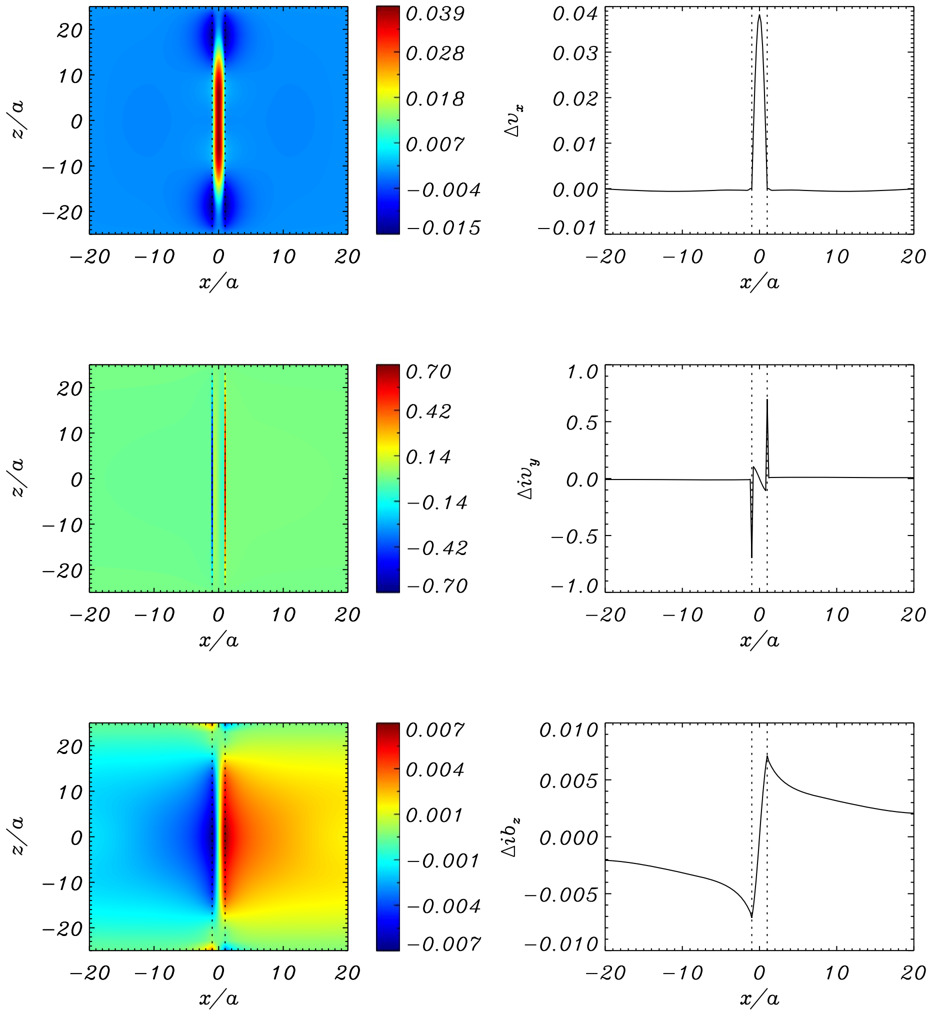

Figure 4. CEOF analysis: difference Δv_x (top row), Δv_y (middle row), and Δb_z (bottom row) between the fundamental evanescent eigenfunctions and their approximations from the first CEOF mode. Left: two-dimensional distribution of the difference. Right: cut of the difference along $z = 0$. Dotted lines are plotted at the slab boundaries.

with the input field, the "highest contributing" CEOF mode, that is, the one associated to the largest fraction of the total field variance, is retrieved first and other CEOF modes are obtained next in decreasing order of their fraction of the total field variance. The sum of the modes' fraction of the total field variance tends to 1 as the number of CEOF modes is increased. The execution is stopped when the percentage of the total field variance accounted for by all the retrieved CEOF modes exceeds a pre-established value, here taken as 99.9%.

In our case the field U can be, for example, the velocity component $v_x(x_i, z_k, t_l)$ obtained in the numerical simulation of Section 4. This means that the input field is a three-dimensional data cube. As mentioned above, each of the obtained CEOF modes has empirically computed temporal and spatial measures, called the temporal amplitude, $R(t_l)$, the temporal phase, $\phi(t_l)$, the spatial amplitude, $S(x_i, z_k)$, and the spatial phase, $\theta(x_i, z_k)$. The spatial and temporal variability of the field described by this CEOF mode is

$$\mathrm{Re}\,\{R(t_l)\exp[i\phi(t_l)]S(x_i, z_k)\exp[-i\theta(x_i, z_k)]\}, \tag{30}$$

where Re denotes the real part. A CEOF mode that, for example, represents a propagating wave, has a temporal phase that varies linearly with t_l and a spatial phase that varies linearly with x_i and z_k. The CEOF modes that we expect to find when analyzing the results of the numerical simulation, however, are standing waves. In this case, the temporal phase also varies linearly with t_l, but the spatial phase is such that two regions in which the difference of $\theta(x_i, z_k)$ is an integer multiple of 2π correspond to in-phase oscillations, while oscillations that are in anti-phase display a phase difference that is an odd multiple of π. In our results we will also find that a standing wave can have a phase that slowly varies in space, which is nothing but a modulation of $S(x_i, z_k)$ by the factor $\exp[-i\theta(x_i, z_k)]$. Section 3 of Terradas et al. (2004) gives simple two-dimensional examples of the outcome of the CEOF analysis when applied to a synthetic signal made of the sum of a propagating and a standing wave.

Our hypothesis is that the CEOF analysis applied to the results of the numerical simulation of Section 4 will provide an approximation, by means of Equation (30), to the evanescent normal mode eigenfunctions. Given that the eigenfunctions do not depend on time, we will ignore the temporal variation given by the measures $R(t)$ and $\phi(t)$ in Equation (30) and will only

The Astrophysical Journal, 876:86 (12pp), 2019 May 1 Rial et al.

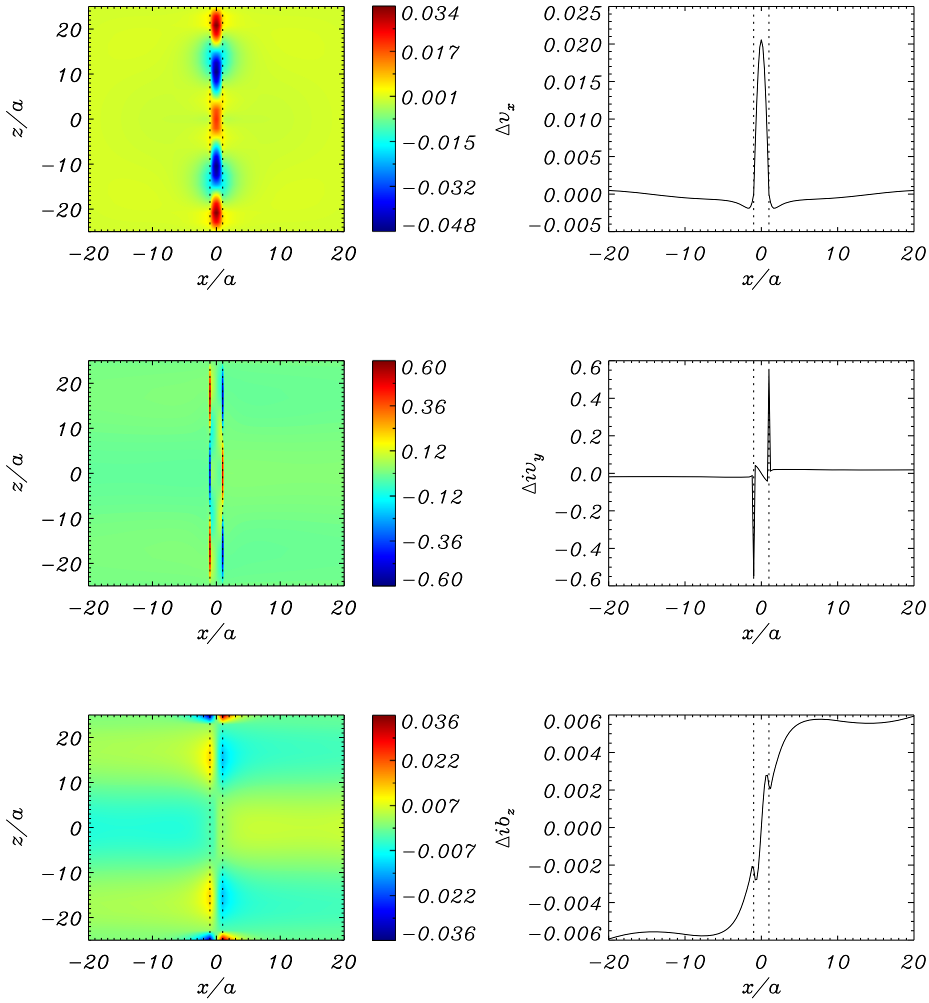

Figure 5. CEOF analysis: same as Figure 4, but for the second longitudinal evanescent overtone.

retain the real part of the spatial measures. Let us take, for example, the variable v_x, which for a normal mode has the eigenfunction $\hat{v}_x(x)\cos(k_z z)$. The CEOF approximation to this eigenfunction is

$$\tilde{v}_x(x_i, z_k) = S_{v_x}(x_i, z_k)\cos\theta_{v_x}(x_i, z_k), \tag{31}$$

where S_{v_x} and θ_{v_x} are the spatial amplitude and phase of v_x and the tilde in $\tilde{v}_x$ indicates that this is an approximation to the normal mode v_x. A numerical comparison between the normal mode eigenfunction and its approximation from the CEOF analysis is obtained with the help of the difference

$$\Delta v_x(x_i, z_k) = \hat{v}_x(x_i)\cos k_z z_k - \tilde{v}_x(x_i, z_k). \tag{32}$$

An analogous expression can be built for all other eigenfunctions.

Regarding iv_y, its eigenfunction for the confined mode is $i\hat{v}_y(x)\cos(k_z z)$, with $i\hat{v}_y(x)$ given by Equations (23) and (26). The CEOF approximation to this eigenfunction is

$$i\tilde{v}_y(x_i, z_k) = S_{iv_y}(x_i, z_k)\cos\theta_{iv_y}(x_i, z_k), \tag{33}$$

with S_{iv_y} and θ_{iv_y} being the spatial amplitude and phase of iv_y. The case of b_z requires special attention. Its eigenfunction is $i\hat{b}_z(x)\cos(k_z z)$, where $i\hat{b}_z(x)$ can be obtained from Equations (24) and (26). In the numerical simulation, however, we have not used the variable ib_z but b_z. For this reason, the CEOF approximation to ib_z requires inserting a factor i inside Re{…} of Equation (30). We then have that the CEOF approximation to ib_z is

$$i\tilde{b}_z(x_i, z_k) = S_{b_z}(x_i, z_k)\sin\theta_{b_z}(x_i, z_k), \tag{34}$$

where S_{b_z} and θ_{b_z} are the spatial amplitude and phase of b_z. Concerning b_x and b_y, Equations (18) and (19) tell us that their respective CEOF approximations can be obtained from those of v_x and iv_y. Finally, approximations to $\hat{v}_x(x)$, $i\hat{v}_y(x)$, and $i\hat{b}_z(x)$ can be derived by taking a cut along $z = z_k$ of Equations (31), (33), and (34).

Before applying the CEOF method to the results of our simulation, two more comments are in order. First, the transient phase is excluded from the analysis by considering $t \geqslant 50\tau_{Ai}$ only. Second, to reduce the memory requirements and speed up the computation of the CEOF modes, the values of v_x, iv_y, and b_z are interpolated from the 4001×51 numerical grid to a grid of $N_x \times N_z$ points (here we use $N_x = 201$, $N_z = 25$). To do so, in the x- and z-directions only 1 of every 20 points and 1 of every 2 points, respectively, from the numerical simulation are kept for the CEOF analysis.

The Astrophysical Journal, 876:86 (12pp), 2019 May 1 Rial et al.

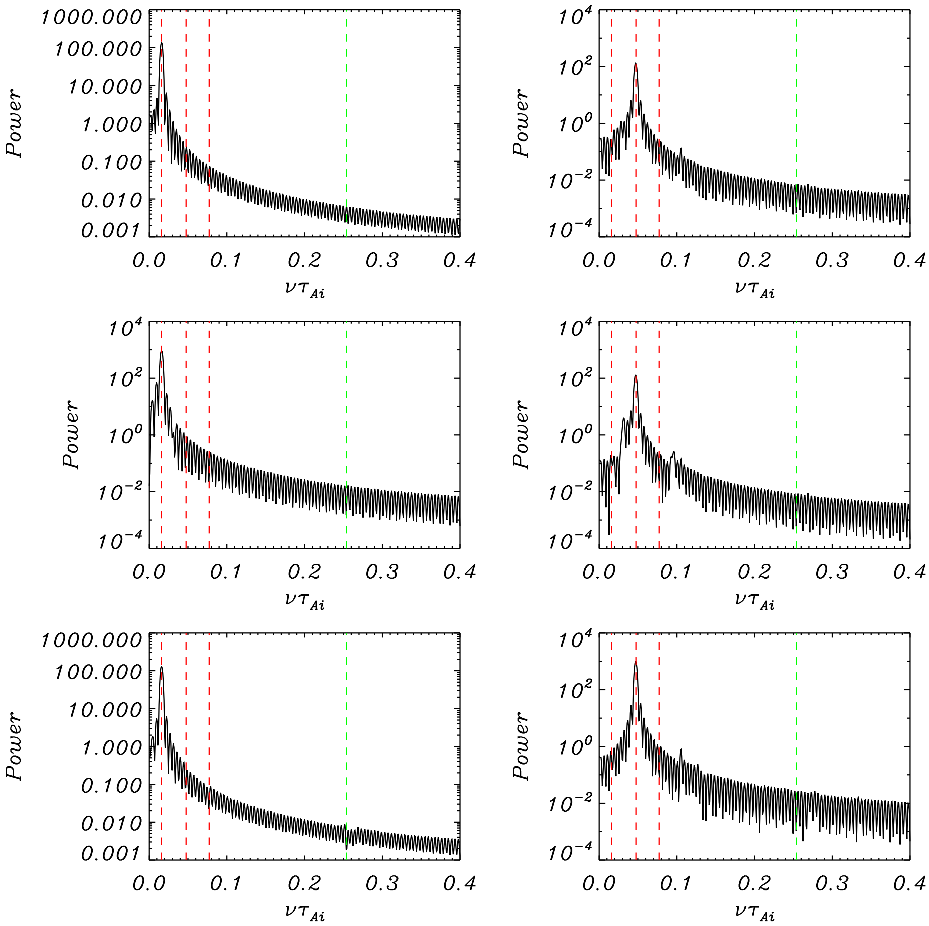

Figure 6. Iterative method: same as Figure 3, but for the numerical simulations of iteration #6. Left: fundamental evanescent mode. Right: second longitudinal evanescent overtone.

5.1. Results

The CEOF method has the possibility of analyzing several fields simultaneously, which allows a better characterization of the physical modes because more restrictions are imposed by the higher complexity of the combined fields. Thus, we run the CEOF code on the fields $v_x(x_i, z_k, t_l)$, $iv_y(x_i, z_k, t_l)$, and $b_z(x_i, z_k, t_l)$ together. To do this, the three data cubes are put next to each other and a larger data cube is created. We choose to join the three $201 \times 25 \times 330$ cubes by attaching their xt-faces, so that the CEOF input is a cube of $201 \times 75 \times 330$ data values. After the CEOF analysis is complete, we obtain a collection of CEOF modes, each of them characterized by its temporal amplitude and phase, $R(t)$ and $\phi(t)$, and its spatial amplitude and phase, $S(x, z)$ and $\theta(x, z)$, that can be split into the spatial measures S_{v_x} and θ_{v_x} of the field $v_x(x_i, z_k, t_l)$, S_{iv_y} and θ_{iv_y} of the field $iv_y(x_i, z_k, t_l)$, and S_{b_z} and θ_{b_z} of the field $b_z(x_i, z_k, t_l)$. These measures can in turn be inserted into Equations (31), (33), (34) to obtain the approximate CEOF eigenfunctions.

The first CEOF mode accounts for 64.8% of the total field variance and corresponds to the fundamental evanescent normal mode. Its frequency is determined by fitting the straight line $\phi(t) = \omega t + \phi_0$ to the temporal phase, which yields $\omega = 0.1016/\tau_{Ai}$. This value is in excellent agreement with the normal mode frequency $\omega = 0.1011/\tau_{Ai}$. The goodness of the CEOF approximation to the normal mode can also be judged with the help of the differences Δv_x, Δv_y, Δb_z, which are presented in Figure 4. To make this figure, the $\hat{v}_x$ eigenfunction is normalized to a maximum value of 1 and the CEOF approximation $\tilde{v}_x$ is also normalized to 1 at the position where the eigenfunction is maximum. The conclusion from this figure is that the CEOF analysis of the numerical simulation results allows us to recover the normal mode eigenfunction $\hat{v}_x$ with an error below 4%. We next turn our attention to the error of iv_y and ib_z. The middle row of Figure 4 gives the difference Δv_y. Except for the points on the boundaries, $x = \pm a$, the error is smaller than 10% inside the slab ($|x| < a$) and practically zero outside the slab ($|x| > a$). The bottom row of Figure 4 gives the difference Δb_z, which also attains its largest value, of the order of 15% of the eigenfunction value, at the slab boundary.

The second CEOF mode accounts for 15.9% of the total field variance and corresponds to the second longitudinal evanescent overtone. A linear fit to the temporal phase results in the frequency $\omega = 0.2969/\tau_{Ai}$, which is very close to the analytical value $\omega = 0.2989/\tau_{Ai}$. Figure 5 shows the difference between the normal mode and the CEOF approximation to the eigenfunctions. We see that the error in the second longitudinal overtone is almost a factor of 2 better than that of the fundamental mode. When comparing the exactness of the CEOF approximation for the fundamental and the second overtone, we find a better agreement in the second case because there are more periods of this normal mode in the numerical simulation.

The Astrophysical Journal, 876:86 (12pp), 2019 May 1

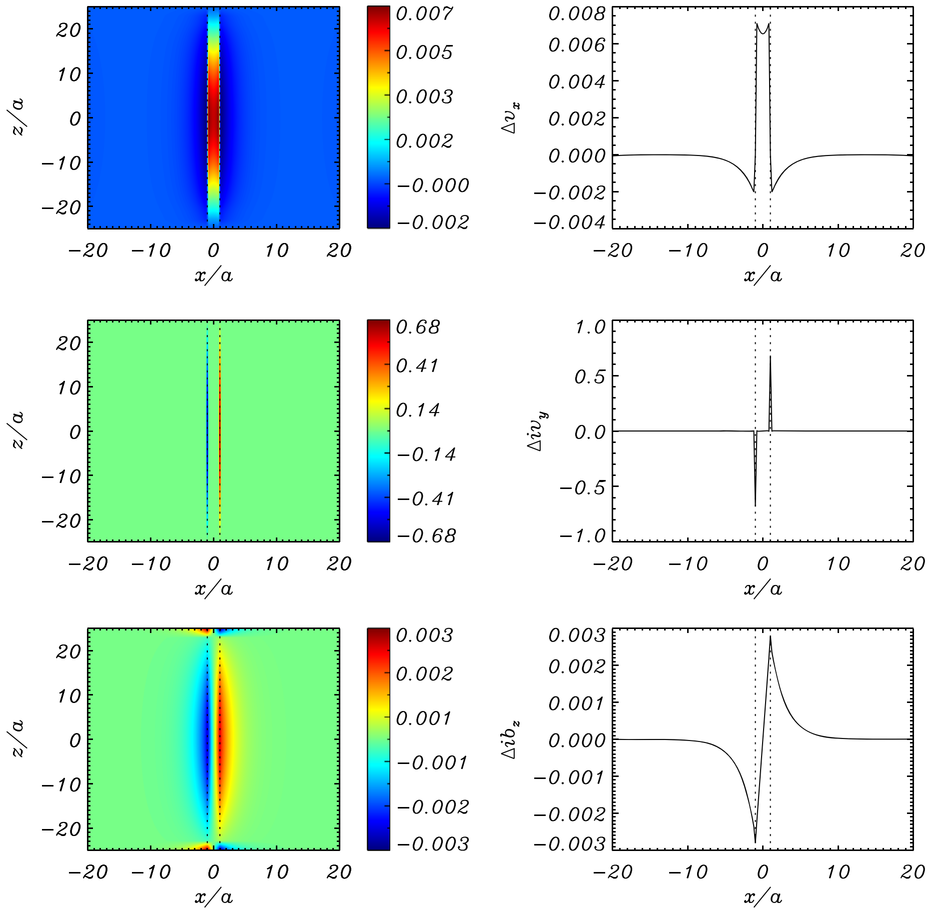

Figure 7. Same as Figure 4, but for the CEOF analysis of iteration #6.

The conclusion of this section is that, while the CEOF approximation to $\hat{v}_x$ is acceptable, those to $i\hat{v}_y$ and $i\hat{b}_z$ are not too good. This situation will be improved by the application of the iterative method presented in the following section.

6. Iterative Method

6.1. Description of the Method

The scheme we have used so far consists of two steps: (i) a time-dependent numerical simulation of Equations (8)–(12) followed by (ii) the CEOF analysis of the obtained results. If we imagine that an eigenmode is perfectly described by a CEOF mode, then one could run a numerical simulation with initial conditions given by the eigenfunctions and thus the obtained temporal evolution would be that of the eigenmode. At this point, this is not the case, but we have seen that the CEOF analysis produces an approximation to a normal mode eigenfunctions. We thus devise an iterative method that is made of the repeated application of steps (i) and (ii), in which the initial conditions of the numerical simulation of a given iteration are taken from the CEOF method of the previous iteration. The iterations will be stopped once a given measure of goodness is reached. The iterative method is carried out separately for each normal mode.

We first need to determine which information is required from the CEOF analysis to fix the initial conditions. Rather than using the time dependence $\exp(i\omega t)$ of Equations (13)–(15) we assume that $v_x(x, z, t)$ is maximum at $t = 0$ and so it has the form $v_x(x, z, t) = \hat{v}_x(x)\cos(k_z z)\cos(\omega t)$. Now, Equations (8)–(12) tell us that v_x and iv_y are in phase (in time) and that they are a quarter of a period out of phase with respect to b_x, ib_y, and b_z. This implies that $iv_y(x, z, t)$ is also maximum at $t = 0$ and that the perturbed magnetic field components vanish at the start of the numerical simulation. Hence, the information that the CEOF analysis must provide to repeat step (i) is the approximation to $\hat{v}_x$ and $i\hat{v}_y$ provided by Equations (31) and (33).

6.2. Results

We are then ready to carry out the iterative process. Iteration #1 consists of the numerical simulation of Section 4 and the CEOF analysis of Section 5.1. The results we present now are a summary of the performance of six iterations, which are carried out independently for the fundamental evanescent mode and its second longitudinal overtone. An excellent assessment of the performance of the iterative method can be gained from the power spectra of v_x, iv_y, and b_z for the numerical simulation of the last iteration. These power spectra are shown in Figure 6 for the two normal modes. Whereas the numerical simulation of iteration #1 displays power peaks at the frequencies of many harmonics, both simulations of iteration #6 only show a power peak for a single normal mode. The left (right) panels of Figure 6 have non-negligible power around the maximum $\nu = 0.01601/\tau_{Ai}$ ($\nu = 0.04721/\tau_{Ai}$) that are identical to those obtained from the power spectra in the first iteration. All other normal modes are virtually absent in the numerical simulations of the last iteration.

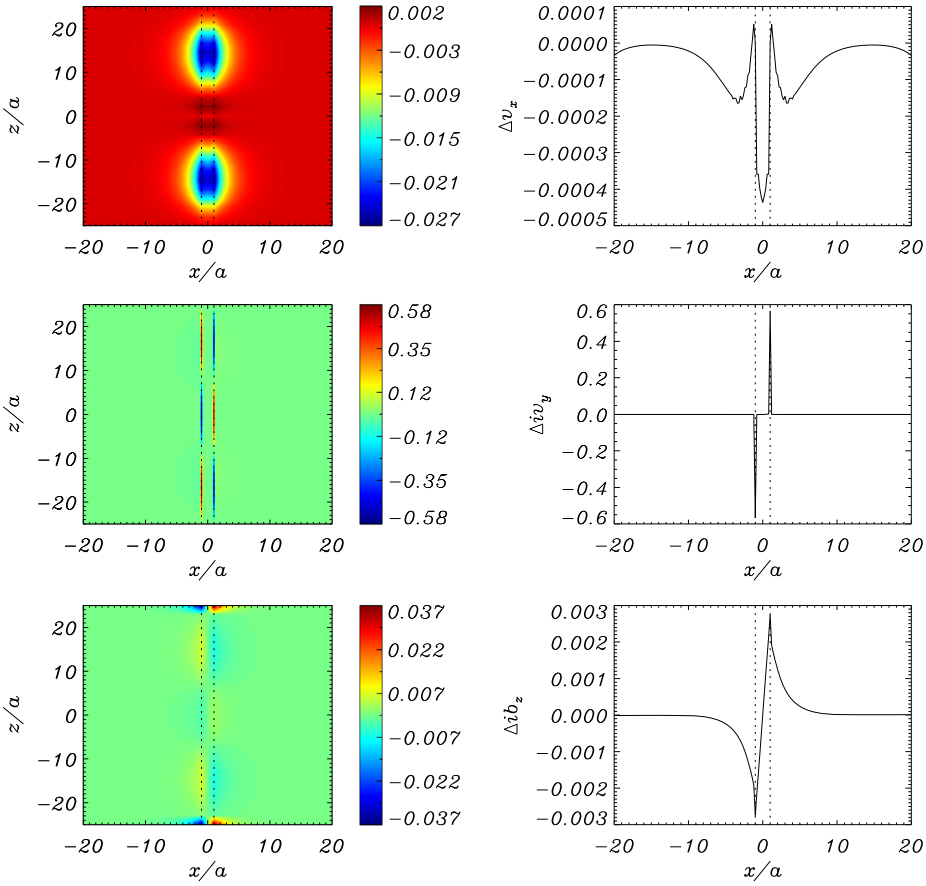

Figure 8. Same as Figure 5, but for the CEOF analysis of iteration #6.

The iterative method yields another approximation to the frequency that comes from the CEOF analysis of the numerical simulation of iteration #6. A linear least-squares fit to the temporal phase gives the frequency $\omega = 0.1016/\tau_{Ai}$ for the fundamental evanescent mode and $\omega = 0.2969/\tau_{Ai}$ for the second longitudinal evanescent overtone. These values are identical to those of the first iteration. The errors associated with these approximate values are 0.5% and 0.7%, so the obtained accuracy is excellent.

6.3. Error and Stopping Criterion

We next examine in detail the error of the CEOF approximation to the eigenfunctions. Again, we consider the results of iteration #6 and show these errors in Figures 7 and 8. Although their maximum values are reduced by a factor of 2, the errors display some of the patterns of iteration #1: the error of v_x is maximum in the slab; the error of iv_y has a dominant component at the slab boundaries, but has been strongly reduced inside the slab during the iterative process; and the error of b_z is maximum at the slab boundaries, but has become much more confined to the slab neighborhood.

We finally analyze the evolution of the error with the iterations.[6] At the end of iteration #n, with $n = 1, 2, \ldots$, Equations (31), (33), and (34) provide us with approximations for the three main eigenfunctions; we denote these approximations with the superscript n, i.e., $\tilde{v}_x^n$, $i\tilde{v}_y^n$, $i\tilde{b}_z^n$. For each eigenfunction, we define a global measure of the error, ε, by summing over the spatial domain the squares of the difference between the normal mode eigenfunction and the CEOF approximation. For example, for iteration #n and the variable v_x this global error is

$$\varepsilon_{v_x}^n = \frac{1}{N_x N_z \max\limits_{i,k} |\hat{v}_x(x_i) \cos k_z z_k|} \times \left\{ \sum_{i,k} [\hat{v}_x(x_i) \cos k_z z_k - \tilde{v}_x^n(x_i, z_k)]^2 \right\}^{1/2}, \quad n = 1, 2, \ldots, \tag{35}$$

where the factor $\max_{i,k} |\hat{v}_x(x_i) \cos k_z z_k|$ in the denominator provides the right normalization that enables us to compare the error of different eigenfunctions. The additional factors N_x and N_z give an additional normalization that removes the dependence of $\varepsilon_{v_x}^n$ on the number of points in the CEOF analysis. The definitions of $\varepsilon_{iv_y}^n$ and $\varepsilon_{ib_z}^n$ are done in a similar way.

The top panels of Figure 9 present the global errors for the first 6 iterations for the fundamental evanescent mode (left column) and its second longitudinal overtone (right column). In each iteration, v_x has the smallest error (possibly because it is the eigenfunction with less "contamination" from the confined normal mode) and iv_y displays the largest global error (because

[6] Before computing the errors described here we normalize the normal mode eigenfunctions and their approximation from the CEOF analysis so that v_x equals zero at $x = 0$, $z = 0$.

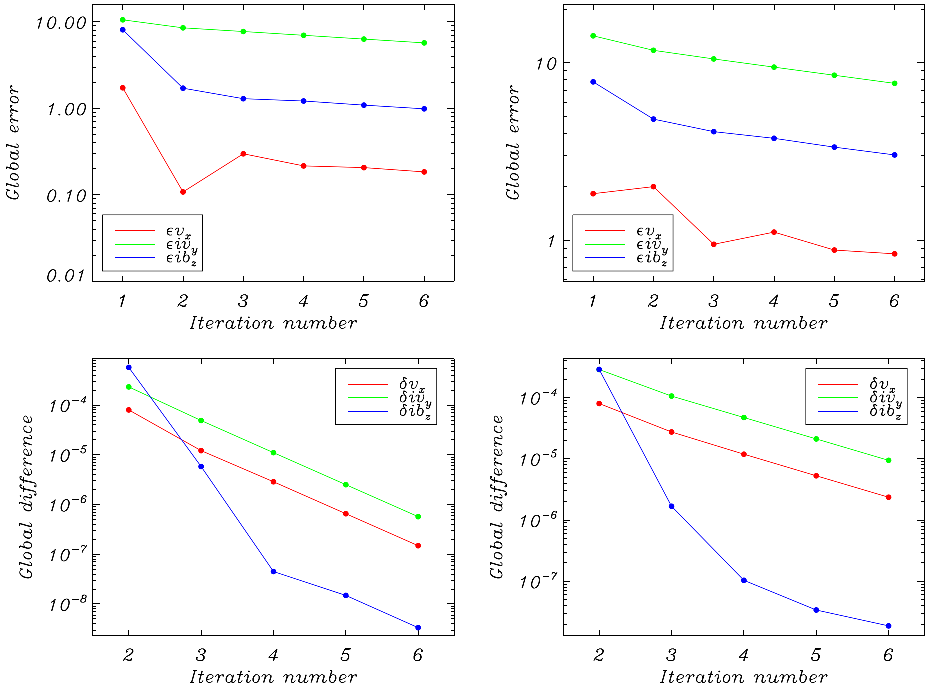

Figure 9. Global error (top panels) and global difference (bottom panels) as a function of the iteration number. Left: fundamental evanescent mode. Right: second longitudinal evanescent overtone.

of the large contributions at the slab boundaries, that do not disappear with the iterative process). We see that the biggest improvement in the global error is obtained in iteration #2, for which a remarkable reduction in ε_{v_x} and ε_{ib_z} is found. The subsequent variation of the three global errors is much more moderate, so for this problem two iterations give a good compromise between the error associated with the CEOF approximations and the computer time spent.

The case studied in this paper allows us to compute the global error because of our knowledge of the exact eigenfunctions. In a general case, in which the eigenfunctions are unknown and our aim is just to obtain them, a proxy for the global error can be computed by comparing the approximate eigenfunctions of two successive iterations. To define this new global uncertainty measure, in Equation (35) we replace the normal mode eigenfunction $\hat{v}_x(x_i)\cos k_z z_k$ with its CEOF approximation in the iteration $n+1$. We also rewrite the iteration indices and substitute $n+1$ by n. This gives the following definition for the global difference between the v_x eigenfunction of iterations $\#n$ and $\#n-1$:

$$\delta_{v_x}^n = \frac{1}{N_x N_z \max\limits_{i,k}|\tilde{v}_x^n(x_i, z_k)|} \times \left\{\sum_{i,k}[\tilde{v}_x^n(x_i, z_k) - \tilde{v}_x^{n-1}(x_i, z_k)]^2\right\}^{1/2}, \quad n = 2, 3, \ldots. \tag{36}$$

Analogous expressions can be written for δ_{iv_y} and δ_{ib_z}.

The variation of the global difference with the iterations is displayed in the bottom panels of Figure 9. The convergence is quite fast, with δ_{ib_z} showing an improvement of roughly two orders of magnitude per iteration during the first iterations, the highest convergence rate of all variables. δ_{v_x} and δ_{iv_y} are reduced at a slower pace, namely almost an order of magnitude per iteration. We see that all variables attain a global difference smaller than 10^{-5} in iteration #5 (fundamental evanescent mode) and in iteration #6 (second longitudinal evanescent overtone). Therefore, we adopt the iteration stopping criterion that the global difference must be smaller than 10^{-5}.

7. Conclusions

In this paper we have devised a method to determine the normal modes of a physical system, i.e., its eigenfunctions and eigenfrequencies, by the iterative application of time-dependent numerical simulations of the equations that govern the system dynamics and the CEOF analysis of the simulation results. We have illustrated how the CEOF method can be applied to all the non-redundant variables: in our case, in particular, this means that we can avoid including b_x and ib_y in the CEOF computation because their eigenfunctions can be readily computed from the other three (v_x, iv_y, and b_z). At the end of each iteration, the CEOF approximations to the eigenfunctions are used as the initial conditions for the time-dependent numerical simulation of the next iteration. Finally, we have examined the global error of the approximate eigenfunctions as a function of the iteration number and have established a convergence criterion based on the global difference between the approximate eigenfunctions of consecutive time steps.

The main disadvantage of our test case is the presence of sharp boundaries in the equilibrium structure, which leads to abrupt jumps of the eigenfunction $i\hat{v}_y$ and non-derivable eigenfunctions $\hat{v}_x$ and $i\hat{b}_z$ at these positions (see Figure 2). We have found that these normal mode features result in the presence of large errors at the slab boundary, which are quite substantial for the approximation to $i\hat{v}_y$; see Figures 7 and 8.

We have obtained an approximation to the two normal modes of interest (the fundamental evanescent mode and its second longitudinal overtone) with great accuracy: after six iterations, the frequency is wrong by only 0.5%–0.7% and the eigenfunctions $\hat{v}_x$ and $i\hat{b}_z$ have maximum errors of the order of 0.6% and 0.7%, respectively. The case of $i\hat{v}_y$ is worse because of the difficulties of recovering a function that jumps at $x = \pm a$. If these two lines are ignored, the maximum error of $i\hat{v}_y$ is also of the order of 0.6%.

In the second paper of this work (S. Rial et al. 2019, in preparation) we will apply the technique presented here to the time-dependent numerical simulations of a loop embedded in a coronal arcade carried out by Rial et al. (2013). The equilibrium structure is similar to the one used in the present paper but includes a curved slab in which both the magnetic field strength and plasma density vary along the magnetic field. The initial condition used by Rial et al. (2013) is analogous to Equation (29), so various longitudinal harmonics are excited. The present paper shows that our technique is well suited for this task because it allows us to obtain the features of different normal modes. Its application to the more realistic numerical simulations by Rial et al. (2013) should produce normal mode characteristics comparable to observed loop oscillation events.

R.O. and J.T. acknowledge support from the Spanish Ministry of Economy and Competitiveness (MINECO) and FEDER funds through project AYA2017-85465-P. I.A. acknowledges support by the Spanish Ministry of Economy and Competitiveness (MINECO) through projects AYA2014-55456-P (Bayesian Analysis of the Solar Corona) and AYA2014-60476-P (Solar Magnetometry in the Era of Large Solar Telescopes) and FEDER funds. R.O. is indebted to D. W. Fanning for making available the Coyote Library of IDL programs (http://www.idlcoyote.com/).

ORCID iDs

I. Arregui https://orcid.org/0000-0002-7008-7661
R. Oliver https://orcid.org/0000-0003-4162-7240
J. Terradas https://orcid.org/0000-0002-7013-1933

References

Andries, J., Arregui, I., & Goossens, M. 2005a, ApJL, 624, L57
Andries, J., Goossens, M., Hollweg, J. V., Arregui, I., & van Doorsselaere, T. 2005b, A&A, 430, 1109
Arregui, I., Terradas, J., Oliver, R., & Ballester, J. L. 2007, SoPh, 246, 213
Aschwanden, M. J., Fletcher, L., Schrijver, C. J., & Alexander, D. 1999, ApJ, 520, 880
Aschwanden, M. J., & Terradas, J. 2008, ApJL, 686, L127
Bona, C., Bona-Casas, C., & Terradas, J. 2009, JCoPh, 228, 2266
Edwin, P. M., & Roberts, B. 1983, SoPh, 88, 179
Goedbloed, J., & Poedts, S. 2004, Principles of Magnetohydrodynamics: With Applications to Laboratory and Astrophysical Plasmas (Cambridge: Cambridge Univ. Press)
Goossens, M., Andries, J., & Aschwanden, M. J. 2002, A&A, 394, L39
Hannachi, A., Jolliffe, I. T., & Stephenson, D. B. 2007, IJCli, 27, 1119
Heyvaerts, J., & Priest, E. R. 1983, A&A, 117, 220
Hollweg, J. V., & Yang, G. 1988, JGR, 93, 5423
Horel, J. D. 1984, JApMe, 23, 1660
Lomb, N. R. 1976, Ap&SS, 39, 447
Morton, R. J., & Erdélyi, R. 2009, ApJ, 707, 750
Nakariakov, V. M., Ofman, L., Deluca, E. E., Roberts, B., & Davila, J. M. 1999, Sci, 285, 862
Nakariakov, V. M., & Verwichte, E. 2005, LRSP, 2, 3
Priest, E. 2014, Magnetohydrodynamics of the Sun (Cambridge: Cambridge Univ. Press)
Rial, S., Arregui, I., Terradas, J., Oliver, R., & Ballester, J. L. 2013, ApJ, 763, 16
Roberts, B. 1981, SoPh, 69, 39
Ruderman, M. S. 2003, A&A, 409, 287
Ruderman, M. S., & Erdélyi, R. 2009, SSRv, 149, 199
Ruderman, M. S., & Roberts, B. 2002, ApJ, 577, 475
Ruderman, M. S., Verth, G., & Erdélyi, R. 2008, ApJ, 686, 694
Scargle, J. D. 1982, ApJ, 263, 835
Selwa, M., Murawski, K., Solanki, S. K., & Wang, T. J. 2007, A&A, 462, 1127
Selwa, M., Ofman, L., & Solanki, S. K. 2011a, ApJ, 726, 42
Selwa, M., Solanki, S. K., Murawski, K., Wang, T. J., & Shumlak, U. 2006, A&A, 454, 653
Selwa, M., Solanki, S. K., & Ofman, L. 2011b, ApJ, 728, 87
Terradas, J., Arregui, I., Oliver, R., et al. 2008, ApJ, 679, 1611
Terradas, J., Oliver, R., & Ballester, J. L. 2004, ApJ, 614, 435
Terradas, J., Oliver, R., & Ballester, J. L. 2006, ApJL, 650, L91
van Doorsselaere, T., Debosscher, A., Andries, J., & Poedts, S. 2004, A&A, 424, 1065
van Doorsselaere, T., Verwichte, E., & Terradas, J. 2009, SSRv, 149, 299
von Storch, H., & Zwiers, F. W. 1999, Statistical Analysis in Climate Research (Cambridge: Cambridge Univ. Press), doi:10.1017/CBO9780511612336
Wallace, J. M., & Dickinson, R. E. 1972, JApMe, 11, 887

Chapter 5

Conclusions and future work

The conclusions of this thesis are done from several points of view. On one hand we present a summary of the results obtained in each of the papers that compose the thesis. On the other hand, we discuss the achieved goals and finally we point out some future work that can be done departing from where we left our investigation.

In Chapter 2 two types of numerical experiments are carried out. On one hand, resonant wave energy exchange between a fast normal mode-like of the system and local Alfvén waves is analyzed. The goal of this numerical experiment is to make an initial test to our temporal code. As the behavior of the normal modes have been studied by many authors using equivalent models we will use their results to guide us. The results from the temporal evolution of a normal mode-like fast disturbance are quite satisfactory, resonant absorption phenomenon due to three-dimensional propagation of perturbations in a non-uniform medium, takes place at the position and with the frequency predicted.

On the other hand, we consider a more realistic situation by using as the initial perturbation a localized impulsive excitation. This kind disturbance is a more faithful model of what happens in the solar corona when a sudden release of energy occurs. In this case there are several results that are worthy to mention. First as the initial perturbation is made by the sum of normal modes, resonant coupling between fast and Alfvén waves now happens in all the domain. One of the main results of this experiment is that even though a part of the fast mode-like energy is able the leave the system always a fraction of it can be retained in the system without having a density enhancement or a cavity structure. This energy is stored in form Alfvén oscillations which remain confined around magnetic surfaces. A phenomenon that is observed and is worth to be mentioned is phase mixing. As the Alfvén frequency of each magnetic line is slightly different, as time evolves they became out of phase and it gives rise spatial scales that decrease with time until one point where the numerical code is unable to properly follow its evolution.

In this case we can also test our numerical results following the guides of previous studies. It is a known result from Arregui et al. (2004a), that when perpendicular propagation is considered, the frequency of the Alfvén oscillations should not change from the pure poloidal case. So another result from this experiment is that the frequency of the induced Alfvénic oscillations is seen to be independent from the perpendicular wavenumber.

Finally, the wave energy exchange between the fast-like perturbation and the Alfvén oscillations has been analyzed as a function of the perpendicular wavenumber and the ratio of the magnetic scale height to the density scale height. In this case the fraction of the energy trapped by the magnetic structure increases with the value of the perpendicular wavenumber. To end with, the ratio of magnetic to density scale heights determines the pace at which the available fast wave energy leaves the system and also how fast this energy is converted to Alfvén waves, but not the final amount of energy stored by the arcade in the form of Alfvénic oscillations.

In Chapter 3, we have analyzed the time dependent solutions of impulsively generated waves when we consider a curved density enhancement embedded in the same static magnetic potential arcade presented in our previous chapter. We use this configuration because we want to investigate the importance of using a realistic three-dimensional model on the damping of vertical loop oscillations. Following that direction, we begin by just allowing the three-dimensional propagation to the previous two-dimensional model and analyzing its consequences on the wave damping due to resonant absorption and wave leakage.

The results of using a pure two-dimensional model are that the initial impulsive perturbation does not leave any energy in the form of vertical kink oscillations. It is only able to excite a combination of leaky modes that leave the system very quickly. Therefore, when considering pure poloidal models, damping by wave leakage is the dominant mechanism for the attenuation of vertical loop oscillations and confirms the results of previous studies Brady and Arber (2005) and Brady et al. (2006).

When we allow perturbations propagate in the ignorable direction, two main results are obtained. On one hand, the initial perturbation not only excites some leaky modes, in this case trapped modes are also excited and the density enhancement is capable to store part of the energy in form of vertical kink oscillations. The amount of energy trapped by the loop increases directly with the perpendicular wave number. On the other hand, resonant coupling between fast and Alfvén modes ocurrs at those locations where the trapped mode frequency coincide that of Alfvén waves. As these positions can be theoretically predicted from previous studies, this can be seen as a test to our numerical results. Is worthy to point out that as our loop has a sharp density transition, the energy exchange between the trapped modes and the Alfvénic oscillations does not happen at the loop boundary, but at points located above the coronal loop, in the external medium. It will be interesting to add to the present model an smooth transition between the loop and the external medium to make resonant absorption happen at the loop boundary. This addition for sure will give us a better description of the observed damped transverse loop oscillations and it is left for future work.

The time-dependent results obtained in this chapter point out that vertical loop oscillations that are attenuated by two mechanism that are wave leakage from the slab and resonant absorption in the environment. Determine the fraction of the initial pulse energy transferred by means of these damping mechanisms should also be studied in a future work, although this is beyond the scope of this thesis.

In Chaper 4, we have investigated an alternative method to obtain the eigenmodes of a system, i.e., their eigenfunctions and eigenfrequencies. The method consists in iteratively solve the time-dependent problem of the system and afterwards apply a CEOF analysis to the temporal results. After each iteration, the resulting CEOF modes are utilized as the initial conditions for the time-dependent numerical simulation of the next iteration. It is important to note that we use a model where its normal modes can be solved following the standard method, see Arregui et al. (2007b), and comparisons can help us to determine the goodness of our iterative method.

The results of our approach to normal modes has been quite satisfactory but some points have to be taken into account. The main disadvantage of the method is the presence of non smooth boundaries in the density enhancement. These abrupt jumps leads to non-derivable eigenfunctions and we have found that these features result in large errors at the points where they are located. Therefore the main result is that when using sharp equilibriums, the results obtained at these particular locations are not accurate.

A possible way to avoid the complications at the non-derivable locations, would be to substitute the CEOF analysis in the full spatial domain by three analysis in the three derivable domains $L_x \leq x < -a$, $-a \leq x \leq a$, and $a < x \leq L_x$. As all eigenfunctions and their derivatives are smooth in each individual domain, we may obtain an approximation to frequencies and eigenfunctions that is free from the large errors at the sharp boundaries. Splitting the spatial domain in several pieces when doing the CEOF analysis is somehow similar to removing the initial time to get rid of the wave transients, such as we have done here. We have not yet tried this improvement and leave it for a future work.

Keeping in mind the previous result, we have obtained accurate approximations to the fundamental mode and its second longitudinal overtone after 6 iterations. Therefore the main result of this investigation is that this method opens a new possibility when the standard method to find normal modes of a system can not be carried out. It is important to note that it can be applied, with the usage restrictions above mentioned, to find the normal modes of any system because we have not use any approximation that limits its application.

To end with, we summarize some the goals accomplished and finally we draw some possibilities left for future work.

- We have been able to prove that we can obtain reliable time-dependent results when several models of coronal loop oscillations are considered. This has been one of our main aims of this thesis, begin from simple configurations where solutions are well known and see if we can reproduce these results using the time-dependent approach.

- Over this basis we have acquired new knowledge on the field of coronal loop oscillations by increasing the complexity of the models step by step. In order to reproduce the observed oscillations, we have focused in adding the three-dimensional ingredient to our model, which we think can be a key element.

- We have investigated how the time-dependent and the normal mode approach are related. This has been realized by taking the results of many theoretical works done in normal modes and see how they are represented in the temporal approach.

- We also have approached to the problem of coronal loop oscillations using the normal mode method. We have devised an alternative method to fully determine the normal modes of a system that can be applied in general to any equilibrium model.

As for the future work, it is left several investigations that will complete this research such as

- To find the normal modes of the model presented in Chaper 3 using the method presented in Chapter 4. In this case we do not have any theoretical studies that can guide us. This work is in preparation as the second part of the paper Rial et al. (2019).
- To solve the time-dependent problem of the model presented in Chapter 3 when the coronal loop have a smooth density profile. This can be a step forward the realistic modeling of coronal loops oscillations.

Bibliography

Andries, J., Arregui, I. and Goossens, M.: 2005, Determination of the Coronal Density Stratification from the Observation of Harmonic Coronal Loop Oscillations, ApJL **624**, 57–60.

Anfinogentov, S. A., Nakariakov, V. M. and Nisticò, G.: 2015, Decayless low-amplitude kink oscillations: a common phenomenon in the solar corona?, A&A **583**, A136.

Antolin, P., De Moortel, I., Van Doorsselaere, T. and Yokoyama, T.: 2017, Observational signatures of transverse MHD waves and associated dynamic instabilities, ApJ **836**(2), 219.

Antolin, P., Okamoto, T. J., De Pontieu, B., Uitenbroek, H., Van Doorsselaere, T. and Yokoyama, T.: 2015, Resonant Absorption of Transverse Oscillations and Associated Heating in a Solar Prominence. II. Numerical Aspects, ApJ **809**(1), 72.

Antolin, P., Yokoyama, T. and Van Doorsselaere, T.: 2014, Fine Strand-like Structure in the Solar Corona from Magnetohydrodynamic Transverse Oscillations, ApJL **787**(2), L22.

Arregui, I.: 2015, Wave heating of the solar atmosphere, Philosophical Transactions of the Royal Society of London Series A **373**(2042), 20140261–20140261.

Arregui, I., Andries, J., van Doorsselaere, T., Goossens, M. and Poedts, S.: 2007a, MHD seismology of coronal loops using the period and damping of quasi-mode kink oscillations, A&A **463**, 333–338.

Arregui, I., Oliver, R. and Ballester, J. L.: 2004a, Magnetohydrodynamic waves in a sheared potential coronal arcade, A&A **425**, 729–739.

Arregui, I., Oliver, R. and Ballester, J. L.: 2004b, Magnetohydrodynamic Waves in Sheared Coronal Arcades, ApJ **602**, 1006–1020.

Arregui, I., Terradas, J., Oliver, R. and Ballester, J. L.: 2007b, Resonantly Damped Surface and Body MHD Waves in a Solar Coronal Slab with Oblique Propagation, Sol. Phys. **246**, 213–230.

Aschwanden, M. J.: 1987, Theory of radio pulsations in coronal loops, Sol. Phys. **111**, 113–136.

Aschwanden, M. J.: 2003, Review of Coronal Oscillations - An Observer's View, ArXiv Astrophysics e-prints.

Aschwanden, M. J.: 2005, Physics of the Solar Corona. An Introduction with Problems and Solutio Praxis Publishing Ltd., Chichester UK, and Springer, New York.

Aschwanden, M. J.: 2009, The 3D Geometry, Motion, and Hydrodynamic Aspects of Oscillating Coronal Loops, Space science reviews **149**, 31–64.

Aschwanden, M. J. and Schrijver, C. J.: 2011, Coronal Loop Oscillations Observed with Atmospheric Imaging Assembly - Kink Mode with Cross-sectional and Density Oscillations, ApJ **736**, 102.

Aschwanden, M. J., de Pontieu, B., Schrijver, C. J. and Title, A. M.: 2002, Transverse Oscillations in Coronal Loops Observed with TRACE II. Measurements of Geometric and Physical Parameters, Sol. Phys. **206**, 99–132.

Aschwanden, M. J., Fletcher, L., Schrijver, C. J. and Alexander, D.: 1999, Coronal Loop Oscillations Observed with the Transition Region and Coronal Explorer, ApJ **520**, 880–894.

Aschwanden, M. J., Nightingale, R. W., Andries, J., Goossens, M. and Van Doorsselaere, T.: 2003, Observational Tests of Damping by Resonant Absorption in Coronal Loop Oscillations, ApJ **598**, 1375–1386.

Aschwanden, M. J., Poland, A. I. and Rabin, D. M.: 2001, The New Solar Corona, ARAA **39**, 175–210.

Berghmans, D. and Clette, F.: 1999, Active region EUV transient brightenings - First Results by EIT of SOHO JOP80, Sol. Phys. **186**, 207–229.

Brady, C. S. and Arber, T. D.: 2005, Damping of vertical coronal loop kink oscillations through wave tunneling, A&A **438**, 733–740.

Brady, C. S., Verwichte, E. and Arber, T. D.: 2006, Leakage of waves from coronal loops by wave tunneling, A&A **449**, 389–399.

de Moortel, I.: 2009, Longitudinal Waves in Coronal Loops, Space science reviews **149**, 65–81.

De Moortel, I., Hood, A. W. and Ireland, J.: 2002a, Coronal seismology through wavelet analysis, A&A **381**, 311–323.

De Moortel, I., Hood, A. W., Ireland, J. and Walsh, R. W.: 2002b, An overview of longitudinal oscillations in coronal loops, in A. Wilson (ed.), Solar Variability: From Core to Outer Frontiers, Vol. 506 of ESA Special Publication, pp. 509–512.

De Moortel, I., Ireland, J. and Walsh, R. W.: 2000, Observation of oscillations in coronal loops, A&A **355**, 23–26.

De Moortel, I., Ireland, J., Walsh, R. W. and Hood, A. W.: 2002c, Longitudinal intensity oscillations in coronal loops observed with TRACE I. Overview of Measured Parameters, Sol. Phys. **209**, 61–88.

De Moortel, I., Pascoe, D. J., Wright, A. N. and Hood, A. W.: 2016, Transverse, propagating velocity perturbations in solar coronal loops, Plasma Physics and Controlled Fusion **58**(1), 014001.

Del Zanna, L., Schaekens, E. and Velli, M.: 2005, Transverse oscillations in solar coronal loops induced by propagating Alfvénic pulses, A&A **431**, 1095–1104.

Díaz, A. J., Zaqarashvili, T. and Roberts, B.: 2006, Fast magnetohydrodynamic oscillations in a force-free line-tied coronal arcade, A&A **455**, 709–717.

Ebrahimi, Z. and Karami, K.: 2016, Resonant absorption of kink magnetohydrodynamic waves by a magnetic twist in coronal loops, Monthly Notices of the Royal Astronomical Society **462**, 1002–1011.

Edwin, P. M. and Roberts, B.: 1982, Wave propagation in a magnetically structured atmosphere. III - The slab in a magnetic environment, Sol. Phys. **76**, 239–259.

Edwin, P. M. and Roberts, B.: 1983, Wave propagation in a magnetic cylinder, Sol. Phys. **88**, 179–191.

Goddard, C. R. and Nakariakov, V. M.: 2016, Dependence of kink oscillation damping on the amplitude, A&A **590**, L5.

Goedbloed, J. P. H. and Poedts, S.: 2004, Principles of Magnetohydrodynamics: With Applications to Laboratory and Astrophysical Plasm UK: Cambridge University Press.

Golub, L. & Pasachoff, J. M.: 1997, The Solar Corona, UK: Cambridge University Press.

Goossens, M.: 1991, Resonant Absorption of MHD Waves in Magnetic Loops in the Solar Corona, in P. Ulmschneider, E. R. Priest and R. Rosner (eds), Mechanisms of Chromospheric and Coronal Heating, p. 480.

Goossens, M., Andries, J. and Aschwanden, M. J.: 2002, Coronal loop oscillations. An interpretation in terms of resonant absorption of quasi-mode kink oscillations, A&A **394**, 39–42.

Goossens, M., Arregui, I., Ballester, J. L. and Wang, T. J.: 2008, Analytic approximate seismology of transversely oscillating coronal loops, A&A **484**, 851–857.

Goossens, M., Erdélyi, R. and Ruderman, M. S.: 2011, Resonant MHD Waves in the Solar Atmosphere, Space science reviews **158**(2-4), 289–338.

Goossens, M., Poedts, S. and Hermans, D.: 1985, On the existence of the continuous spectrum of ideal MHD in a 2D magnetostatic equilibrium, Sol. Phys. **102**, 51–66.

Goossens, M., Soler, R., Terradas, J., Van Doorsselaere, T. and Verth, G.: 2014, The Transverse and Rotational Motions of Magnetohydrodynamic Kink Waves in the Solar Atmosphere, ApJ **788**(1), 9.

Guo, M., Van Doorsselaere, T., Karampelas, K., Li, B., Antolin, P. and De Moortel, I.: 2019, Heating Effects from Driven Transverse and Alfvén Waves in Coronal Loops, ApJ **870**(2), 55.

Heyvaerts, J. and Priest, E. R.: 1983, Coronal heating by phase-mixed shear Alfven waves, A&A **117**, 220–234.

Hindman, B. W. and Jain, R.: 2014, An Interpretation of Flare-induced and Decayless Coronal-loop Oscillations as Interference Patterns, ApJ **784**, 103.

Hollweg, J. V. and Yang, G.: 1988, Resonance absorption of compressible magnetohydrodynamic waves at thin 'surfaces', Journal of Geophysical Research **93**, 5423–5436.

Howson, T. A., De Moortel, I. and Antolin, P.: 2017, Energetics of the Kelvin-Helmholtz instability induced by transverse waves in twisted coronal loops, A&A **607**, A77.

Luna, M., Terradas, J., Oliver, R. and Ballester, J. L.: 2009, Transverse Oscillations of Systems of Coronal loops, ApJ **692**(2), 1582–1589.

Magyar, N. and Van Doorsselaere, T.: 2016a, Damping of nonlinear standing kink oscillations: a numerical study, A&A **595**, A81.

Magyar, N. and Van Doorsselaere, T.: 2016b, The Instability and Non-existence of Multi-stranded Loops When Driven by Transverse Waves, ApJ **823**(2), 82.

Mariska, J. T. and Muglach, K.: 2010, Doppler-shift, Intensity, and Density Oscillations Observed with the Extreme Ultraviolet Imaging Spectrometer on Hinode, ApJ **713**, 573–583.

Mrozek, T.: 2011, Failed Eruption of a Filament as a Driver for Vertical Oscillations of Coronal Loops, Sol. Phys. **270**, 191–203.

Murawski, K., Selwa, M. and Nocera, L.: 2005, Numerical simulations of fast magnetosonic waves in a curved coronal loop, A&A **437**, 687–690.

Nakariakov, V. M. and Ofman, L.: 2001, Determination of the coronal magnetic field by coronal loop oscillations, A&A **372**, 53–56.

Nakariakov, V. M. and Verwichte, E.: 2005, Coronal waves and oscillations, Living Reviews in Solar Physics.

Nakariakov, V. M., Ofman, L., Deluca, E. E., Roberts, B. and Davila, J. M.: 1999, TRACE observation of damped coronal loop oscillations: Implications for coronal heating, Science **285**, 862–864.

Nakariakov, V. M., Verwichte, E., Berghmans, D. and Robbrecht, E.: 2000, Slow magnetoacoustic waves in coronal loops, A&A **362**, 1151–1157.

Nightingale, R. W., Aschwanden, M. J. and Hurlburt, N. E.: 1999, Time Variability of EUV Brightenings in Coronal Loops Observed with TRACE, Sol. Phys. **190**, 249–265.

Nisticò, G., Nakariakov, V. M. and Verwichte, E.: 2013, Decaying and decayless transverse oscillations of a coronal loop, A&A **552**, A57.

Ofman, L. and Wang, T.: 2002, Hot Coronal Loop Oscillations Observed by SUMER: Slow Magnetosonic Wave Damping by Thermal Conduction, ApJL **580**, 85–88.

Oliver, R., Ballester, J. L., Hood, A. W. and Priest, E. R.: 1993, Magnetohydrodynamic waves in a potential coronal arcade, A&A **273**, 647–658.

Oliver, R., Hood, A. W. and Priest, E. R.: 1996, Magnetohydrodynamic Waves in Solar Coronal Arcades, ApJ **461**, 424–444.

Oliver, R., Murawski, K. and Ballester, J. L.: 1998, Numerical simulations of impulsively generated MHD waves in a potential coronal arcade, A&A **330**, 726–738.

Pagano, P. and De Moortel, I.: 2019, Contribution of observed multi frequency spectrum of Alfvén waves to coronal heating, A&A **623**, A37.

Pagano, P., Pascoe, D. J. and De Moortel, I.: 2018, Contribution of phase-mixing of Alfvén waves to coronal heating in multi-harmonic loop oscillations, A&A **616**, A125.

Pascoe, D. J., Goddard, C. R., Nisticò, G., Anfinogentov, S. and Nakariakov, V. M.: 2016, Damping profile of standing kink oscillations observed by SDO/AIA, A&A **585**, L6.

Poedts, S. and Goossens, M.: 1988, The continuous spectrum of MHD waves in 2-D solar loops and arcades - Parametric study of poloidal mode coupling for poloidal magnetic fields, A&A **198**, 331–340.

Poedts, S., Hermans, D. and Goossens, M.: 1985, The continuous spectrum of an axisymmetric self-gravitating and static equilibrium with a mixed poloidal and toroidal magnetic field, A&A **151**, 16–26.

Priest, E. R.: 1984, Solar magneto-hydrodynamics, Geophysics and Astrophysics Monographs, Reidel.

Rial, S., Arregui, I., Oliver, R. and Terradas, J.: 2019, Normal modes of transverse coronal loop oscillations from numerical simulations. i. method and test case, ApJ **876**(1), 86.

Rial, S., Arregui, I., Terradas, J., Oliver, R. and Ballester, J. L.: 2010, Three-dimensional Propagation of Magnetohydrodynamic Waves in Solar Coronal Arcades, ApJ **713**, 651–661.

Rial, S., Arregui, I., Terradas, J., Oliver, R. and Ballester, J. L.: 2013, Wave Leakage and Resonant Absorption in a Loop Embedded in a Coronal Arcade, ApJ **763**, 16.

Roberts, B.: 2000, Waves and Oscillations in the Corona - (Invited Review), Sol. Phys. **193**, 139–152.

Roberts, B., Edwin, P. M. and Benz, A. O.: 1984, On coronal oscillations, ApJ **279**, 857–865.

Ruderman, M. S.: 2015, Propagating kink waves in thin twisted magnetic tubes with continuous equilibrium magnetic field, A&A **575**, A130.

Ruderman, M. S. and Roberts, B.: 2002, The Damping of Coronal Loop Oscillations, ApJ **577**, 475–486.

Safari, H., Nasiri, S. and Sobouti, Y.: 2007, Fast kink modes of longitudinally stratified coronal loops, A&A **470**, 1111–1116.

Selwa, M., Murawski, K., Solanki, S. K. and Wang, T. J.: 2007, Energy leakage as an attenuation mechanism for vertical kink oscillations in solar coronal wave guides, A&A **462**, 1127–1135.

Selwa, M., Solanki, S. K., Murawski, K., Wang, T. J. and Shumlak, U.: 2006, Numerical simulations of impulsively generated vertical oscillations in a solar coronal arcade loop, A&A **454**, 653–661.

Smith, J. M., Roberts, B. and Oliver, R.: 1997, Ducted fast waves in coronal loops: curvature effects., A&A **317**, 752–760.

Soler, R. and Terradas, J.: 2015, Magnetohydrodynamic Kink Waves in Nonuniform Solar Flux Tubes: Phase Mixing and Energy Cascade to Small Scales, ApJ **803**(1), 43.

Spruit, H. C.: 1981, Motion of magnetic flux tubes in the solar convection zone and chromosphere, A&A **98**, 155–160.

Tandberg-Hanssen, E.: 1995, Books-Received - the Nature of Solar Prominences, Science **269**, 111.

Terradas, J.: 2009, Excitation of Standing Kink Oscillations in Coronal Loops, Space science reviews **149**, 255–282.

Terradas, J. and Arregui, I.: 2018, Temporal and spatial scales for coronal heating by alfvén wave dissipation in transverse loop oscillations, Research Notes of the AAS **2**(4), 196.

Terradas, J. and Goossens, M.: 2012, Transverse kink oscillations in the presence of twist, A&A **548**, A112.

Terradas, J., Arregui, I., Oliver, R., Ballester, J. L., Andries, J. and Goossens, M.: 2008a, Resonant Absorption in Complicated Plasma Configurations: Applications to Multistranded Coronal Loop Oscillations, ApJ **679**, 1611–1620.

Terradas, J., Oliver, R. and Ballester, J. L.: 1999, Magnetohydrodynamic Waves in Coronal Magnetostatic Arcades, ApJ **517**, 488–496.

Terradas, J., Oliver, R. and Ballester, J. L.: 2004, Application of Statistical Techniques to the Analysis of Solar Coronal Oscillations, ApJ **614**, 435–447.

Terradas, J., Oliver, R. and Ballester, J. L.: 2005, On the excitation of trapped and leaky modes in coronal slabs, A&A **441**, 371–378.

Terradas, J., Oliver, R. and Ballester, J. L.: 2006a, Damped Coronal Loop Oscillations: Time-dependent Results, ApJ **642**, 533–540.

Terradas, J., Oliver, R. and Ballester, J. L.: 2006b, Damping of Kink Oscillations in Curved Coronal Loops, ApJL **650**, 91–94.

Terradas, J., Oliver, R., Ballester, J. L. and Keppens, R.: 2008b, On the Properties of Low-β Magnetohydrodynamic Waves in Curved Coronal Fields, ApJ **675**, 875–884.

Tsubaki, T.: 1988, Observations of periodic oscillations or waves in the solar corona and prominences, in R. C. Altrock (ed.), Solar and Stellar Coronal Structure and Dynamics, p. 140.

Uchida, Y.: 1970, Diagnosis of Coronal Magnetic Structure by Flare-Associated Hydromagnetic Disturbances, Publ. Astron. Soc. of Japan **22**, 341–364.

Čadež , V. M. and Ballester, J. L.: 1995a, MHD disturbances in a coronal potential arcade generated by localized perturbers., A&A **296**, 537–549.

Čadež , V. M. and Ballester, J. L.: 1995b, Time evolution of MHD disturbances impulsively excited by a localized perturber in a potential coronal arcade., A&A **296**, 550–559.

Van Doorsselaere, T., Antolin, P. and Karampelas, K.: 2018, Broadening of the differential emission measure by multi-shelled and turbulent loops, A&A **620**, A65.

Van Doorsselaere, T., Debosscher, A., Andries, J. and Poedts, S.: 2004, The effect of curvature on quasi-modes in coronal loops, A&A **424**, 1065–1074.

Van Doorsselaere, T., Verwichte, E. and Terradas, J.: 2009, The Effect of Loop Curvature on Coronal Loop Kink Oscillations, Space science reviews **149**, 299–324.

Verwichte, E., Aschwanden, M. J., Van Doorsselaere, T., Foullon, C. and Nakariakov, V. M.: 2009, Seismology of a Large Solar Coronal Loop from EUVI/STEREO Observations of its Transverse Oscillation, ApJ **698**, 397–404.

Verwichte, E., Foullon, C. and Nakariakov, V. M.: 2006a, Fast magnetoacoustic waves in curved coronal loops, A&A **446**, 1139–1149.

Verwichte, E., Foullon, C. and Nakariakov, V. M.: 2006b, Fast magnetoacoustic waves in curved coronal loops. II. Tunneling modes, A&A **449**, 769–779.

Verwichte, E., Foullon, C. and Nakariakov, V. M.: 2006c, Seismology of curved coronal loops with vertically polarised transverse oscillations, A&A **452**, 615–622.

Verwichte, E., Foullon, C. and Nakariakov, V. M.: 2006d, Seismology of curved coronal loops with vertically polarised transverse oscillations, A&A **452**, 615–622.

Verwichte, E., Foullon, C. and Van Doorsselaere, T.: 2010, Spatial Seismology of a Large Coronal Loop Arcade from TRACE and EIT Observations of its Transverse Oscillations, ApJ **717**, 458–467.

Verwichte, E., Nakariakov, V. M., Ofman, L. and Deluca, E. E.: 2004, Characteristics of transverse oscillations in a coronal loop arcade, Sol. Phys. **223**, 77–94.

Verwichte, E., Van Doorsselaere, T., Foullon, C. and White, R. S.: 2013, Coronal Alfvén Speed Determination: Consistency between Seismology Using AIA/SDO Transverse Loop Oscillations and Magnetic Extrapolation, ApJ **767**, 16.

Wang, T.: 2011, Standing Slow-Mode Waves in Hot Coronal Loops: Observations, Modeling, and Coronal Seismology, Space science reviews **158**, 397–419.

Wang, T., Innes, D. E. and Qiu, J.: 2007, Determination of the Coronal Magnetic Field from Hot-Loop Oscillations Observed by SUMER and SXT, ApJ **656**, 598–609.

Wang, T. J. and Solanki, S. K.: 2004, Vertical oscillations of a coronal loop observed by TRACE, A&A **421**, 33–36.

Wang, T. J., Ofman, L. and Davila, J. M.: 2009, Propagating Slow Magnetoacoustic Waves in Coronal Loops Observed by Hinode/EIS, ApJ **696**, 1448–1460.

Wang, T. J., Solanki, S. K., Curdt, W., Innes, D. E., Dammasch, I. E. and Kliem, B.: 2003a, Hot coronal loop oscillations observed with SUMER: Examples and statistics, A&A **406**, 1105–1121.

Wang, T. J., Solanki, S. K., Innes, D. E., Curdt, W. and Marsch, E.: 2003b, Slow-mode standing waves observed by SUMER in hot coronal loops, A&A **402**, 17–20.

Wang, T., Ofman, L., Davila, J. M. and Su, Y.: 2012, Growing Transverse Oscillations of a Multistranded Loop Observed by SDO/AIA, ApJL **751**, L27.

Watari, S., Detman, T. and Joselyn, J. A.: 1996, A Large Arcade Along the Inversion Line, Observed on May 19, 1992 by Yohkoh, and Enhancement of Interplanetary Energetic Particles, Sol. Phys. **169**, 167–179.

Weiss, L. A., Gosling, J. T., McAllister, A. H., Hundhausen, A. J., Burkepile, J. T., Phillips, J. L., Strong, K. T. and Forsyth, R. J.: 1996, A comparison of interplanetary coronal mass ejections at ULYSSES with YOHKOH soft X-ray coronal events., A&A **316**, 384–395.

Wentzel, D. G.: 1979, Hydromagnetic surface waves on cylindrical fluxtubes, A&A **76**, 20–23.

White, R. S. and Verwichte, E.: 2012, Transverse coronal loop oscillations seen in unprecedented detail by AIA/SDO, A&A **537**, A49.

Zaqarashvili, T. V.: 2003, Observation of coronal loop torsional oscillation, A&A **399**, 15–18.

Zimovets, I. V. and Nakariakov, V. M.: 2015, Excitation of kink oscillations of coronal loops: statistical study, A&A **577**, A4.